UNIVERSITY OF CALIFORNIA
Los Angeles

Integrated Terahertz Transceivers in Silicon for Point-to-Point Wireless Communication

A dissertation submitted in partial satisfaction
of the requirements for the degree
Doctor of Philosophy in Electrical and Computer Engineering

by

Mostafa Hosseini

2022

ABSTRACT OF THE DISSERTATION

Integrated Terahertz Transceivers in Silicon for Point-to-Point Wireless Communication

by

Mostafa Hosseini
Doctor of Philosophy in Electrical and Computer Engineering
University of California, Los Angeles, 2022
Professor Aydin Babakhani, Chair

Advances in silicon technologies and emerging on-chip antennas have provided a reliable solution for designing low-cost, high-speed integrated circuits. The birth of 5G systems and the definition of the 6G standard are evidence of the increasing interest in the exploration of terahertz frequencies for ultra-broadband wireless communication systems. Terahertz frequencies promise unlicensed wide-spectrum bandwidth for the next generation of wireless communication links.

Traditionally, terahertz systems have been realized optically by exploiting a photoconductive antenna with a femtosecond laser source. However, laser-based terahertz systems suffer from high cost, bulky measurement setups, and high power consumption, making them impractical for certain applications in communication, sensing, and imaging. In contrast, the transistor speed in silicon-based technologies has been improving over the last several decades, making electronic terahertz systems a low-cost and efficient alternative for optical systems. However, one of the main challenges in realizing efficient integrated terahertz systems in silicon is the generation and detection of signals beyond the maximum oscillation frequency ($\mathrm{f}_{\mathrm{max}}$) of a transistor, which does not exceed hundreds of gigahertz.

Considering all the progress made in electronic terahertz systems, researchers have remained pessimistic regarding the feasibility of terahertz propagation over relatively long distances due to high atmospheric absorption loss. This issue is even more critical for silicon-based terahertz radiators, where the amount of radiated power is 10s of dB below that of optical terahertz systems. Therefore, most studies in the terahertz domain have been limited to short-distance setups in a lab environment.

In this dissertation, a fully integrated laser-free terahertz impulse transceiver in silicon is presented that can radiate and detect arbitrary signals in millimeter-wave and terahertz bands with a 2 Hz frequency resolution. In the transmit mode, this chip radiates broadband impulses with 2.5-picosecond full width at half maximum, corresponding to a frequency comb with 1.052 terahertz bandwidth. In the receive mode, this design acts as a coherent detector that detects arbitrary signals up to 500 GHz with a peak sensitivity of -100 dBm with a 1 KHz resolution bandwidth. This receiver is utilized in conjunction with an impulse radiator to implement a dual-frequency comb spectroscopy system. A chip-to-chip dual-frequency comb is successfully measured and characterized in the 20–220 GHz frequency range. Additionally, this design can transmit picosecond impulses at 4 Gb/s data rate. Moreover, long-path terahertz communication channel characterization is introduced in the frequency range of 0.32–1.1 THz, where a specular link is created using a terahertz radiator, parabolic reflector antennas, a plane mirror, and a downconverter mixer. The terahertz channel is characterized up to a distance of 110 m. The measurement results demonstrate channel path loss, atmospheric absorption, and low-loss frequency windows suitable for long-range point-to-point wireless communication links in the terahertz regime.

The dissertation of Mostafa Hosseini is approved.

Danijela Cabric

Subramanian Srikantes Iyer

Yuanxun Wang

Aydin Babakhani, Committee Chair

University of California, Los Angeles

2022

To my family ...

TABLE OF CONTENTS

LIST OF FIGURES

LIST OF TABLES

ACKNOWLEDGMENTS

Now that my Ph.D. endeavor is coming to an end, I would like to express my sincere gratitude to those who supported me during this chapter of my life and made it unforgettable. The most important lesson I learned during this amazing journey was to never lose the sense of wonder and always accept the challenges to enter the unexplored territories.

First, I would like to thank my thesis supervisor, Professor Aydin Babakhani, who is the best advisor that I could possibly ask for. I am grateful to his continuous support, patience, motivation, and immense knowledge.

I would also like to thank Professors Danijela Cabric, Subramanian Iyer, and Ethan Wang for serving on my doctoral committee and providing valuable feedback to further improve the quality of my dissertation and research.

I thank Professors Asad Abidi, Behzad Razavi, Shervin Moloudi, Hooman Darabi, Bahram Jalali, and Sudhakar Pamarti for their wonderful graduate courses that gave me a unique profound experience and knowledge to broaden my insight into different aspects of electrical engineering, especially RF and analog design.

I am grateful to all members of UCLA Integrated Sensors Laboratory and Rice Integrated Circuits Systems group: Dr. Mahdi Assefzadeh, Dr. Peiyu Chen, Dr. Babak Jamali, Dr. Sam Razavian, Dr. Hamed Rahmani, Dr. Himashu Aggrawal, Dr. Charles Chen, Dr. Yuxiang Sun, Dr. Xuebei Yang, Dr. Mazdak Taghioskoui, Dr. Jaeeun Jang, Dr. Hongming Lyu, Mahdi Forghani, Yash Mehta, Hanni Alhowri, Yaswanth Kumar Cherivirala, Seyed Mohammad Kazempour, Dai Li, Iman habibagahi, Sidharth Thomas, Benyamin Fallah Motlagh, Jaskirat Singh Virdi, and Hamid Sharemi.

In particular, I want to thank Dr. Mahdi Assefzadeh, Dr. Peiyu Chen, and Dr. Babak Jamali for their mentoring during the early part of my PhD. I especially thank Dr. Sam Razavian for our invaluable technical discussions during this journey. I was fortunate enough to have many friends around me whom I could talk with and enjoy their company during

this long path. I would like to thank Sam Razavian, Saeed Khorram, Mohammad Talebi, Mahdi Assefzadeh, Mohammadreza Amirmoshiri, Ali Jebeli, and Ario Mirfatahi for their invaluable advice and discussions.

Finally, I would like to express my utmost gratitude to my parents for their unconditional love and support. Words cannot express how grateful I am to them for their infinite patience, support, and sacrifice. I owe all my success in life to my mother, for her unlimited love, and my father, who supports me in all aspects of life. I would also like to thank my sister, Rojan, for her love and patience. This long journey would not have been possible without their help and support. Although I have not seen them for years, it is difficult to put my gratitude for them in words and impossible to return their favor and kindness.

VITA

2015	B.Sc. in Electrical Engineering Sharif University of Technology, Tehran, Iran.
2015	Rice Electrical and Computer Engineering Fellowship Rice University, Houston, TX.
2015-2017	Graduate Research Assistant Rice University, Houston, TX.
2019	M.Sc. in Electrical and Computer Engineering University of California, Los Angeles.
2019	Advanced to PhD Candidacy University of California, Los Angeles.
2020	RFIC Design Engineering Intern Qualcomm Technologies, Inc., San Diego, California.
2021	RFIC Design Engineering Intern Qualcomm Technologies, Inc., San Diego, California.
2018–2022	Graduate Research Assistant University of California, Los Angeles.

PUBLICATIONS

1- **M. Hosseini** and A. Babakhani, "A 4-Gb/s Laser-Free Picosecond Impulse Transmitter With a Broadband On-Chip Antenna" *2020 45th International Conference on Infrared, Millimeter, and Terahertz Waves (IRMMW-THz), 2020, pp. 1-2.*

2- **M. Hosseini** and A. Babakhani, "A Fully Integrated 20-500-GHz Coherent Detector with 2-Hz Frequency Resolution," in *2020 IEEE BiCMOS and Compound Semiconductor Integrated Circuits and Technology Symposium (BCICTS), 2020, pp. 1-4.*

3- **M. Hosseini***, S. Razavian*, Y. Mehta* and A. Babakhani, ""Terahertz Channel Characterization Using a Broadband Frequency Comb Radiator in 130-Nm SiGe BiCMOS," in *IEEE Transactions on Terahertz Science and Technology, vol. 11, no. 3, pp. 269-276, May 2021.* *Equally contributed authors.

4- **M. Hosseini**, M. Assefzadeh, S. Razavian, Y. Mehta, and A. Babakhani, "Terahertz Channel Characterization using a Silicon-based Picosecond Pulse Source," in *2020 IEEE Radio and Wireless Symposium (RWS), 2020, pp. 76-79.*

5- **M. Hosseini**, and A. Babakhani, "Oscillator-Free Laser-Free THz Impulse Transceiver for Spectroscopy, Imaging, and Communication". (Under Preparation)

CHAPTER 1

Introduction

1.1 Overview of Terahertz Spectrum

Terahertz (THz) frequencies in the electromagnetic spectrum lie between radio frequencies at the lower end and optical frequencies at the higher end. This regime typically refers to the frequency range from 300 GHz to 3 THz, as shown in Fig. 1.1. In this spectrum, different frequencies correspond to different wavelengths and photon energies, having various properties of propagation and penetration through materials [1].

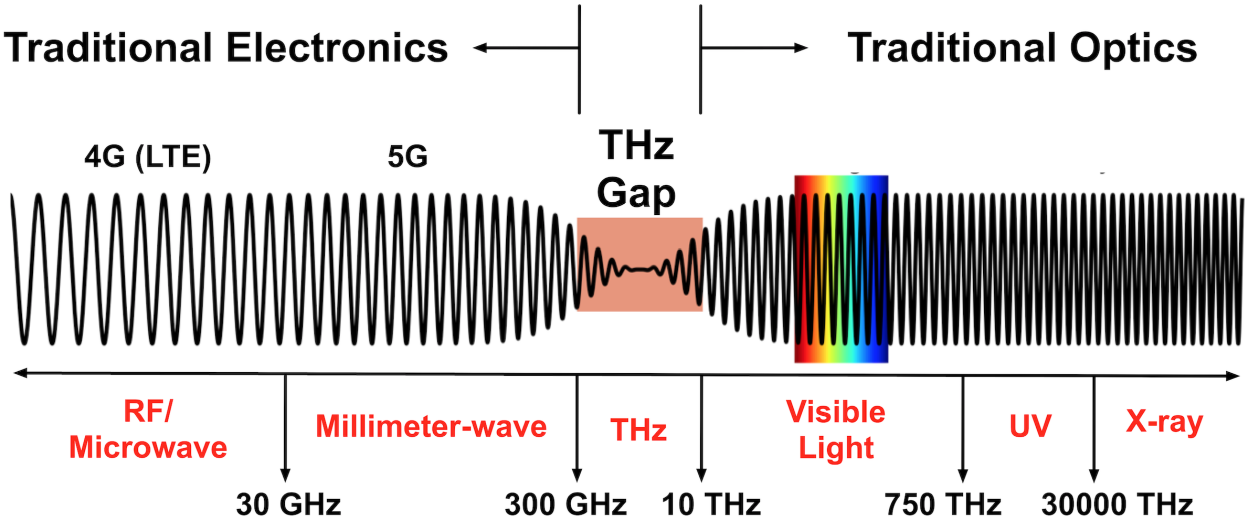

Figure 1.1: Overview of the electromagnetic wave spectrum and THz frequency regime.

This region is commonly called the THz gap due to lack of efficient methods for generating or detecting signals in this frequency regime since it is too high for electronic systems and too low for optical systems [2].

The wavelength in the THz frequency band is in the range of 0.03-3 mm. Due to the short wavelength of the electromagnetic waves in this frequency range and being comparable to circuit dimensions, a reconsideration of traditional electronic approaches is necessary. Therefore, new devices and techniques in conventional electronics, such as digital, analog, and radio frequency/microwave integrated circuits, are being developed.

In contrast, laser-based systems have limited applicability for THz generation due to lack of appropriate materials with sufficiently small bandgaps at room temperature [3]. Therefore, conventional electronic and optical techniques cannot be utilized in THz design and the THz gap exists in electronics and photonics research.

In this chapter, the advantages of silicon technology for broadband THz systems, as well as the challenges of conventional techniques for THz generation and detection are described. This chapter consists of four sections. First, an overview of the main applications of THz band is summarized. Second, the current techniques for THz generation in optics and electronics are discussed. Finally, the organization of the remaining context of this dissertation is listed.

1.2 Terahertz Wave Applications

This section discusses the main applications of THz frequencies are discussed. These applications include high-speed wireless communication, high-resolution imaging, molecular sensing and broadband spectroscopy, and remote sensing [4, 5, 6].

1.2.1 High-speed Wireless Communication

Due to the increasing demand for unregulated and unoccupied frequencies as well as higher data rate, THz communication systems are viable solutions for the next generation of wireless communication systems, such as 6G standards, point-to-point long-distance wireless links, and short-range server-client wireless communication. Such systems provide us high data rate due to the wide spectrum bandwidth (BW) that is achievable at higher frequency ranges [7, 8].

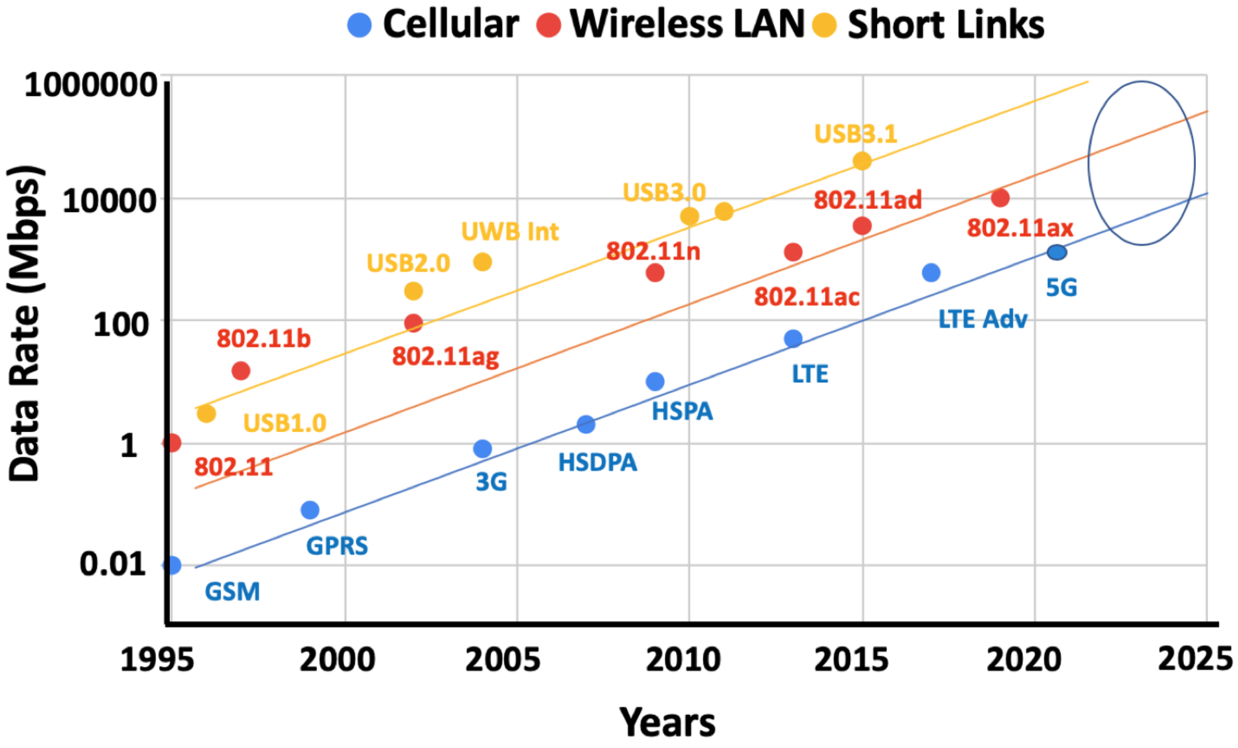

Figure 1.2: Wireless data rates over three decades.

The importance of the THz band for the future of communication applications can be better understood from Fig. 1.2. The exponential increasing trend in the data rate is clearly noticeable in cellular, wireless local area network (WLAN), and short-range communication systems. With the current trend, the data rate of cellular systems will surpass 100 Gb/s and that of WLAN links will surpass 1 Tb/s by the end of this decade [9]. According to Shannon-Hartley's ideal communication theorem, the channel capacity C (bits/sec) can be expressed as

$$C = B.log_2(1 + SNR) \tag{1.1}$$

where B is the BW of the communication channel and SNR is the signal-to-noise ratio. Hundreds of gigahertz of free unlicensed spectrum BW available in the THz regime makes it an ideal candidate to realize high-speed wireless communication links. It is evident that the THz band can realize Tb/s communication in the future. However, researchers have remained pessimistic regarding the feasibility of THz propagation over relatively long distances due to high atmospheric absorption loss. This issue is even more critical for silicon-based THz radiators, where the amount of radiated power is 10s of dB below that of optical THz systems.

Therefore, most studies in the THz domain have been limited to short-distance setups in a lab environment. Studies of long-distance THz propagation have mostly utilized laser-based THz sources. However, laser-based THz systems suffer from high power consumption, high cost, and bulky measurement setups. Therefore, although such studies have offered valuable analyses of the THz band, they do not promise a practical solution for the long-distance THz propagation problem.

To exploit THz frequencies for communication applications, it is imperative to study the atmospheric channel response of these frequencies and investigate the possibility of THz propagation over relatively long paths. Fig. 1.3 shows the atmospheric absorption loss [10]. As shown, atmospheric absorption is stronger in the THz range compared to millimeter-wave band; therefore, a precise knowledge of the locations and widths of these absorption lines is essential for the next generations of long-distance wireless links.

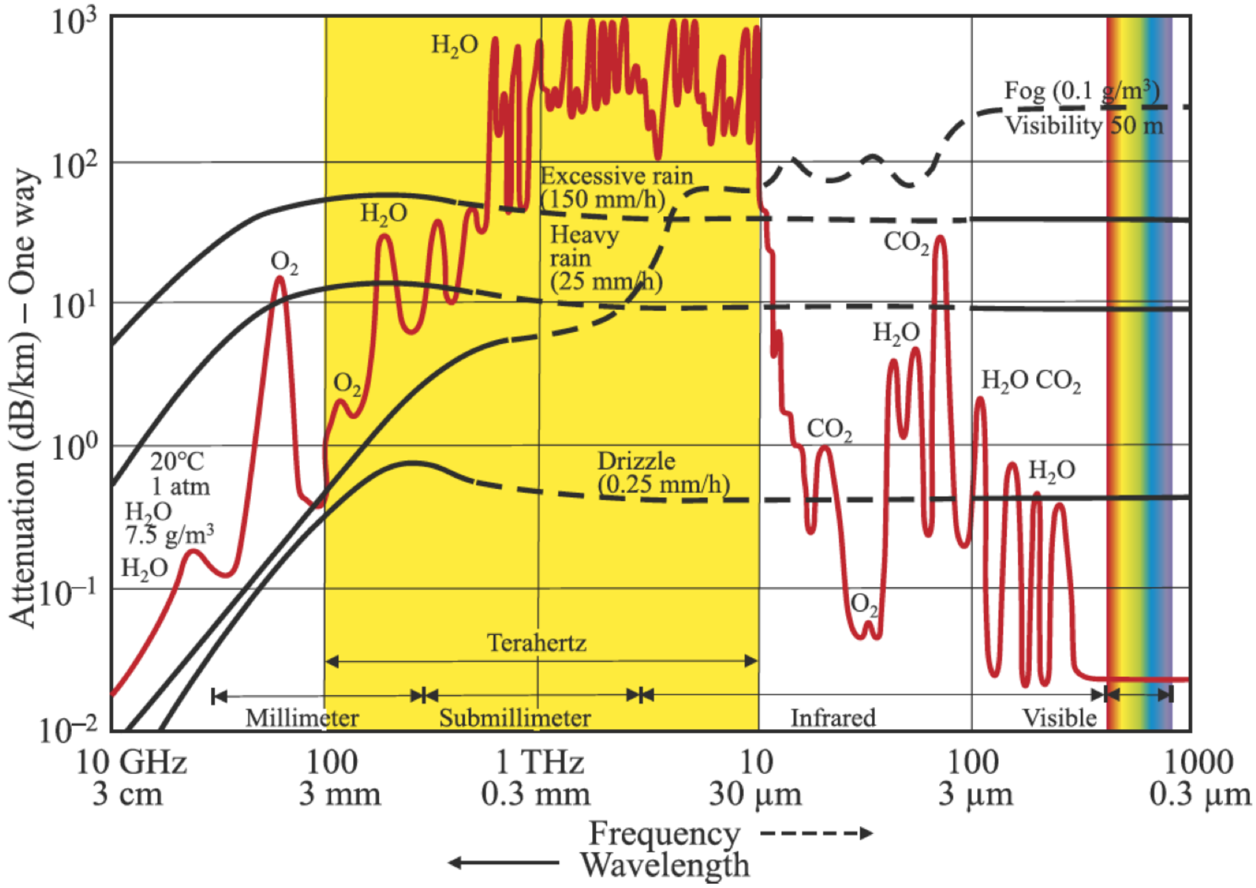

Figure 1.3: The atmospheric absorption loss in millimeter-wave, THz, infrared, and visible regions.

1.2.2 High-Resolution Imaging

THz light is an invisible radiation and travels in a line-of-sight (LOS), and like microwaves, efficiently transmits through most non-metallic mediums, such as clothing, bone, wood, plastic, paper, and ceramics. This enables the implementation of non-contact imaging systems that can see through conventional barriers and retrieve information from inside of non-metallic objects. Fig. 1.4 shows THz medical imaging [11], THz security imaging [12], and THz imaging for environmental monitoring [13].

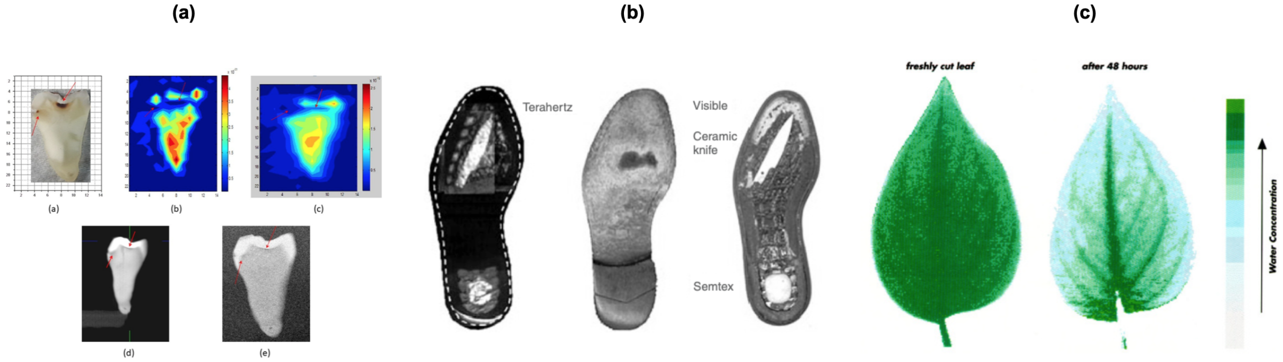

Figure 1.4: (a) THz medical imaging, (b) THz security imaging, (c) THz imaging for environmental monitoring.

Owing to the short wavelength of THz electromagnetic waves, transmission and reflection imaging systems in THz frequency ranges have superior spatial resolution. In transmission imaging systems [14], THz waves penetrate the objects and a THz detector receives them on the other side of the object. However, in reflection imaging systems [15], the THz source and reflected waves are on the same side.

THz imaging has been applied to numerous biological and medical applications [16]. THz waves can penetrate the body tissue like X-rays. However, X-ray technology emits ionizing radiation that breaks chemical bonds and is detrimental for living organisms. Therefore, THz imaging technologies have been introduced as a safe replacement for medical X-ray imaging systems. For biomedical applications, THz imaging can be utilized to extract information about the body tissues and blood samples that only lay in the THz spectrum [17, 18]. Furthermore, skin cancer detection [19], imaging of human breast tumors [20], and dental care [21] are other example of THz medical applications.

The non-ionizing nature of THz frequencies renders them effective in security applications, such as harmless and nondestructive imaging of explosive materials, weapons, and drugs [22]. THz imaging systems can perfectly handle the security screening tasks for concealed weapons, allowing us to see through the objects and identify hidden threats without disturbing its integrity, since many non-metallic and non-polar materials are transparent to THz radiation. Moreover, these systems are being utilized in many other applications, such as non-destructive industrial inspection [23], pharmaceutical industry [24], and environmental monitoring [13].

1.2.3 Molecular Sensing and Broadband Spectroscopy

Spectral sensing aims to distinguish various materials based on their responses to electromagnetic waves at different frequencies [25, 26]. A wide range of materials have unique absorption lines within the THz region due to transitions in their rotational [27] or vibrational [28] quantum states. This can be used as spectroscopic fingerprints for material identification [29]. The characteristic absorption frequencies of molecules and crystals in the microwave, THz, and infrared domains is shown in Fig. 1.5 ([30]).

Therefore, THz spectral sensing has been widely used in industries for applications such as toxic gas detection [31], chemical recognition [32], air-quality monitoring systems [33], and quality control in food and pharmaceutical industries [34].

Additionally, THz waves can be utilized to detect changes in the DNA-encoded chain in patients blood for the early diagnoses of diseases, genetically optimized medication, and gene therapy [35]. The rapid sensing and detection of virus (including SARS-CoV-2) and bacteria to identify and control epidemics is another potential application of THz frequencies [36].

Broadband spectroscopy systems are preferable as they can characterize objects over a wide range of frequencies and identify a large group of materials. Spectroscopy methods have been utilized in the THz region using femtosecond-laser-based THz time-domain spectroscopy systems [37]. However, such systems are bulky and expensive, making them impractical for some applications. In contrast, silicon-based chip-scale THz spectrometers provide a single solution to miniaturize these laser-based spectroscopy systems on a small millimeter-sized chip and minimize the fabrication cost [38, 39].

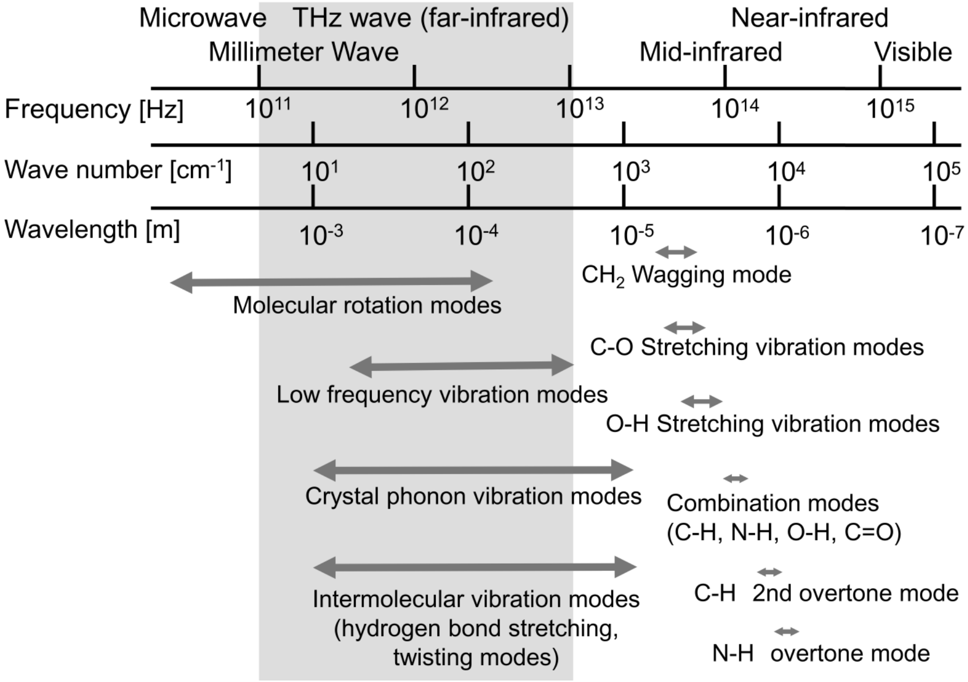

Figure 1.5: Characteristic absorption frequencies of molecules and crystals in the microwave, THz, and infrared domains.

1.2.4 Remote Sensing

In terms of remote sensing, THz systems can be used for non-contact-based vibrometry for wireless detection of sound [40, 41] or the speed of moving objects such as drones and airplanes [42]. Doppler effect has been used to detect, classify, and characterize moving objects, such as cars and aircraft, in radar applications. Due to the Doppler phenomenon, mechanical sound waves can cause vibrations on the surface of an object, which can modulate the frequency of the incident electromagnetic waves. As a result, small movements and weak vibrations of an object can be measured and characterized. By pushing the operating frequency of the vibrometry systems to the THz regime, the sensing resolution and accuracy can be increased due to the shorter wavelength. In addition, high operating frequencies and wide bandwidth enhance the spatial and lateral resolutions for radar applications.

Another application of THz systems is plasma characterization [43]. The general concept is to measure the phase shift of an electromagnetic wave in the plasma relative to that in vacuum. For high-density plasma, optical instruments utilizing lasers are adopted; however, this is challenging at these densities due to the small phase shift at low density. Therefore, to measure a broad range of plasma density, the system frequency must be sufficiently higher than the plasma frequency so that the beam stays coherent after traveling through a nonuniform plasma volume, but also low enough such that a phase difference is measurable at low density. As a result, the THz band is a viable solution to measure a broad range of plasma densities.

1.3 Terahertz Generation and Detection Techniques

This section discusses the current approaches for THz generation and detection in optics. THz systems have been often realized optically by exploiting femtosecond laser sources. In this approach, a photoconductive switch is used as an emitter and detector of THz waves [44]. In this approach, an incident femtosecond laser generates pairs of carriers (e.g. electrons and holes) in a photo-absorbing semiconductor. The photo-carriers are only generated when the incident photon energy is larger than the bandgap energy of the photoconductive substrate [46] (Fig. 1.6). By applying a bias voltage across the photoconductor contact electrodes, an electrical field is induced that accelerates the photo-carriers and generates an ultrafast photo-current. The collected photo-current at the corresponding contact electrodes is coupled to a THz antenna and the antenna radiates the THz electromagnetic waves. Typically, femtosecond laser pulse generates a sub-picosecond coherent electromagnetic pulse. For efficient THz generation, the transient time of the photo-carriers to the photoconductor contact electrodes should be a fraction of the oscillation period of the desired radiation [47]. Therefore, short-carrier lifetime photoconductive substrate such as low-temperature (LT) grown GaAs has been often utilized as the substrate of photoconductive switches for

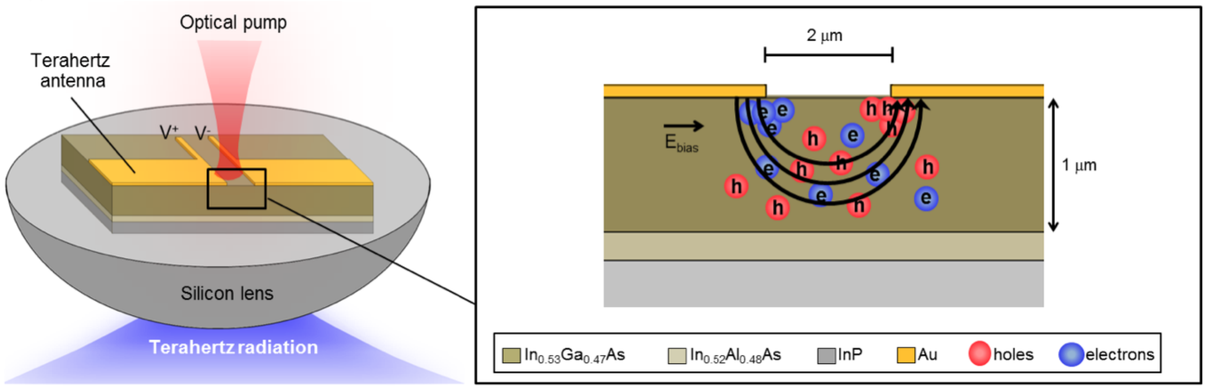

Figure 1.6: A photoconductive switch for generation and detection of THz radiation.

generation and detection of THz radiation [48]. To capture the THz waves, a sub-sampling technique is employed. In this technique, the laser pulse is delayed and the sampling window is shifted to repeat the measurement. This pulse generation and detection technique is used in THz time-domain spectroscopy (THz-TDS) systems [49]. However, an integrated germanium-based THz impulse radiator with an optical waveguide coupled is introduced recently as a photoconductive switch [50, 51]. This design is fabricated in a low-cost silicon-on-insulator (SOI) process, which provides a germanium thin film that can be used as a photoconductive material. Silicon-based technologies provide a high level of integration and low fabrication costs compared to other technologies such as III–V semiconductors [52].

Although THz-TDS is a strong technique, it suffers from the high power consumption, high cost, and bulky measurement setups due to requirement of having a femtosecond laser source. Moreover, the need of having a mechanical delay line to shift the laser pulse in the sub-sampling scheme makes such systems impractical for some applications. Thus, there has been a tendency to implement THz systems in electronics, including both silicon and III–V substrates.

Compared with the silicon-based devices, non-silicon-based solutions such as III-V semiconductors exhibit better high-frequency performance due to their high breakdown voltages and maximum oscillation frequency (f_{max}). The frequency f_{max} represents the frequency at which the unilateral gain of the transistor becomes unity [53]. This is an important metric because it fundamentally defines the maximum frequency at which the device can provide power amplification. For example, InP-based high-electron mobility transistors (HEMTs) have reached (f_{max}) of 1.5 THz, enabling the first solid-state amplifier beyond 1 THz [54]. However, III-V technologies suffer from high power consumption, high fabrication costs, low scalability, and low level of integration compared to standard silicon technologies. Moreover, silicon-based technologies are compatible with complementary metal–oxide–semiconductor (CMOS), enabling the design of complex analog and mixed-signal circuits [55]. It is worth mentioning that heterojunction bipolar transistors (HBTs) exhibit superior high-frequency performance compared to the field-effect transistors (FETs) due to their high transconductance, high output conductance, and voltage handling capability [56].

The transistor speed in silicon-based technologies has been improving over the last several decades, making electronic-based THz systems a low-cost alternative for optical-based systems. One of the main challenges in realizing efficient integrated THz systems in silicon is the generation and detection of signals beyond the f_{max} of a transistor, which does not exceed 500 GHz [57].

Continuous-wave (CW) signal generation/detection or pulse-based systems are the two main approaches for THz electromagnetic wave generation and detection beyond the f_{max} of the transistor in the silicon-based technologies.

As shown in Fig. 1.7, for CW signal generation, there is, ideally, a Dirac delta function in the frequency spectrum. However, the frequency spectrum for the impulse-based systems has a large BW because of its very short duration in time. Due to the repetitive generation of these impulses, the frequency spectrum contains discrete frequency tones. The spacing between two adjacent tones in the frequency spectrum is determined by the repetition frequency (f_0) of impulses. Consequently, by changing the repetition frequency of impulses in time-domain, the spacing between tones in the frequency-domain can be tuned.

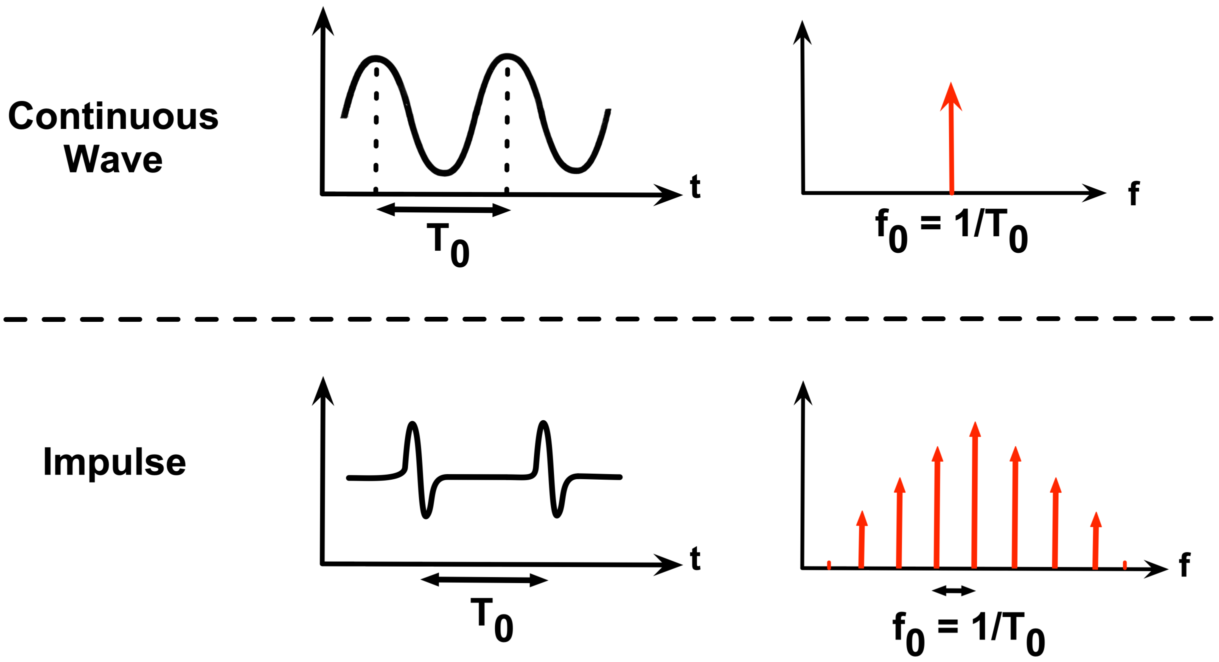

Figure 1.7: Time- and frequency-domain visualizations of continuous-wave signal and impulse train.

In the CW approach, an oscillator is used to generate a fundamental signal below the f_{max} of the transistor [58], and higher order harmonics are produced by either utilizing a frequency multiplier [59, 60] or extracting high-order harmonics of fundamental oscillations frequency [61, 62]. The BW of CW THz generation and detection systems is narrow, and multiple sources and detectors are needed to cover the entire mm-wave and THz band. The other challenge of this approach is the necessity of having a high-power local oscillator to downconvert or upconvert the signal, which is challenging in the mm-wave and THz regimes.

On the other hand, pulse-based systems have a short pulse duration in the time-domain that exhibit a broad comb-shaped spectrum in the frequency domain. In other words, such systems distribute the total radiated power to a broad frequency range, which makes them a promising solution for broadband applications such as spectroscopy. Moreover, by time-interleaving the picosecond impulse-radiating arrays, ultra-high data-rate communication links are feasible.

Traditionally, an oscillator followed by a fast switch has been used to produce ultra-short impulses in silicon technology [63]. There are several limitations associated with these approach: first, it is required to use a phase-locked loops (PLLs) and delay-locked loops (DLLs) in order to synchronize the switching operations and the oscillator due to random phase variation of the free-running on-chip oscillator [64]. Second, the implementation of PLLs and DLLs increases system complexity, power consumption, and die area significantly that limit the scalability of such systems. Third, due to the low isolation of the switch at mm-wave and THz frequency ranges, the performance of the system is degraded. Finally, the transient response of the switch limits the BW of the generated impulses.

Recently, an oscillator-free architectures have been introduced to radiate [65, 66, 67] and detect [68, 69] signals in the mm-wave and THz regime. Such systems utilize a nonlinear current-switching mechanism to generate a reference frequency comb, overcoming the aforementioned limitations for the oscillator-based architectures. The same technique is used in the design procedure of the circuit blocks, described in the chapter 2 and chapter 3 of this dissertation. A nonlinear current switch generates a reference THz frequency comb. This reference frequency comb is radiated through the air by coupling to the broadband on-chip antenna in the transmitter. Moreover, the reference comb can be employed as an LO signal in the receiver to downconvert the received mm-wave and THz signal to the low-frequency intermediate frequency (IF) band.

1.4 Organization

Having provided the background on THz applications and techniques, an in-depth overview of my research is provided in the following chapters of this dissertation, which includes mm-wave and THz circuit design and measurement. This thesis presents a fully integrated ultra-short pulse radiator and detector in silicon-based platforms that can radiate and detect electromagnetic waves in the mm-wave and THz regimes. This dissertation is organized as follows:

Chapter 2 describes a fully integrated laser-free oscillator-free terahertz impulse radiator in silicon. This THz transmitter radiates 2.5 picosecond impulses, corresponding to a frequency comb with 1.052 THz bandwidth. In addition, this chip can transmit 4 Gb/s data with the non-return-to-zero inverted on-off keying modulation scheme. A 2 m specular non-line-of-sight communication link for long-range wireless applications is built using this transmitter, parabolic reflector antennas, and a plane mirror. This chip is fabricated in 130 nm SiGe BiCMOS process technology and occupies a total die area of 1.26 mm^2 and consumes 206 mW of dc power.

Chapter 3 introduces an oscillator-free frequency comb-based coherent detector with an on-chip antenna for sensing and imaging applications in mm-wave and THz frequencies. This design detects arbitrary signals from 20 GHz up to 500 GHz with 2-Hz frequency resolution. A peak sensitivity of -100 dBm is measured with 1 KHz resolution bandwidth (RBW). The frequency spacing in the on-chip reference frequency comb is tunable and set to 4 GHz in this work. A chip-to-chip dual-frequency comb measurement setup is successfully implemented by using this receiver and the impulse transmitter (chapter two). This setup is characterized in the 20-220-GHz frequency range. This chip is fabricated in 130 nm SiGe BiCMOS process technology.

Chapter 4 presents a long-path THz communication channel characterization in the frequency range of 0.32–1.1 THz using a custom, silicon-based THz pulse radiator chip. A specular link was created using the impulse radiator, parabolic reflector antennas, a plane mirror, and a downconverter mixer. The THz channel was characterized up to a distance of 110 m. The measurement results demonstrate channel path loss, atmospheric absorption, and low-loss frequency windows suitable for wireless links in the THz range.

Finally, chapter 5 concludes this thesis.

CHAPTER 2

A Fully Integrated Laser-free Oscillator-free Terahertz Impulse Radiator in Silicon

This chapter presents a fully integrated impulse radio transmitter that has an ultra-broadband frequency comb in the millimeter-wave and terahertz regimes with a 2 Hz frequency resolution as an on-chip reference signal, published in [70]. The spectral purity due to the extremely narrow spectral line-width makes this design a solution for a wide range of high-resolution sensing applications, including narrow absorption line spectroscopy, radar, imaging, and remote sensing. Moreover, the area-efficient and low-power topology allows scaling up the design for large array implementation. This work also includes an on-chip slot bow-tie antenna with a maximum gain of up to +20 dBi, including the gain of the silicon lens. This chip radiates 2.5 picosecond impulses, corresponding to a frequency comb with 1.052 THz bandwidth. In addition, this chip can transmit 4 Gb/s data with the non-return-to-zero inverted on-off keying modulation scheme. A 2 m specular non-line-of-sight communication link for long-range wireless applications is built using this transmitter, parabolic reflector antennas, and a plane mirror. This chip is fabricated in 130 nm SiGe BiCMOS process technology and occupies a total die area of 1.26 mm^2 and consumes 206 mW of dc power.

2.1 Introduction

THz frequencies promise larger bandwidths for wireless links and higher resolutions for radar, imaging, and remote sensing systems [1, 2]. The need for a higher data rate in communication systems and higher resolution in sensing/imaging systems pushes the operating frequency into millimeter-wave/THz regimes. In the last decade, remarkable improvements have been made in the specifications of accessible THz technologies in photonics and electronics. The birth of 5G systems and the definition of the 6G standard for communication and sensing are evidence of the increasing interest in the exploitation of THz frequencies for ultra-broadband wireless communication. At the same time, pushing the operating frequencies beyond 300 GHz has been among the popular research topics in academia.

In photonics, femtosecond laser-based photoconductive antennas have been utilized for radiating short pulses [49], but such setups are bulky and expensive, making them impractical for some applications. In addition, femtosecond lasers suffer from poor linewidth and phase noise. Thus, there has been a tendency to implement THz systems in electronics.

In electronics, continuous-wave (CW) or impulse-based systems have been used for mm-wave/THz generation/detection beyond the f_{max} of transistors. The transistor speed in silicon-based technologies has been improving over the last several decades, making electronic-based THz systems a low-cost alternative for optical-based systems. Silicon-based technologies provide a high level of integration and low fabrication costs compared to other technologies such as III–V semiconductors. One of the main challenges in developing integrated THz systems in silicon is the generation/detection of signals beyond the f_{max} of a transistor.

In CW systems, since it is narrowband, all the power is concentrated in a narrow frequency range and the average power is relatively high [59, 60]. However, such systems consume more power and require a high-power mm-wave/THz LO signal to upconvert the signal, which is challenging in mm-wave and THz regimes.

Pulse-based systems, on the other hand, provide broadband spectral information because of their short durations in the time-domain [65, 66, 67, 68, 69]. Consequently, the radiated power is distributed over a broad frequency range. The active-time in impulse-based systems is short, and as a result, the power consumption is lower as compared with CW transceivers.

Recently, an oscillator-less, silicon-based impulse radiator has been reported [78, 79] that radiates sub-10 ps impulses and utilizes a direct digital-to-impulse (D2I) method, which is also used in this design. A non-linear, high-speed switch is used to generate ultashort pulses and a broadband on-chip antenna radiates them.

This chapter presents a fully integrated impulse radiator that radiates an ultra-broadband frequency comb in the millimeter-wave and terahertz regimes with a 2 Hz frequency resolution. It also includes an on-chip slot bow-tie antenna with a maximum gain of up to +20 dBi, including the gain of the silicon lens. This chip radiates 2.5 picosecond impulses, corresponding to a frequency comb with 1.052 THz bandwidth. In addition, this chip can transmit 4 Gb/s data with the non-return-to-zero inverted on-off keying modulation scheme. A 2 m specular non-line-of-sight communication link for long-range wireless applications is built using this transmitter, parabolic reflector antennas, and a plane mirror. This chip is fabricated in 130 nm SiGe BiCMOS process technology and occupies a total die area of 1.26 mm^2 and consumes 206 mW of dc power.

The rest of this chapter is organized as follows. First, the concept and theoretical analysis of the THz radiator is described. It is followed by design details and simulation results of a frequency comb-based radiator, a 4-Gb/s impulse-based transmitter, and an ultra-broadband on-chip antenna. Second, the measurement setups and results of the fabricated chip is presented, including characterization of the transmitter in the frequency- and time-domain.

2.2 Circuit Architecture

2.2.1 Broadband THz Impulse Radiator

Previously the nonlinearity of a bipolar junction transistor (BJT) was employed to generate a frequency-comb [65], which also is taken into account in this design (Fig. 2.1). This nonlinear current-switching method is similar to the mechanism of switching power amplifier, where a shorted coplanar waveguide transmission line acts as an inductor in the collector of Q1.

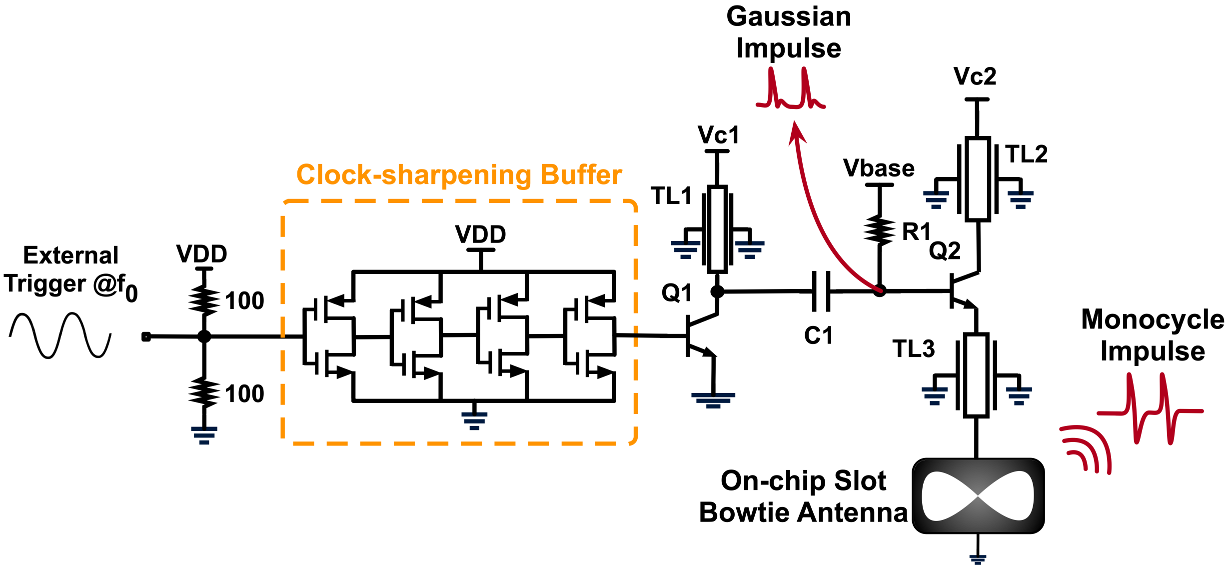

Figure 2.1: Circuit schematic of THz impulse radiator.

The external trigger signal, after passing through a clock-sharpening buffer stage, becomes a square-wave signal that switches Q1. When Q1 is on, energy is stored in the CPW transmission line. By the on-to-off switching of Q1, the stored energy in the previous step is revealed as a sharp Gaussian-shape impulse with the width of several picoseconds. This continuous switching results in having a train of picosecond impulses, which corresponds to an ultra-broadband frequency comb in the frequency domain. The frequency spacing between two adjacent tones in the frequency spectrum is determined by the repetition frequency of impulses (f_0). Consequently, by changing the repetition frequency of impulses in the time-domain, spacing between tones in the frequency-domain can be tuned. In this work, an external tunable trigger signal sets the repetition frequency. Moreover, the BW of this frequency comb is determined by the pulse-with of the picosecond impulses. The simulated plots of Gaussian and monocycle impulses are shown in Fig. 2.2. As it is shown in the Fig. 2.2, monocycel picosecond impulses have a full width at half maximum (FWHM) of 2.5 ps and they are generated only at the falling-edge of the external trigger signal.

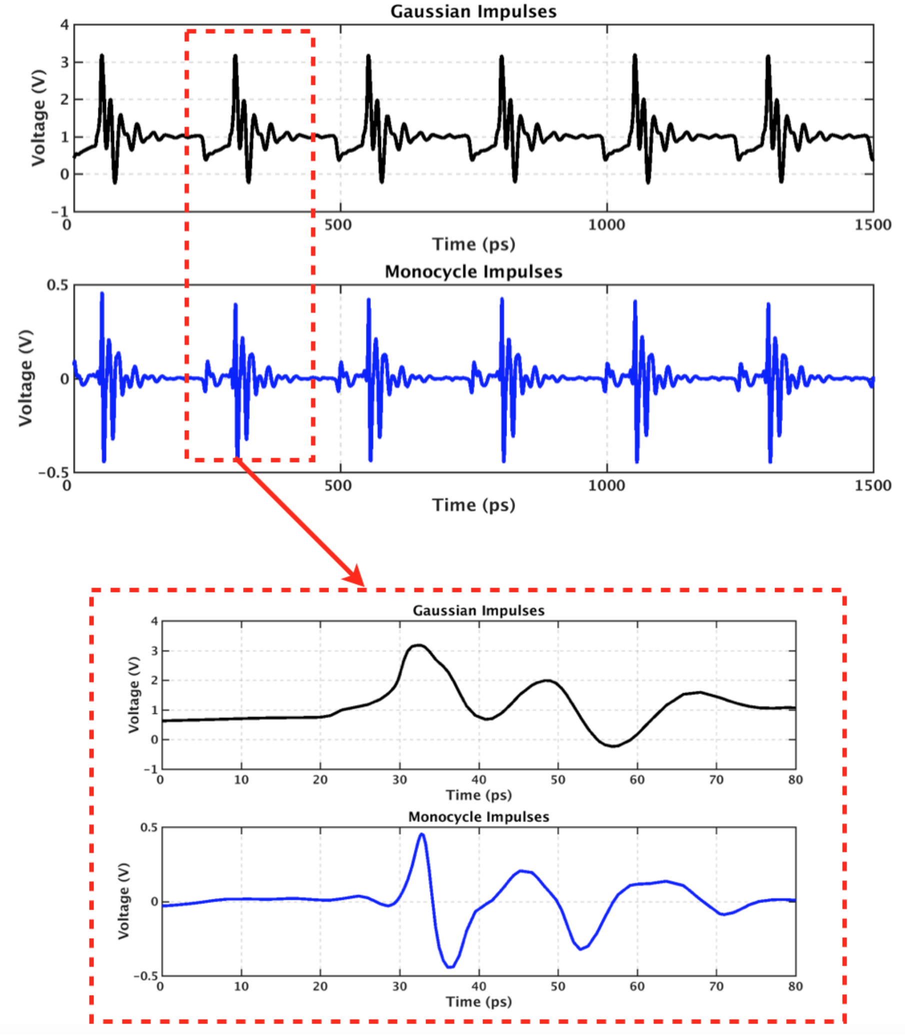

Figure 2.2: Simulation results of the Gaussian and monocycle picosecond impulses.

In Fig. 2.1, Q2 acts as a driver for on-chip antenna and passes the Gaussian-shape impulses to the on-chip antenna. The slot bow-tie antenna is a broadband on-chip antenna and changes the incoming Gaussian impulses to the monocycle impulses, which has no DC content. A hemispherical high-resistivity silicon lens is attached under the chip to eliminate the substrate modes and increase the radiation efficiency and bandwidth. The simulated frequency spectrum of the monocylce impulses is shown in the Fig. 2.3.

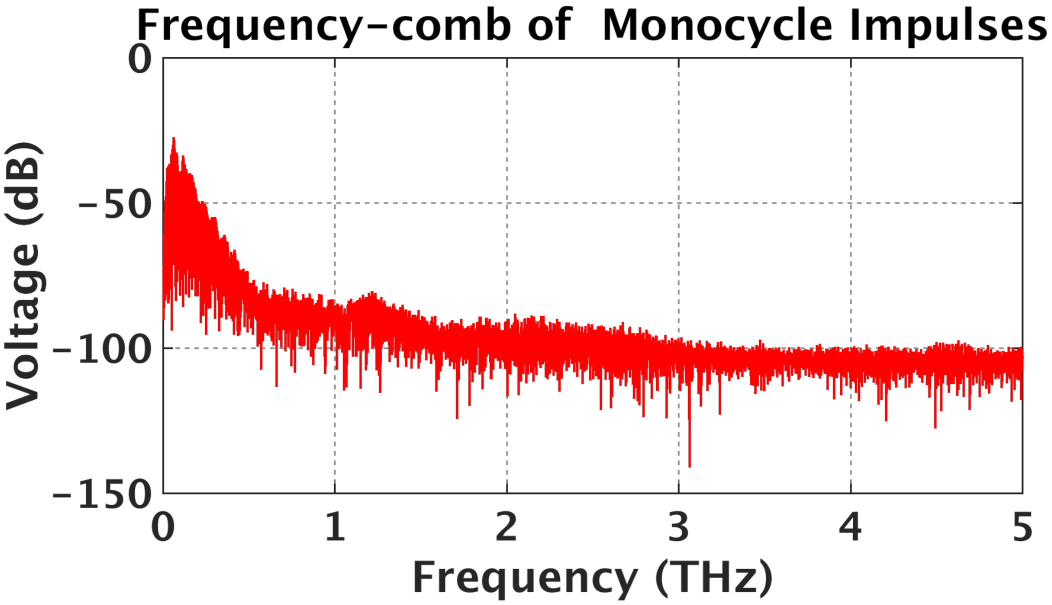

Figure 2.3: Simulated frequency spectrum of the monocylce impulses.

Additionally, the time constant at the base of Q1 plays an important role in the amplitude and the pulse-width of the picosecond impulses. As a result, an edge-sharpening buffer is employed to discharge Q1 faster (Fig. 2.4).

The simulation results of the picosecond impulses, with and without the edge-sharpening buffer, are shown in Fig. 2.5. As shown in Fig. 2.5, adding the edge-sharpening buffer results in a higher amplitude and narrower pulse-width.

2.2.2 4 Gb/s Impulse-Based Communication Transmitter

Since Q1 only generates impulses at the falling edge of the digital data, digital blocks are added to the circuit described in Fig. 2.4 in order to modify this design as a communication transmitter with the non-return-to-zero inverted (NRZI) OOK modulation scheme. The block diagram of the impulse-based transmitter for communication is shown in Fig. 2.6.

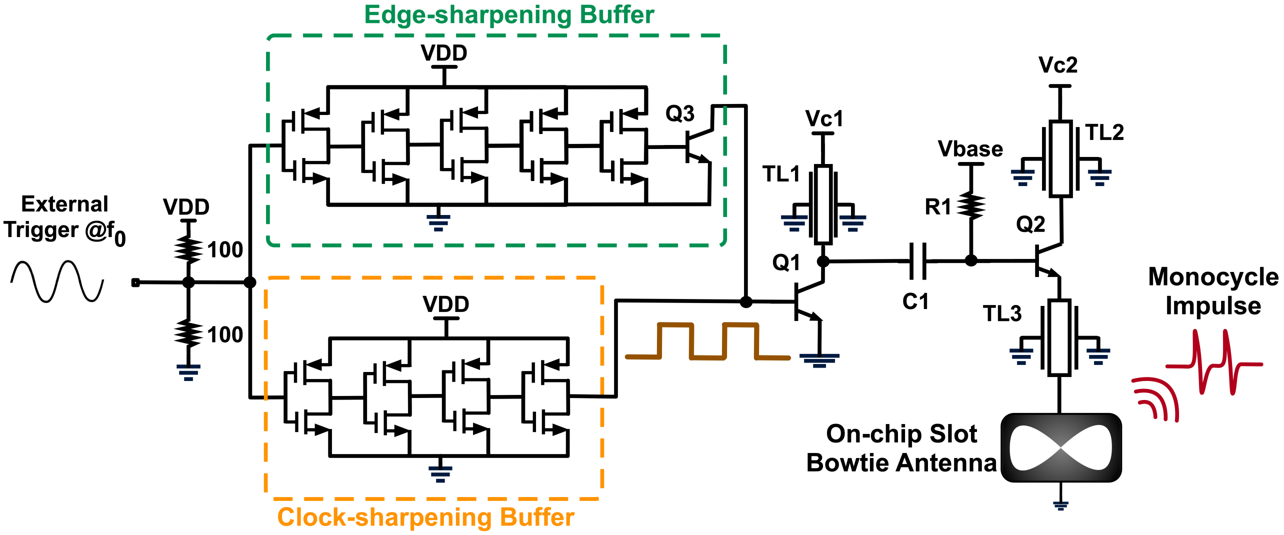

Figure 2.4: THz impulse radiator with edge-sharpenning buffer stage.

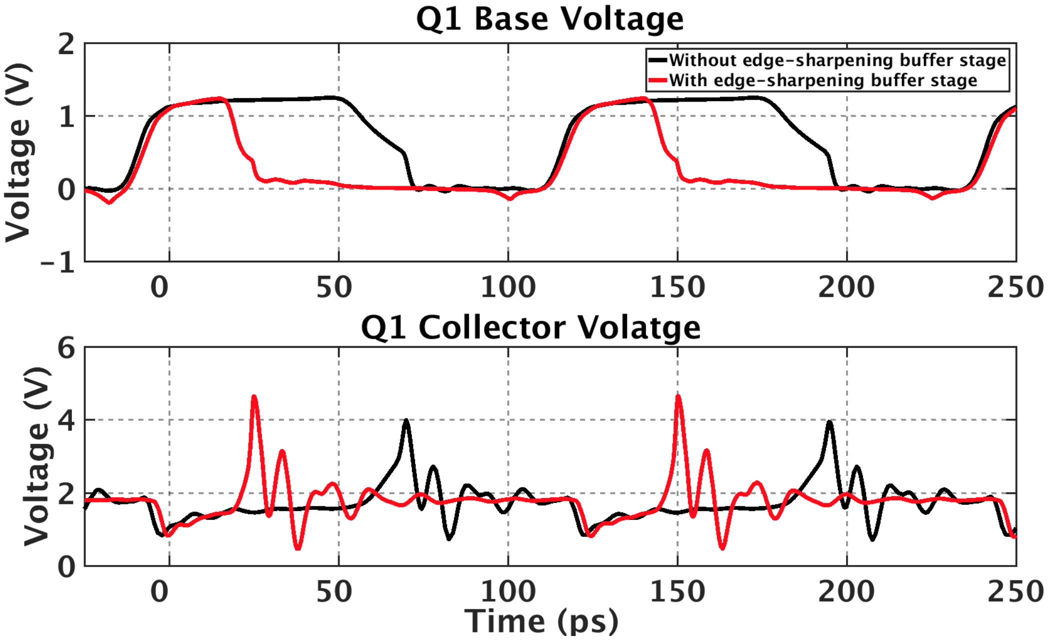

Figure 2.5: Simulation result of the picosecond impulses with/without edge-sharpening buffer stage.

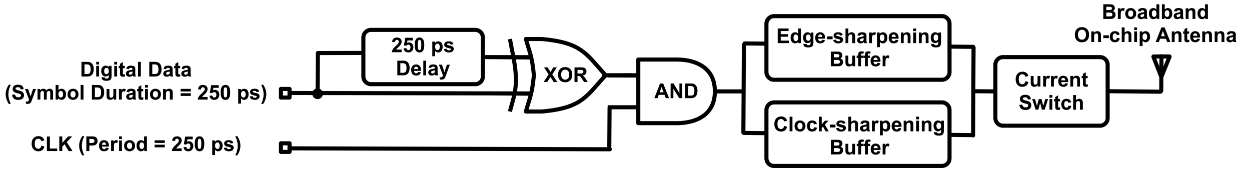

Figure 2.6: Block diagram of the impulse-based transmitter for communication.

Given that the transmitter should radiate impulses at the falling and rising edges of the digital data, an edge detector block followed by an AND gate are utilized. At the edge detector block, the digital data and a delayed version of it are fed to an XOR gate. The amount of the delay should be equal to the symbol duration of the digital signal, which is 250 ps in this design and that corresponds to a 4 Gb/s data rate. The output of the edge detector is a non-return-to-zero (NRZ) modulated signal. Since the impulse generator block only generates impulses at the falling edge of its input, we need to change this modulation from NRZ to return-to-zero and make a falling edge at the output of the edge detector. An AND gate is designed, where one input is the output of the edge detector and the other input is coming from an external signal (CLK). The symbol duration of the CLK signal is 125 ps, which is half of the amount for the digital data signal. The simulation results are shown in Fig. 2.7.

2.2.3 On-chip Impulse Antenna

An on-chip antenna is designed and employed in this chip to obtain a compact setup. An integrated antenna increases the BW and efficiency by eliminating the need of having lossy and narrowband connections to an off-chip antenna.

On-chip antennas suffer from the undesired effects of substrate modes, that propagate inside a doped silicon substrate with high dielectric constant 11.9 and low resistivity $11-16\ \Omega$.cm. Such effects make the antenna narrowband, limit the radiation efficiency and total gain, and cause ringing and non-linearity in the phase. One solution to overcome these

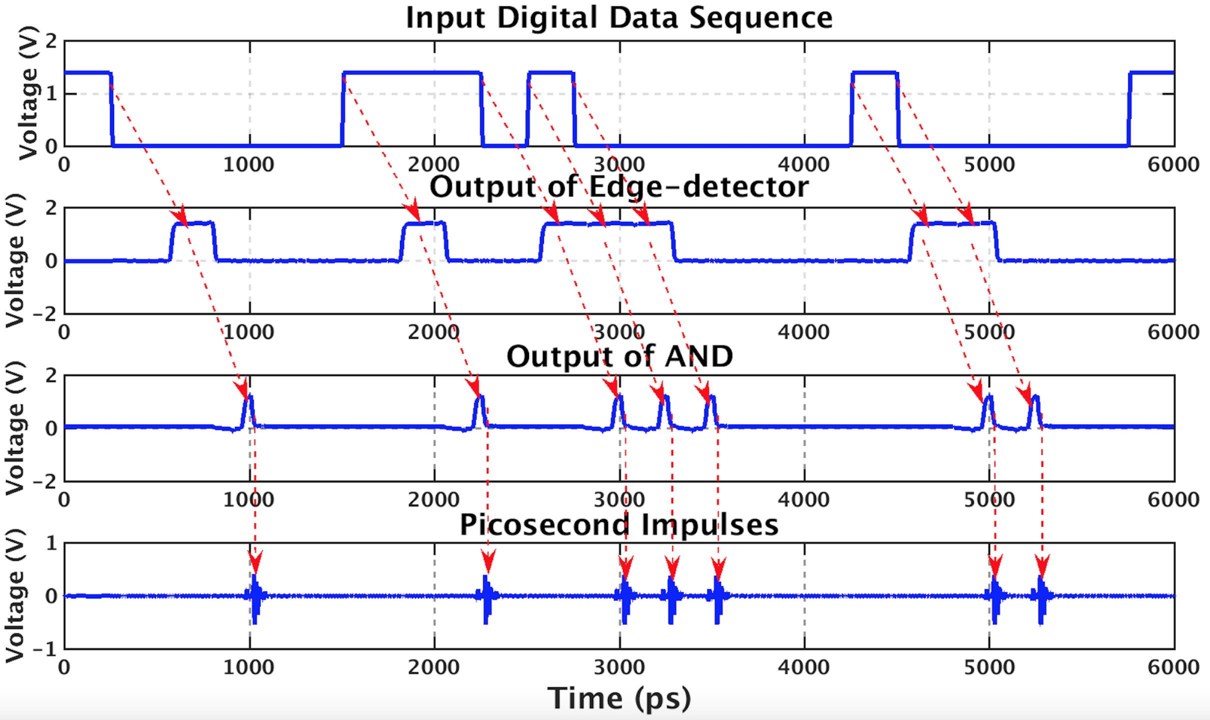

Figure 2.7: Simulation result of the impulse-based transmitter for communication.

limitations to utilize an undoped hemispherical silicon lens, assembled below the chip. This off-chip silicon lens with a diameter of 13 mm and a resistivity of 10 $K\Omega$.cm mimics a semi-infinite silicon substrate for the antenna. This solution forces the antenna to radiate the surface waves from the back side with higher radiation efficiency, gain, and BW [71].

To radiate and detect ultra-short impulses, the antenna must have a broadband impulse response with a linear phase. In additional, the circuit architecture of this chip requires an antenna that behaves like an inductor at low frequencies. A slot bow-tie antenna can satisfy the design criteria for this ultra-braodband radiation and detection. In addition, the edges of the antenna are curved to enhance its BW [72].

Fig. 2.8 shows the geometry of the antenna and the cross section of the chip with the high-resistivity silicon lens.

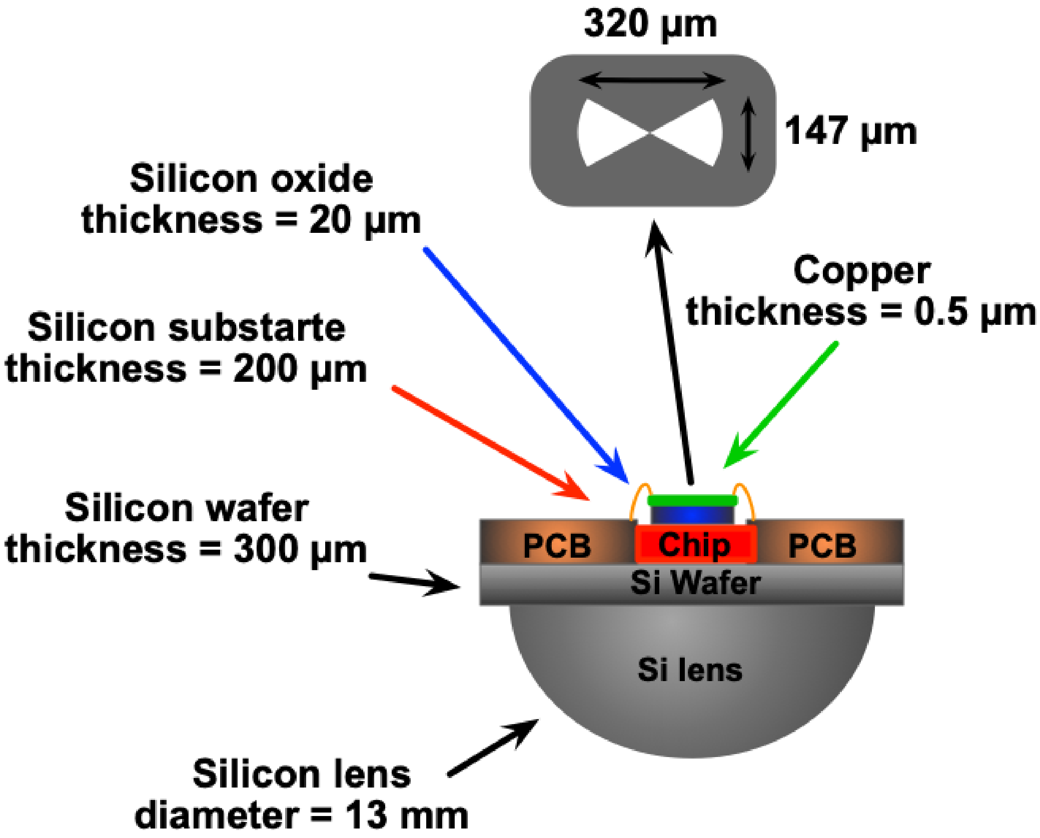

Figure 2.8: Geometry of the antenna and a cross section of the chip with the high-resistivity silicon lens.

This on-chip antenna with a length of 320 μm and a width of 147 μm is fabricated in the MQ layer in the 130 nm SiGe BiCMOS process technology (8HP) with a thickness of 0.5 μm. This antenna structure is simulated using CST Microwave Studio tool. The impedance and s11 plots are shown in Fig. 2.9.

The impedance plot shows that this on-chip antenna has a ultra-broadband flat impedance after its first resonance. This flat impedance gives us the opportunity to match the antenna to our circuit in a broadband frequency range. The S11 plot proves the ultra-broadband impedance matching to a 50 Ω source.

The efficiency and gain plots are shown in Fig. 2.10.

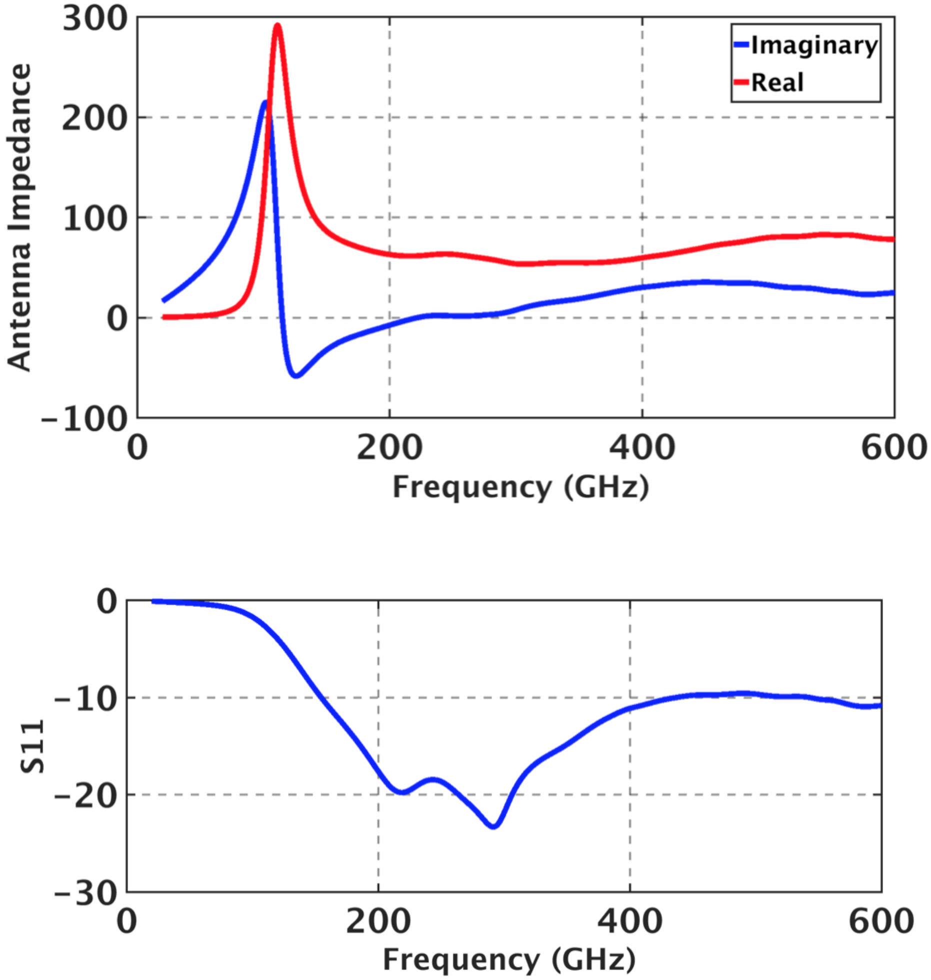

Figure 2.9: Antenna impedance and S11 plots, simulated by CST Microwave Studio

The efficiency plot shows the effect of adding the silicon lens on the total radiation efficiency. A maximum efficiency of 67% is achieved by adding the silicon lens to back-side of the antenna. Finally, the gain plot shows the gain of this antenna at $\phi = 0°$ surface. The difference between the $\theta = 0°$ and $\theta = 180°$ plots illustrates that this antenna is designed for the back-side radiation. Moreover, the difference between the gain plots with and without the silicon lens proves the benefits of adding the silicon lens. The maximum gain of +20 dBi, including the silicon lens gain, is achieved in this simulation.

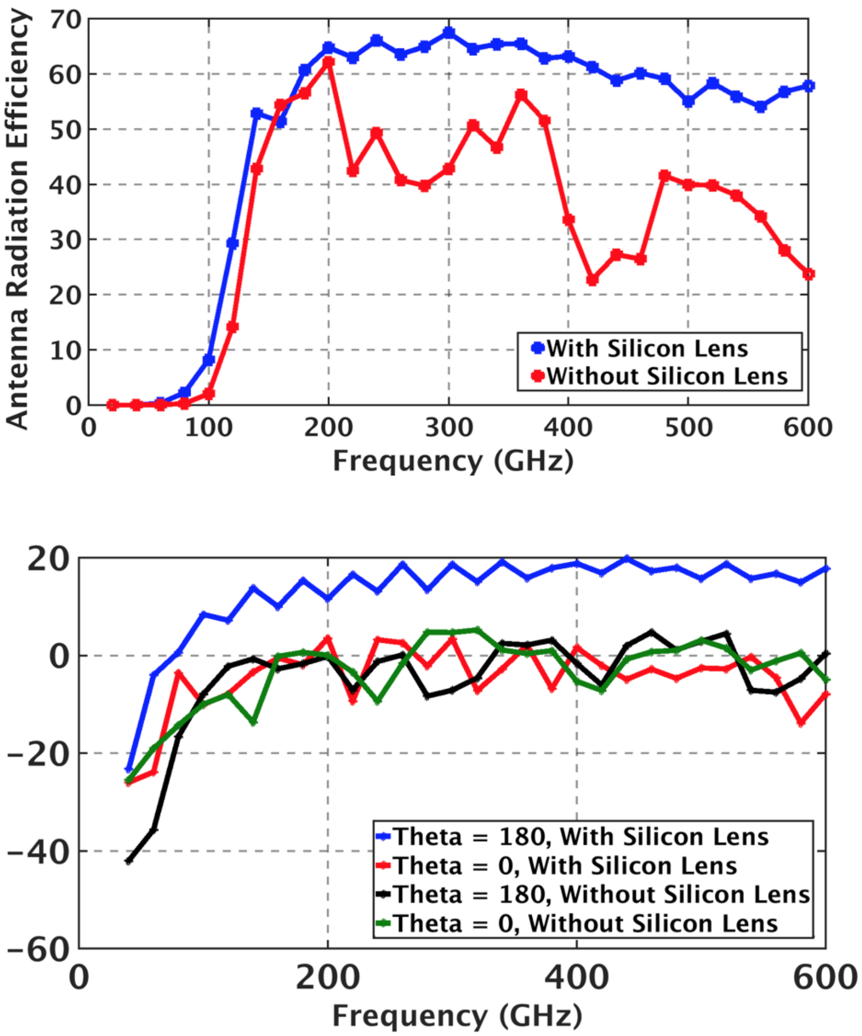

Figure 2.10: Antenna impedance and S11 plots, simulated by CST Microwave Studio

2.3 Measurement Setups and Results

This section describes the measurement setups and results in the characterization of the performance of this chip. In the first step, the chip is characterized in the frequency-domain. In the second step, time-domain measurement setup and results are presented. In the next step, the radiation pattern of the on-chip antenna is shown. In the last step of measurement, this chip is utilized as an impulse-based transmitter for communication.

This chip is fabricated in 130 nm SiGe BiCMOS process technology and occupies a total die area of 1.26 mm^2. Fig. 2.11 shows the die photograph of the chip. The total dc power consumption is 206 mW with a 1.2 V power supply. A hemispherical, high-resistivity silicon lens is attached under the chip to eliminate the substrate modes and increase the radiation efficiency and BW.

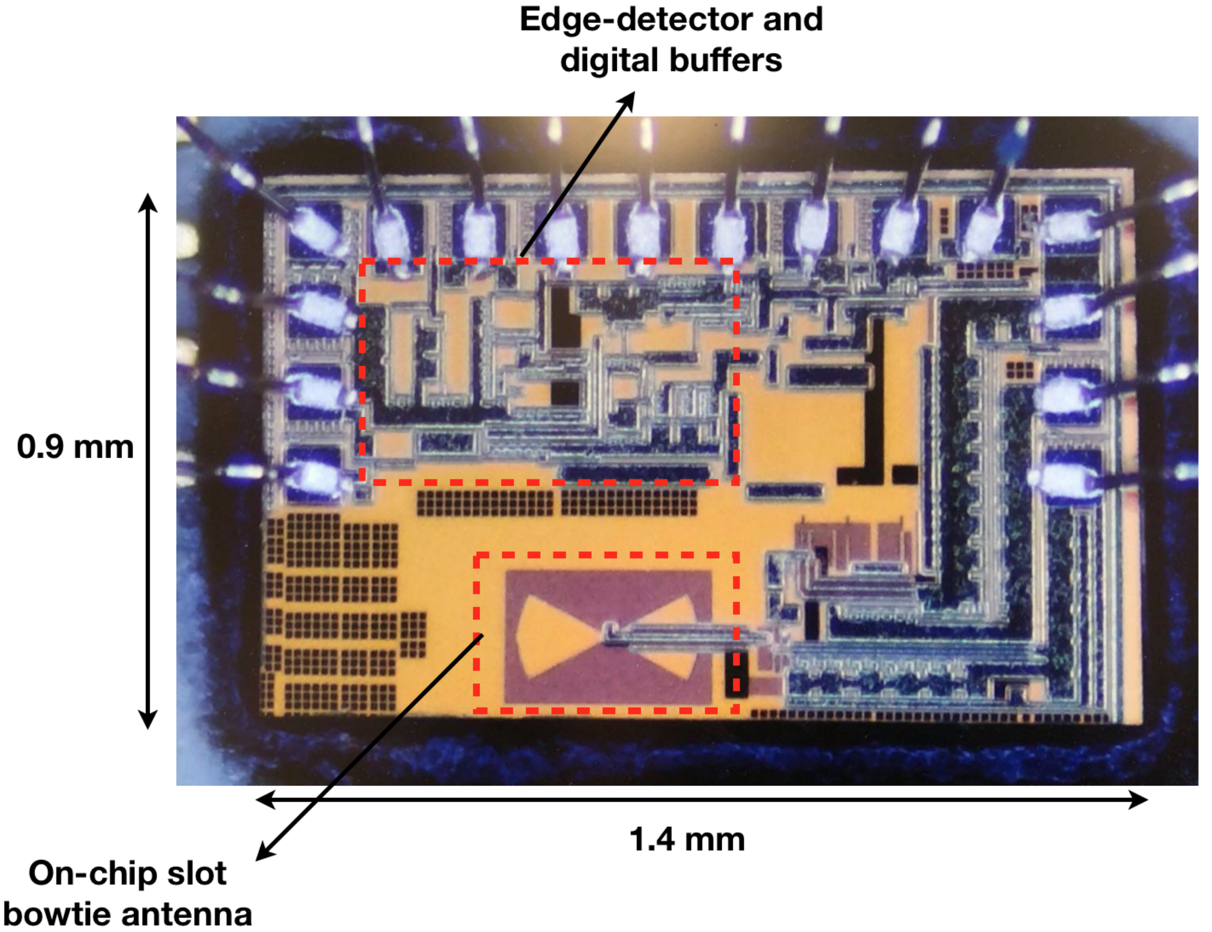

Figure 2.11: Micrograph of THz radiator chip.

2.3.1 Frequency-domain Measurement

The performance of the chip in TX mode is characterized using a frequency-domain measurement setup, as shown in Fig. 2.12. A Keysight N9030A PXA signal analyzer is used with VDI WR-2.2, 1.5, and 1.0 spectrum analyzer extension (SAX) modules and horn antennas to cover the 330–500, 500–750, and 750–1100 GHz frequency bands, respectively. The chip is fed by a 4 GHz trigger signal with an 11 dBm power, which is generated by a Keysight E8257D PSG signal generator. As a result, the spacing between adjacent tones in the frequency comb is set to 4 GHz.

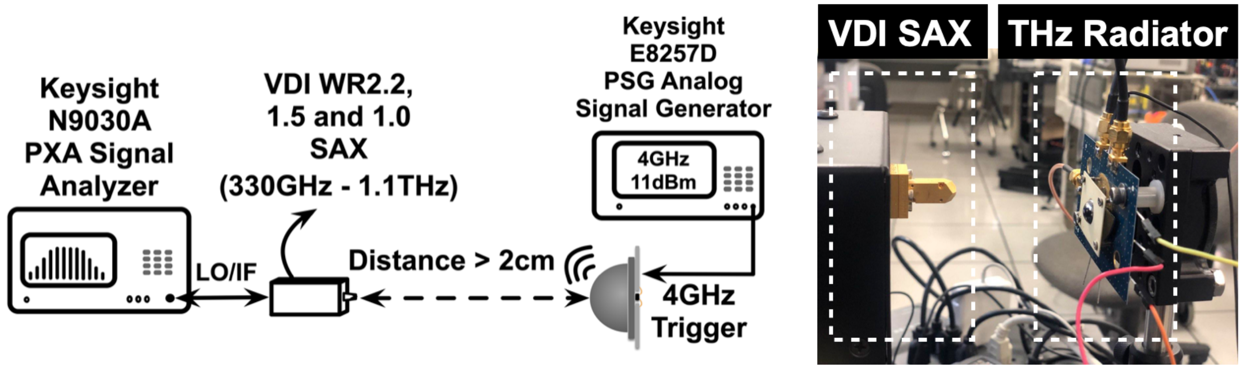

Figure 2.12: Frequency-domain measurement setup of THz impulse radiator.

Frequency tones are measured at the harmonics of 4 GHz, from 328 GHz up to 1052 GHz. The effective isotropic radiated power (EIRP), as shown in Fig. 2.13, is taken after de-embedding the free space path loss by using the Friis equation, conversion loss of mixers, RX antenna gain, and antenna loss. Frequency tones below 328 GHz cannot be measured due to our lack of instruments.

Measured power of frequency tones at 100 and 600 GHz for various distances between the VDI SAX module and the chip are also plotted in Fig. 2.14. In this plot, the power levels are normalized to the power at the closest measured distance. As clearly shown in Fig. 2.14, the received power drops fast in high frequency tones due to the high atmospheric loss for high frequencies.

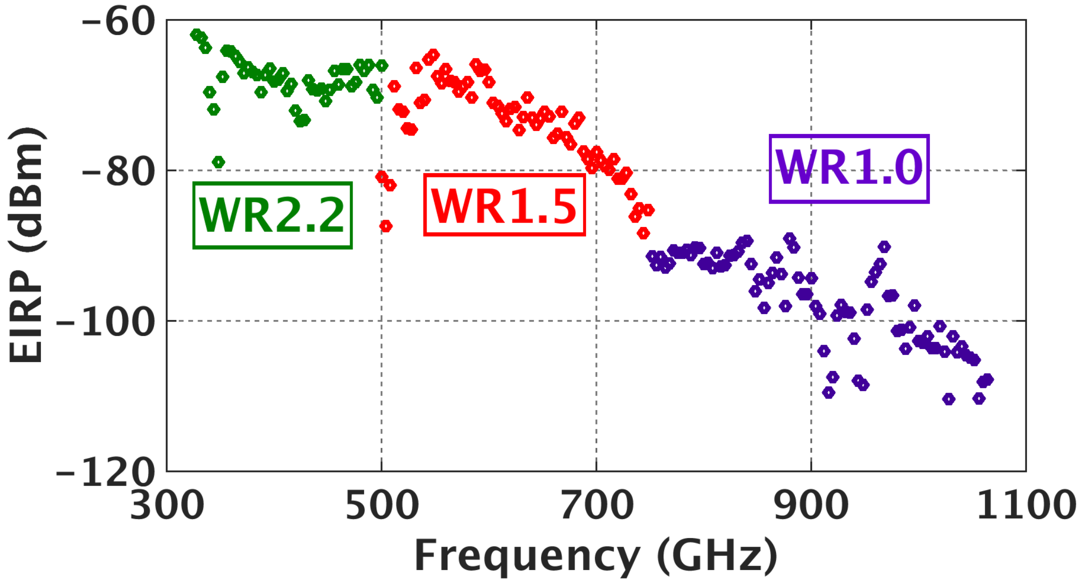

Figure 2.13: Frequency-domain measurement result of THz impulse radiator.

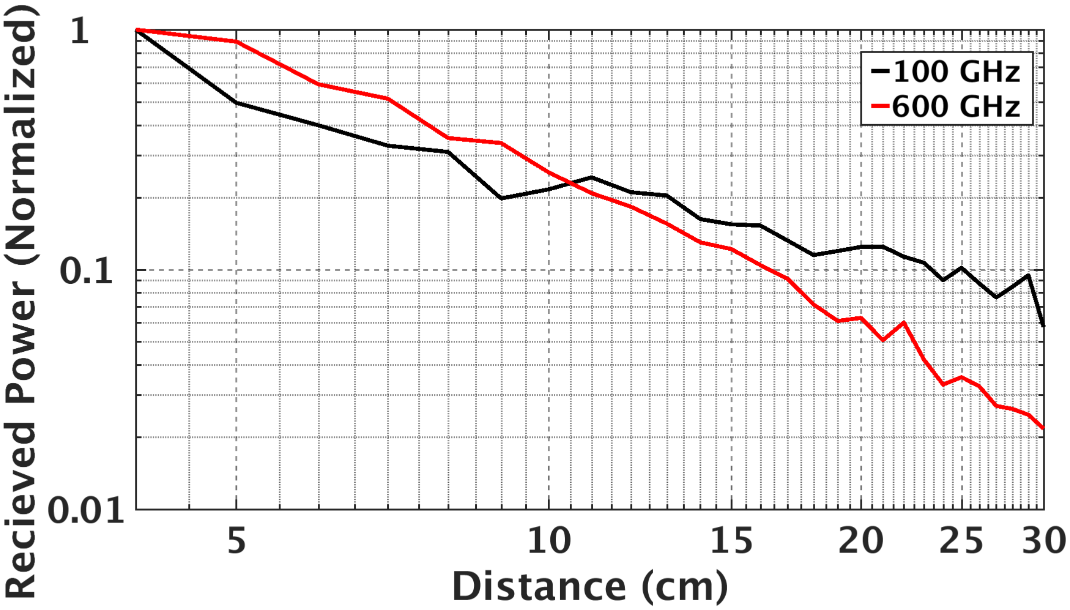

Figure 2.14: Normalized measured power at 100 and 600 GHz versus distance.

2.3.2 Time-domain Measurement

An ultra-broadband receiver and also antenna are required to sample the radiated picosecond impulses in the time-domain. Consequently, the available sampling oscilloscopes with limited BW (∼70 GHz) are not suitable to capture impulses with a few picosecond pulse-width. In additional, given that the receiving antenna should have a linear phase response, pyramidal horn antennas cannot be used as a receiving antenna [73].

Given this limitation, an Advantest TAS7500TS femtosecond-laser-based THz sampling system is used for the time-domain characterization of the radiated picosecond impulses. This is a THz time-domain spectroscopy (THz-TDS) system equipped with a PCA [37, 49] that has a broadband BW. The measurement setup is shown in Fig. 2.15. The Advantest THz-TDS system operates based on the dual-heterodyne-mixing mechanism. Two 50 MHz femtosecond lasers with a 5 Hz difference in their repetition frequencies are locked in this THz-TDS system. This 5 Hz difference enables the detector PCA to sample a 20 ns-long THz wave radiated by the emitter PCA in a 200 ms period.

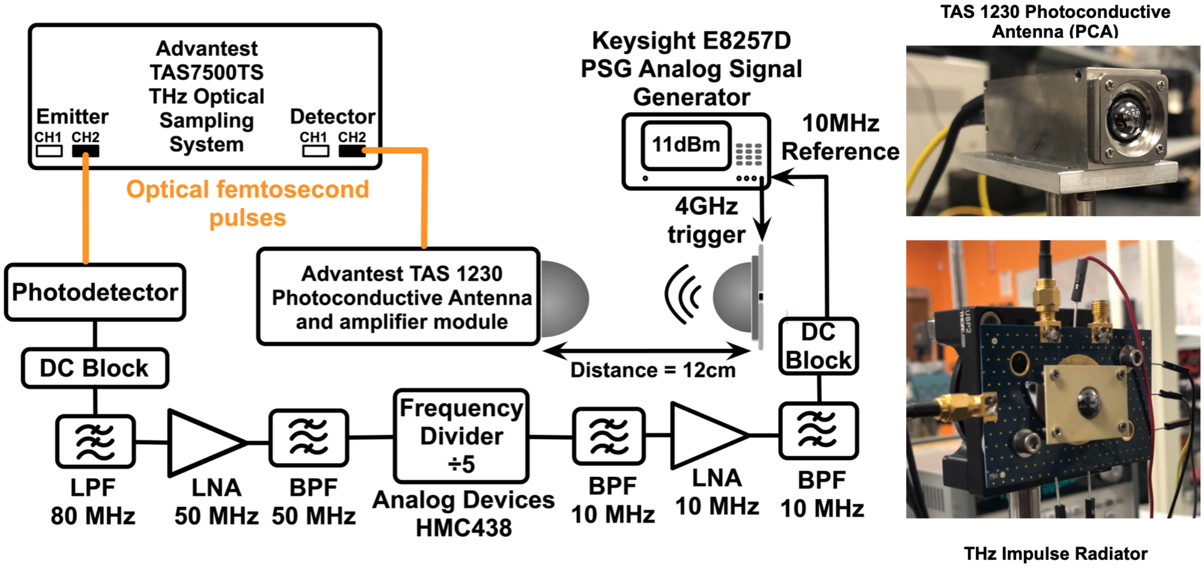

Figure 2.15: Time-domain measurement setup of THz impulse radiator.

In this measurement, the emitter PCA of the Advantest THz-TDS system is replaced by our chip, and the radiated picosecond impulses are captured by the Advantest TAS1230 PCA detector module. A custom synchronization chain is used to lock the Keysight E8257D signal generator and, consequently, the chip with the Advantest THz-TDS system. A full width at half maximum (FWHM) of 2.5 ps with 1024 averaging is measured with a 12 cm distance, which is also shown in Fig. 2.16.

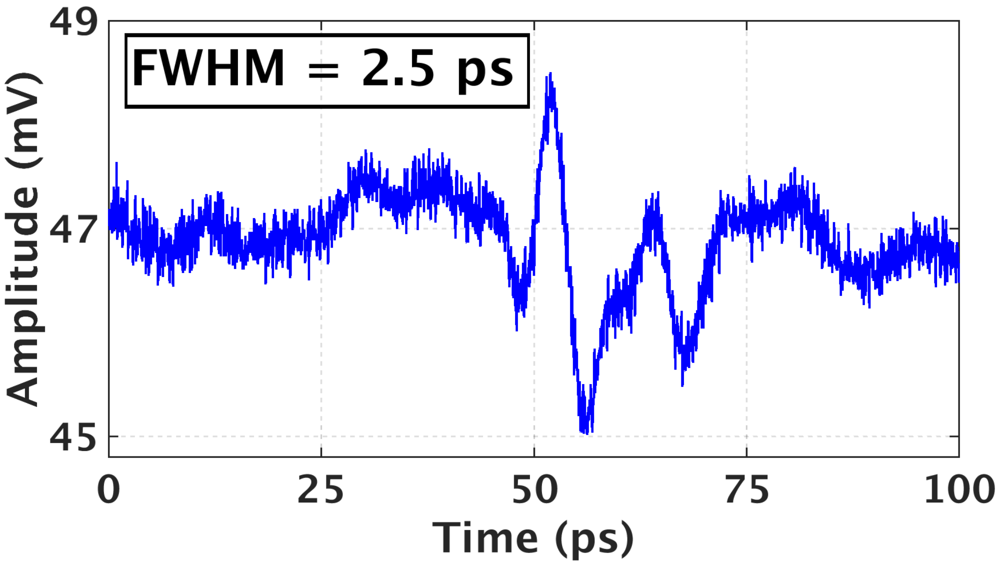

Figure 2.16: Time-domain measurement result of THz impulse radiator.

2.3.2.1 Antenna Radiation Pattern Measurement

A two-dimensional (2D) rotation stage is used to measure the frequency-domain radiation pattern of the chip. This 2D stage rotates the chip by 180 degrees to measure E and H fields. The E-plane is measured at $\phi = 90°$ surface and the H-plane is measured at $\phi = 0°$ surface, both at 600 GHz by placing the VDI WR1.5 SAX and horn antenna at a 12 cm distance. Fig. 2.17 shows the measured E-plane and H-plane radiation patterns.

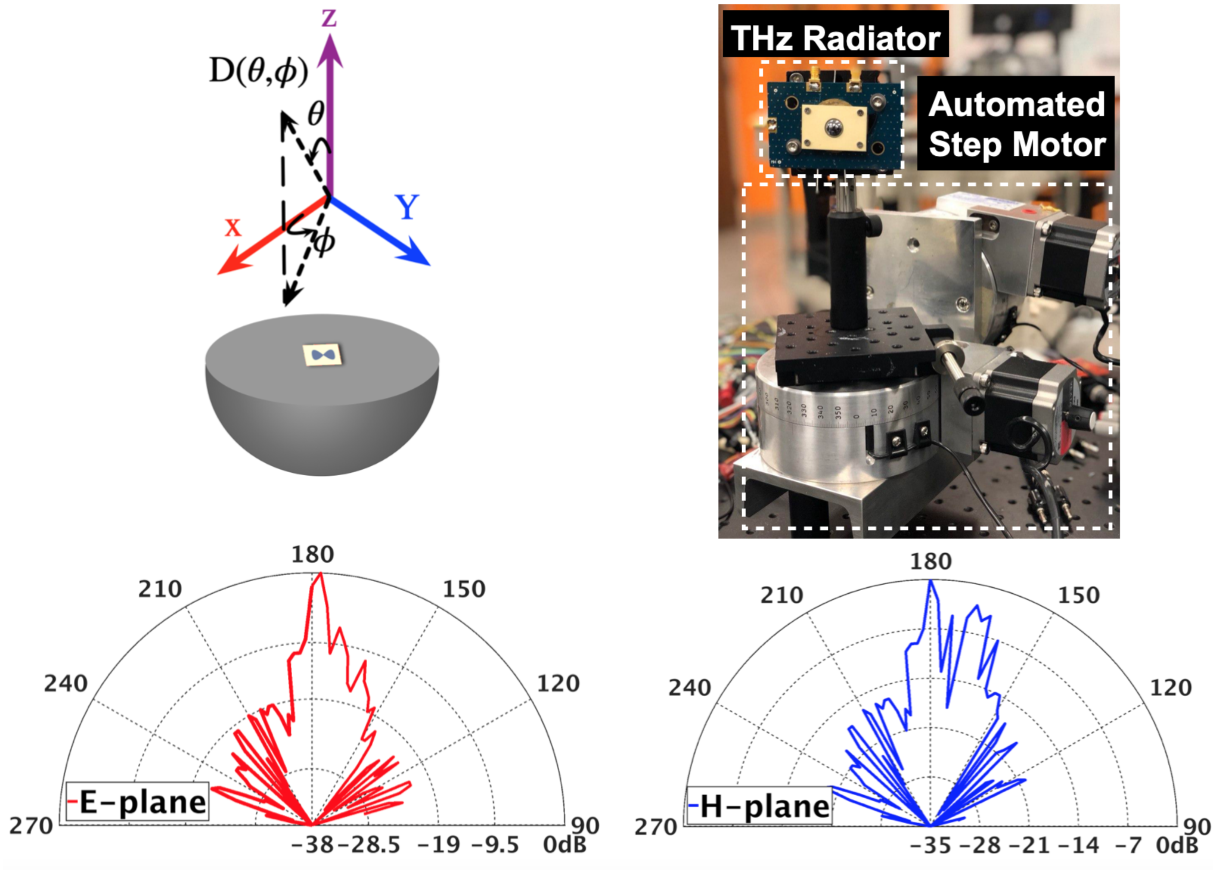

Figure 2.17: Antenna E-plane and H-plane radiation pattern measurement setup and results, measured at 600 GHz.

2.3.3 Communication Transmitter Measurement

The measurement setup shown in Fig. 2.18 is used to measure the performance of this chip as a wireless communication transmitter. Acquiring the time-domain waveform of a picosecond impulse signal is challenging. The receiving antenna requires large BW and constant group delay. In prior impulse radiating works, [63, 74], horn antenna were utilized to measure the picosecond impulses. However, horn antennas have a nonlinear phase response and sharp lower cut-off frequency, resulting in dispersion and distortion in the measured signal. Even broadband antennas such as log-periodic dipole are not suitable to acquire picosecond

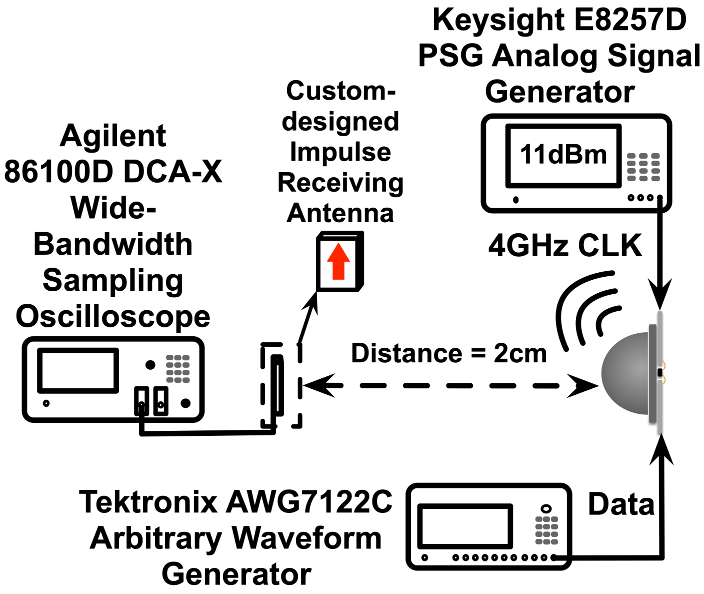

Figure 2.18: Measurement setup for THz impulse communication transmitter.

impulses due to their group delay variation. Therefore, a custom printed circuit board-based inverted cone planar antenna is utilized as the receiving antenna in this experiment for time-domain characterization (Fig. 2.19).

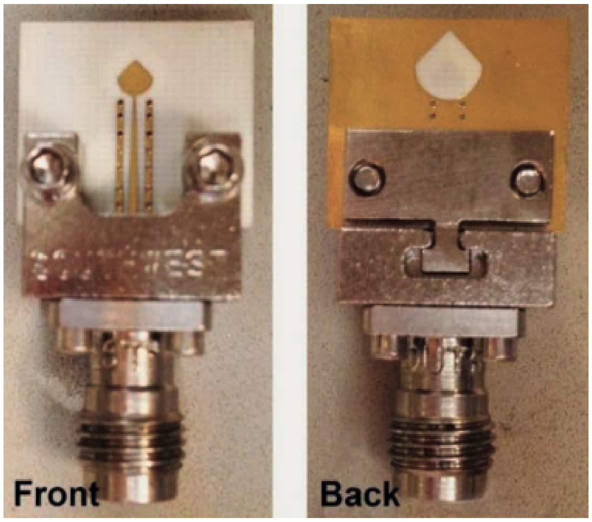

Figure 2.19: Custom-designed impulse receiving antenna.

This custom-designed antenna is fabricated on a two layer Rogers board with a permittivity of 3.5. An Agilent 86100D DCA-X sampling oscilloscope with 70 GHz BW is employed in conjunction with the custom-designed antenna to capture the picosecond impulses.

Given that the BW of the sampling oscilloscope is limited, high-frequency components are filtered out, and only frequency components below 70 GHz are captured, resulting in a widening of the original impulse. A FWHM of 15 ps is measured in this experiment (Fig. 2.20). The distance between the chip and the custom-designed receiving antenna is 2 cm, and the digital data is periodic.

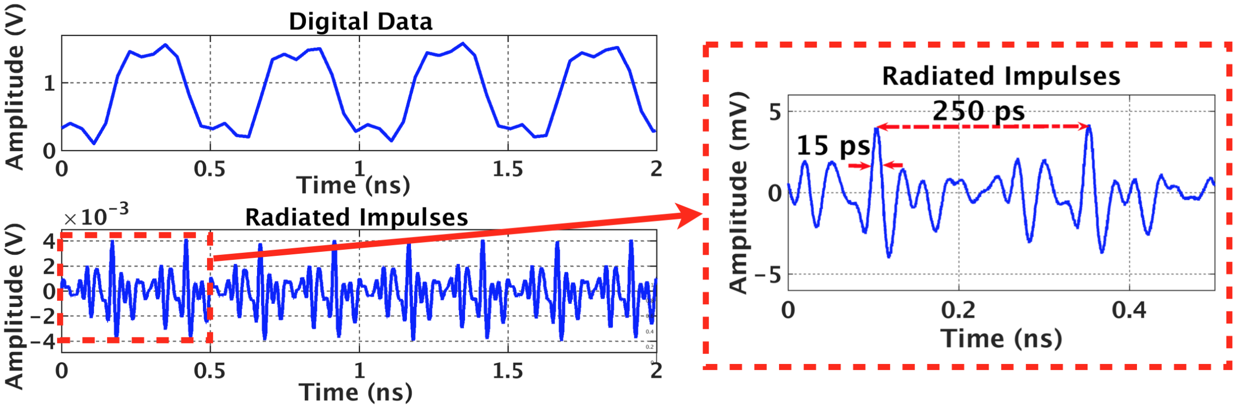

Figure 2.20: Widened impulses, as measured with a sampling oscilloscope and a custom printed circuit board-based antenna.

Furthermore, when the periodic signal is changed to a random data set, a data rate of 4 Gb/s is demonstrated while the chip radiates non-return-to-zero inverted (NRZI) on-off keying (OOK) picosecond impulses at the rising and falling edges of the digital data set (Fig. 2.21). A Keysight E8257D PSG analog signal generator provides a 4 GHz CLK signal, and a Tektronix AWG7122C arbitrary waveform generator generates the digital data set.

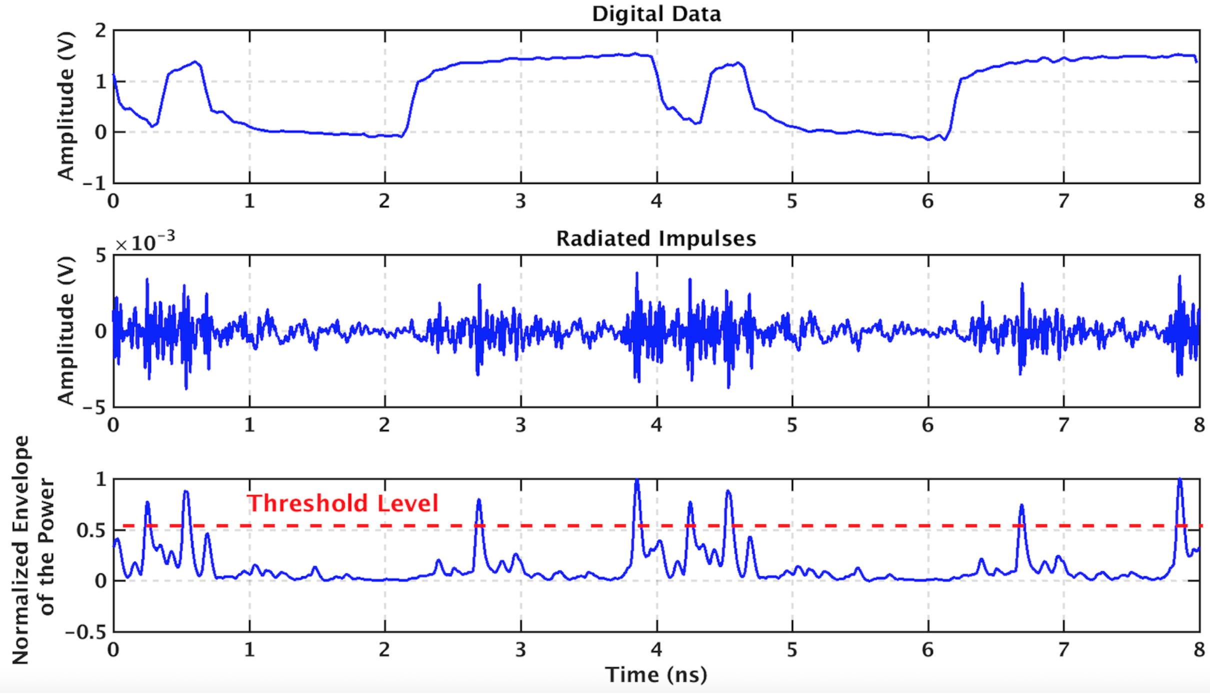

Figure 2.21: 4 Gb/s measured impulses.

Long-range wireless communication can be achieved by collimating the radiated impulses [75, 76]. This measurement setup is shown in Fig. 2.22. Two off-axis parabolic reflectors are used in front of the TX chip and custom-designed antenna to create a specular non-line-of-sight link. The radiated pulses are collimated by a 90° 4-inch diameter off-axis parabolic mirror (M1). Following M1, the collimated wave passes through 1 m to reach a plane mirror (M2), and the reflected wave from M2 passes through the return path to reach another 4-inch 90° off-axis parabolic reflector (M3). A custom-designed antenna is located at the focal length of M3 and captures picosecond pulses.

The received pulses, after passing 2 m in distance, are also shown in Fig. 2.23. The maximum distance is limited by the small directivity of the parabolic and plane mirrors at frequencies below 70 GHz. These mirrors are built for optical frequencies, and their directivity decreases in lower frequency ranges.

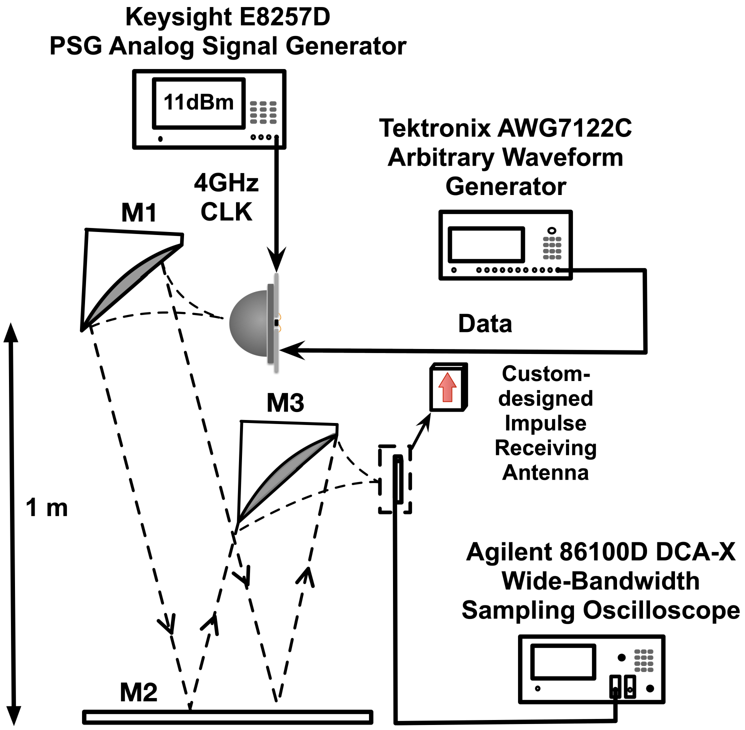

Figure 2.22: Schematic of a non-line-of-sight THz setup for 4 Gb/s impulse transmitter.

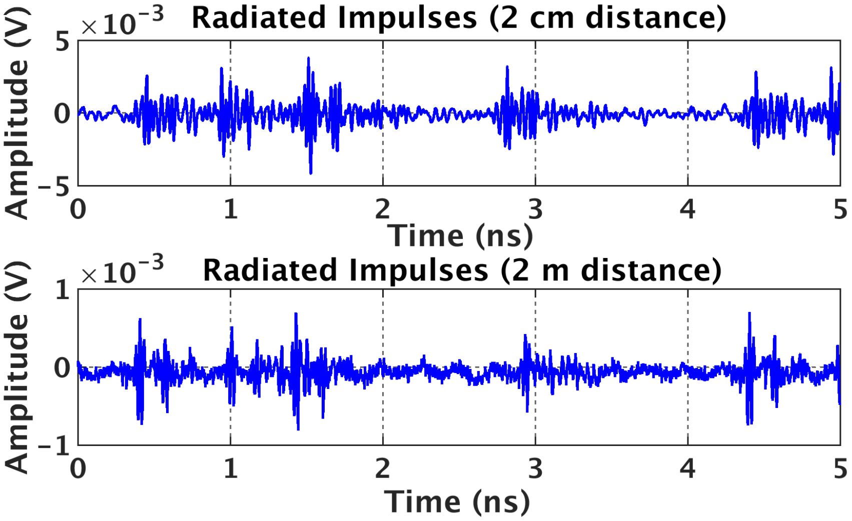

Figure 2.23: 4 Gb/s measured impulses after 2 cm and 2 m.

2.4 Chapter Summary

This chapter introduced a fully integrated ultra-broadband oscillator-free, laser-free millimeter-wave and terahertz transmitter, using a single on-chip antenna. This chip is an energy-efficient solution for developing silicon-based integrated broadband radiators with enhanced bandwidth. This design radiates 2.5 picosecond impulses, corresponding to a frequency comb with 1.052 THz bandwidth. The frequency resolution of 2 Hz is demonstrated. The spectral purity resulting from the extremely narrow spectral line-width makes this design a solution for a wide range of high-resolution sensing applications, including narrow absorption line spectroscopy, radar, imaging, and remote sensing. Moreover, the area-efficient and low-power topology allows scaling up the design for large array implementation. Additionally, an on-chip slot bow-tie antenna is integrated in this design with a maximum gain of up to +20 dBi, including the gain of the silicon lens. Furthermore, this design can transmit 4 Gb/s data with the non-return-to-zero inverted on-off keying modulation scheme. A 2 m specular non-line-of- sight communication link for long-range wireless applications is built using this transmitter, parabolic reflector antennas, and a plane mirror. This chip is fabricated in 130 nm SiGe BiCMOS process technology and, occupies a total die area of 1.26 mm^2 and consumes 206 mW of dc power.

Table 2.1 shows the comparison table with other state-of-the-art terahertz impulse-based systems in silicon.

2.5 Acknowledgment

The authors thank the National Science Foundation Career Award program for partially supporting the work.

Table 2.1: Comparison with previous impulse-based THz radiators in silicon

	This work	[65]	[66]	[67]	[63]	[77]
Architecture	**D2I**	D2I	D2I (NLQSI)	D2I (PIN diode)	VCO	Pulsed VCO
Pulse Duration (FWHM))	**2.5 ps**	1.9 ps	4 ps	1.7 ps	26 ps	60 ps
Highest Measured Frequency	**1.052 THz**	1.1 THz	197 GHz	1.1 THz	110 GHz	N/A
Communication Link	**Yes**	No	No	No	No	No
Data Rate	**4 Gb/s**	N/A	N/A	N/A	N/A	N/A
Maximum Demonstrated Range	**200 cm**	50 cm	4 cm	32 cm	N/A	20 cm
P_{DC} (mW)	**206**	105	170	45	1400	106
Die Area (mm^2)	**1.26**	0.47	1	0.48	6.16	2.85
Technology	**130-nm SiGe BiCMOS**	130-nm SiGe BiCMOS	130-nm SiGe BiCMOS	130-nm SiGe BiCMOS	130-nm SiGe BiCMOS	130-nm SiGe BiCMOS

CHAPTER 3

A Fully Integrated Ultra-broadband Comb-based Terahertz Coherent Detector in Silicon

This chapter presents a fully integrated frequency comb-based terahertz (THz) coherent detector with tunable frequency spacing, which works as an ultra-broadband detector for sensing and imaging applications, published in [80]. A nonlinear current-switching mechanism is utilized to generate a reference frequency comb. This reference comb is employed as an LO signal and downconverts the received mm-wave and THz signal to the low-frequency intermediate frequency (IF) band. This design detects arbitrary signals from 20 GHz up to 500 GHz with 2-Hz frequency resolution. A peak sensitivity of -100 dBm is measured with 1 KHz resolution bandwidth (RBW). The frequency spacing in the on-chip reference frequency comb is tunable and set to 4 GHz in this work. A chip-to-chip dual-frequency comb measurement setup is successfully implemented by using this receiver and the impulse transmitter (chapter 2). This setup is characterized in the 20-220-GHz frequency range. This chip is fabricated in 130 nm SiGe BiCMOS process technology.

3.1 Introduction

The THz frequency regime, which lies between radio frequencies at the lower end and optical frequencies at the higher end, promises enormous novel applications in spectroscopy, wireless communication, radar, high-resolution imaging, and remote sensing [1]. The need for a higher data rate in communication systems and higher resolution in sensing/imaging systems pushes the operating frequency into mm-wave/THz regimes. Due to the lack of efficient methods for generating or detecting signals in this frequency regime, an increasing interest in the exploitation of THz frequencies has been piqued in the last decade [2].

In photonics, femtosecond laser–based photoconductive antennas have been utilized for radiating and detecting a broadband frequency comb [49]. Although THz-TDS is a strong technique, it suffers from the high power consumption, high cost, and bulky measurement setups due to requirement of having a femtosecond laser source, making them impractical for some applications. Moreover, femtosecond lasers suffer from poor linewidth and phase noise. In addition, the need of having a mechanical delay line to shift the laser pulse in the sub-sampling scheme makes such systems impractical for some applications. Thus, there has been a tendency to implement THz systems in electronics.

The transistor speed in silicon-based technologies has been improving over the last several decades, making electronic-based THz systems a low-cost alternative for optical-based systems. Silicon-based technologies provide a high level of integration and low fabrication costs compared to other technologies such as III–V semiconductors. One of the main challenges in developing integrated THz systems in silicon is the generation and detection of signals beyond the $\mathrm{f}_{\mathrm{max}}$ of a transistor, which does not exceed 500 GHz [57]. The frequency $\mathrm{f}_{\mathrm{max}}$ represents the frequency at which the unilateral gain of the transistor becomes unity [53]. This is an important metric because it fundamentally defines the maximum frequency at which the device can provide power amplification.

In order to detect the frequency content of a received signal, coherent detectors are needed to downconvert the signal to intermediate frequencies (IF) using a reference signal. Continuous-wave (CW) or impulse-based systems have been used for mm-wave/THz detection beyond the $\mathrm{f}_{\mathrm{max}}$ of transistors.

The reference signal utilized for coherent detection in the CW systems can be generated by using a on-chip oscillator [81, 82]. However, having a mm-wave/THz LO signal with a sufficient power is challenging. Subharmonic mixers benefit from having a lower-frequency reference LO signal and perform mixing between the RF signal and a harmonic of the LO signal [85, 86]. Subharmonic mixers can potentially be used for coherent detection in the mm-wave/THz frequency range but this method only works in a narrowband frequency range due to the narrow tunability of local oscillator. As a result, CW techniques require multiple sources and detectors to cover the entire mm-wave/THz bands.

Conversely, impulse-based systems provide broadband spectral information because of their short durations in the time-domain [83, 84]. Broadband systems are particularly desirable since they allow detection of various gas molecules with different absorption frequencies in a broad frequency range. Since the active-time in impulse-based systems is short, the power consumption is lower as compared with CW transceivers and make such systems a promising solution for low-power and broadband applications.

Recently, an oscillator-free digital-to-impulse (D2I) architecture has been introduced recently in the silicon to detect signals in the mm-wave and THz regime [83, 84]. In D2I technique, sub-10 ps impulses are generated ans used an a LO signal by utilizing a fast nonlinear current switch. A train of picosecond impulses corresponds to an ultra-broadband frequency comb in the frequency domain. This reference comb is employed as an local oscillator (LO) signal and downconverts the received mm-wave and THz signal to the low IF band.

This chapter presents a fully integrated ultra-broadband THz frequency comb-based detector in silicon with the objective of improving ht detection BW, reducing the total power consumption, and enhancing the detection resolution in comparison with state-of-the-art wideband coherent receivers in silicon technologies. A nonlinear current-switching mechanism is utilized to generate a reference frequency comb. This design detects arbitrary signals from 20 GHz up to 500 GHz with 2-Hz frequency resolution. A peak sensitivity of -100 dBm is measured with 1 KHz RBW. A chip-to-chip dual-frequency comb measurement setup is successfully implemented by using this receiver and the impulse transmitter (chapter two). This setup is characterized in the 20-220-GHz frequency range. This chip is fabricated in 130 nm SiGe BiCMOS process technology occupies a total die area of 1.26 mm2 and consumes 206 mW of dc power.

The rest of this chapter is organized as follows. Section 3.2 begins by describing the comb-based detection principle and theoretical analysis of design. It is followed by design details and simulation results frequency comb generator and heterodyne detector. Section 3.3 presents the measurement results of the fabricated receiver, which include characterization of the receiver performance using continuous-wave sources from 20 GHz to 500 GHz. It is followed by a chip-to-chip dual-frequency comb measurement setup, which is successfully implemented by using this receiver chip and the ultra-broadband impulse transmitter (chapter two). This setup is characterized in the 20-220-GHz frequency range. Lastly, section 3.4 summarizes the chapter.

3.2 Design of A Comb-Based Coherent THz Detector

3.2.1 Comb-based Detection Principle and Proposed System

The main concept in this work is the generation of an on-chip mm-wave/THz ultra-broadband reference signal, which is tunable and can be used to coherently downconvert mm-wave/THz signals to IF signal. A train of sharp picosecond impulses that is corresponding to an ultra-braodband frequency-comb [65] can be used as a coherent detection reference signal. Due to the repetitive generation of these picosecond impulses, its frequency spectrum contains discrete frequency tones. The spacing between two adjacent tones in the frequency spectrum is determined by the repetition frequency (f_0) of impulses. Consequently, by changing the repetition frequency of impulses in the time-domain, the spacing between tones in the frequency-domain can be tuned. The BW of the frequency comb is directly related to the duration of each impulse envelope.

Non-linear transmission lines were utilized in [87, 88, 89] to generate short impulses and build samplers for broadband spectroscopy. Furthermore, optical frequency combs in the infrared band have been used in [90, 91, 92] to implement coherent spectrometers for rapid spectroscopy and sensing. Previously the nonlinearity of a bipolar junction transistor (BJT) was employed to generate a train of sharp picosecond impulses [65]. Block diagram proposed broadband coherent comb-based detector is shown in Fig. 3.1.

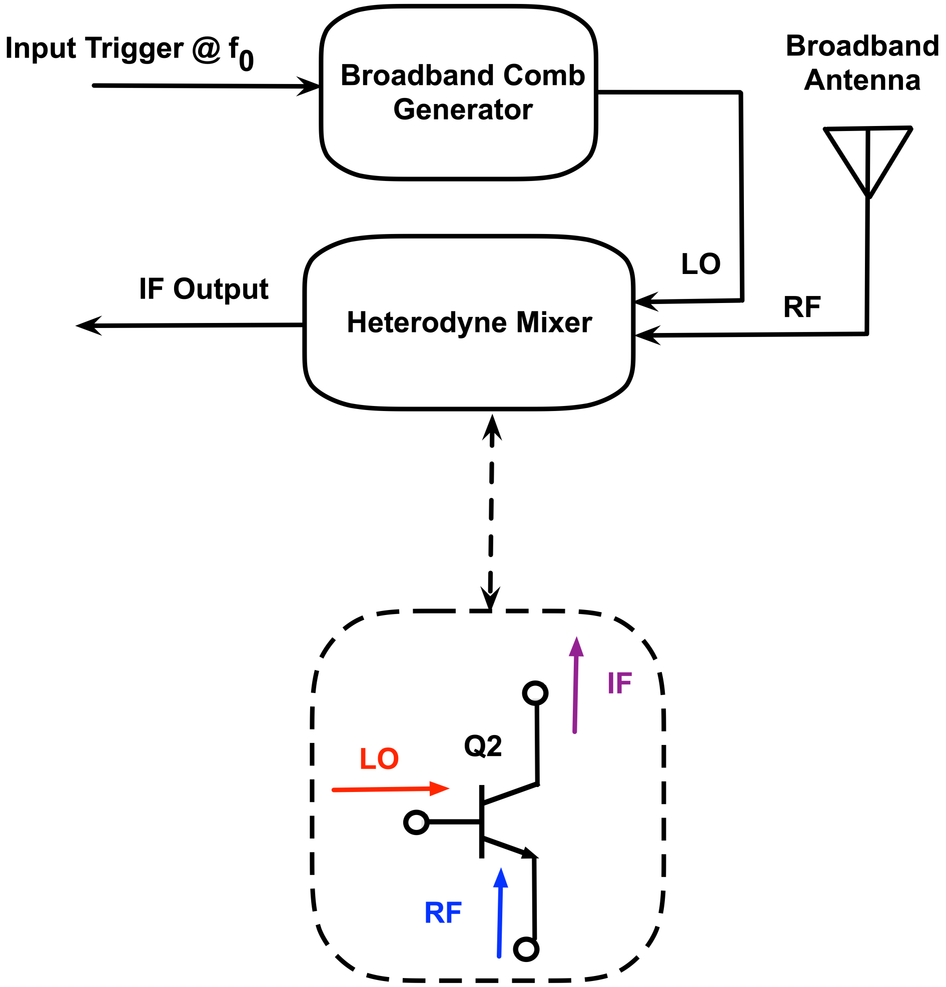

Figure 3.1: Block diagram proposed broadband coherent comb-based detector.

The heterodyne detection is performed using a BJT as a mixer in which the RF signal, which is received by the on-chip antenna, is coupled to its emitter. A reference mm-wave/THz frequency comb, which is locked to an external clock, is delivered to the base of the mixer as the LO signal. RF signal can be either a single tone or a frequency comb. In the RF single tone signal detection, the IF signal would be the result of mixing the RF signal and closest tone of the LO comb to the RF signal. If the RF signal is a frequency comb, single-shot comb detection is possible, similar to the dual-frequency-comb spectroscopy sampling systems, which a slight difference (f_{IF}) exists between the repetition rates of LO and RF combs [93, 94, 95]. A conceptual illustration of the proposed broadband coherent detector is illustrated in Fig. 3.2.

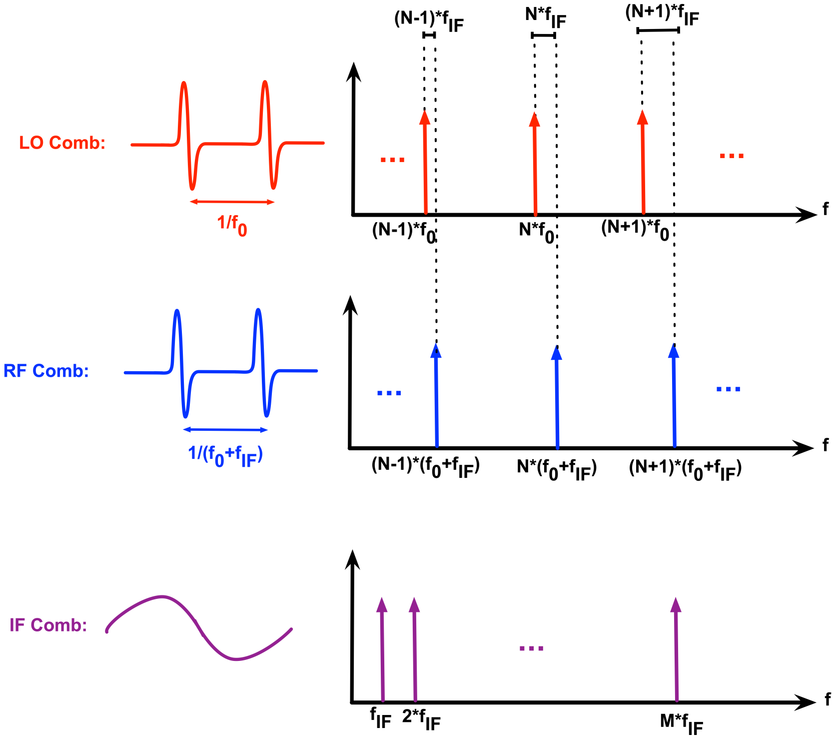

Figure 3.2: Conceptual illustration of the dual-comb detection for broadband spectroscopy and sensing.

In this case, the IF would be another frequency comb, where the difference between its tones equals to f_{IF}. Each tone in the IF comb uniquely represents the mixing result of every adjacent pair of RF and LO tones. Hence, the IF frequency comb is a sampled version of the RF comb produced by the LO comb. The IF signal should be in the IF BW to minimize the conversion loss of mixing. To miniaturize this system further, a baseband spectrum scanning circuit, such as [96], can be implemented to detect the IF frequency without using an external spectrum analyzer. The rest of this section describes the circuit realization of this ultra-broadband coherent THz detector.

3.2.2 Circuit Realization of the Coherent Comb-based THz Detector

The main concept in this work is the generation of an on-chip mm-wave/THz reference frequency comb. Thie reference comb can be delivered to an on-chip antenna and radiated in the transmit (TX) mode (Chapter 2). Moreover, this frequency comb can be used as a broadband reference signal to coherently downconvert mm-wave nad THz signals to intermediate frequency (IF) in the receive (RX) mode.

In this design, an external tunable trigger signal sets the repetition frequency of the picosecond impulse train. In the impulse-based system, spacing between two adjacent tones in the frequency-domain is determined by the repetition frequency of impulses in the toime-domain. The schematic of THz coherent detector is shown in Fig. 3.3. The mechanism in the nonlinear current-switching method is similar to the switching power amplifier, where the external trigger signal, after passing through a clock-sharpening buffer stage, becomes a square-wave signal that switches Q1.

When Q1 is on, energy is stored in the CPW transmission line. By the on-to-off switching of Q1, the stored energy in the previous step is revealed as a sharp picosecond impulse with the width of several picoseconds, which is called LO in this design. This continuous switching results in having a train of picosecond impulses, which corresponds to an ultra-broadband frequency comb in the frequency domain. The BW of this frequency comb is determined

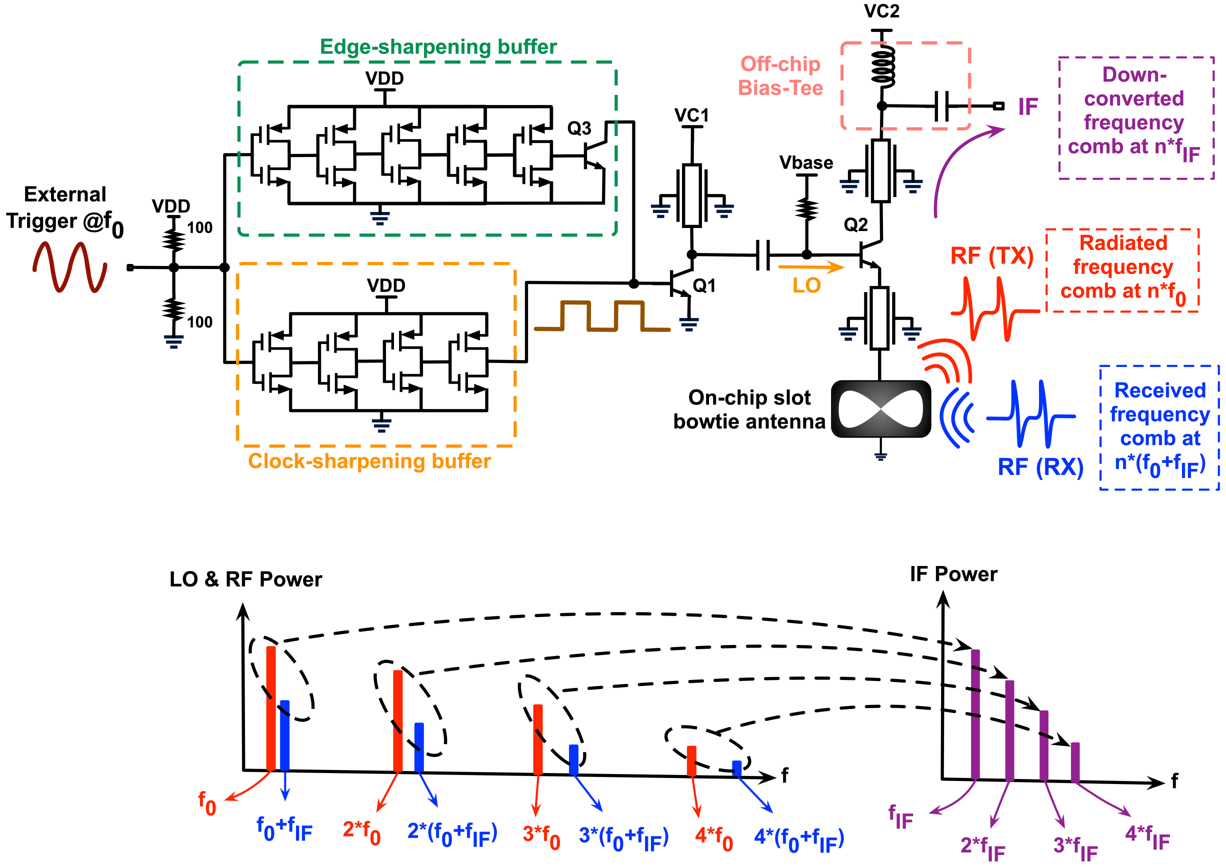

Figure 3.3: Circuit schematic of coherent comb-based THz detector.

by the pulse-with of the picosecond impulses, and the spacing between the adjacent tones is equal to f_0. The time constant at the base of Q1 plays an important role in the amplitude and the pulse-width of the picosecond impulses. As a result, an edge-sharpening buffer is employed to discharge Q1 faster.

In the TX mode, Q2 in Fig. 3.3 passes the LO Gaussian impulse train to the on-chip antenna as a driver. The on-chip antenna changes the Gaussian impulse train to a monocycle pulse train with no DC and radiates it. Furthermore, Q2 in the RX mode acts as a heterodyne mixer and mixes the LO signal at the base of Q2 and the RF signal received by the antenna at the emitter.

To explain the concept of this design, we need to drive the equations of the large-signal I-V response of Q2 in Fig. 1, which can be written as [97]:

$$I(V) = I_s(e^{\alpha V} - 1), \tag{3.1}$$

where I is the current of Q2, I_s is the reverse saturation current, and V is the voltage across the base and emitter of Q2, including a large signal voltage (V_{LO}) and a small signal voltage (v_{RF}). The constant $\alpha = q/nkT$, where q is the charge of an electron, k is Boltzmann's constant, T is the temperature in Kelvin, and n is the transistor ideality factor. By assuming that v_{RF} is small, we can write the Taylor series expansion of the equation (1) about V_{LO}:

$$i(v_{RF}) = I(V_{LO}) + v_{RF}(dI/dV)\Big|_{V_{LO}} + 0.5v_{RF}^2(d^2I/dV^2)\Big|_{V_{LO}}, \tag{3.2}$$

The first term in equation (2) is a function of only LO signal, which is what the antenna radiates in the TX mode. The second term is a function of the LO and RF signals, which gives us the mixing effect and is going to be used in the RX mode of this design. The effect of the third term is negligible compared with the first two terms.

dI/dV in equation (2) can be written as:

$$g(t) = dI/dV\Big|_{V_{LO}} = \alpha I_s e^{\alpha v_{LO} cos(\omega_{LO} t)}, \tag{3.3}$$

Given that $g(t)$ is a function of the LO signal and the LO signal is periodic, $g(t)$ can be expressed as a Fourier cosine series in terms of the harmonics of ω_{LO}:

$$g(t) = g_0 + \sum_{n=1}^{\infty} 2g_n cos(n\omega_{LO}t), \tag{3.4}$$

where g_n is the Fourier coefficient. Therefore, the second term in equation (2) can be written as:

$$i(t) = g(t).v_{RF} = (g_0 + \sum_{n=1}^{\infty} 2g_n cos(n\omega_{LO}t))(\sum_{m=1}^{\infty} v_{RF_m} cos(m\omega_{RF}t)), \tag{3.5}$$

where LO is a frequency comb and RF can be either a single tone or a frequency comb. In the RF single tone signal detection, the IF signal would be the result of mixing the RF signal and closest tone of the LO comb to the RF signal. If the RF signal is a frequency comb, single-shot comb detection is possible, similar to the dual-heterodyne-mixing method in optics, which a slight difference (f_{IF}) exists between the repetition rates of LO and RF combs. In this case, the IF would be another frequency comb, where the difference between its tones equals to f_{IF}.

Each tone in the IF comb uniquely represents the mixing result of every adjacent pair of RF and LO tones. Hence, the IF frequency comb is a sampled version of the RF comb produced by the LO comb. The IF signal should be in the IF BW to minimize the conversion loss of mixing.

3.3 Measurement Setups and Results

This section describes the measurement setups and results in the characterization of the performance of this chip as a coherent THz detector. In the first step, receiver performance is characterized in the frequency-domain by utilizing continuous-wave signal sources from 20

GHz to 500 GHz. In the next step, a chip-to-chip dual-frequency comb measurement setup is successfully implemented by using this receiver chip and the ultra-broadband impulse transmitter (chapter two). This setup is characterized in the 20-220-GHz frequency range.

This chip is fabricated in 130 nm SiGe BiCMOS process technology and occupies a total die area of 1.26 mm^2. Fig. 3.4 shows the die photograph of the chip. The total dc power consumption is 206 mW with a 1.2 V power supply. A hemispherical, high-resistivity silicon lens is attached under the chip to eliminate the substrate modes and increase the detection efficiency and BW.

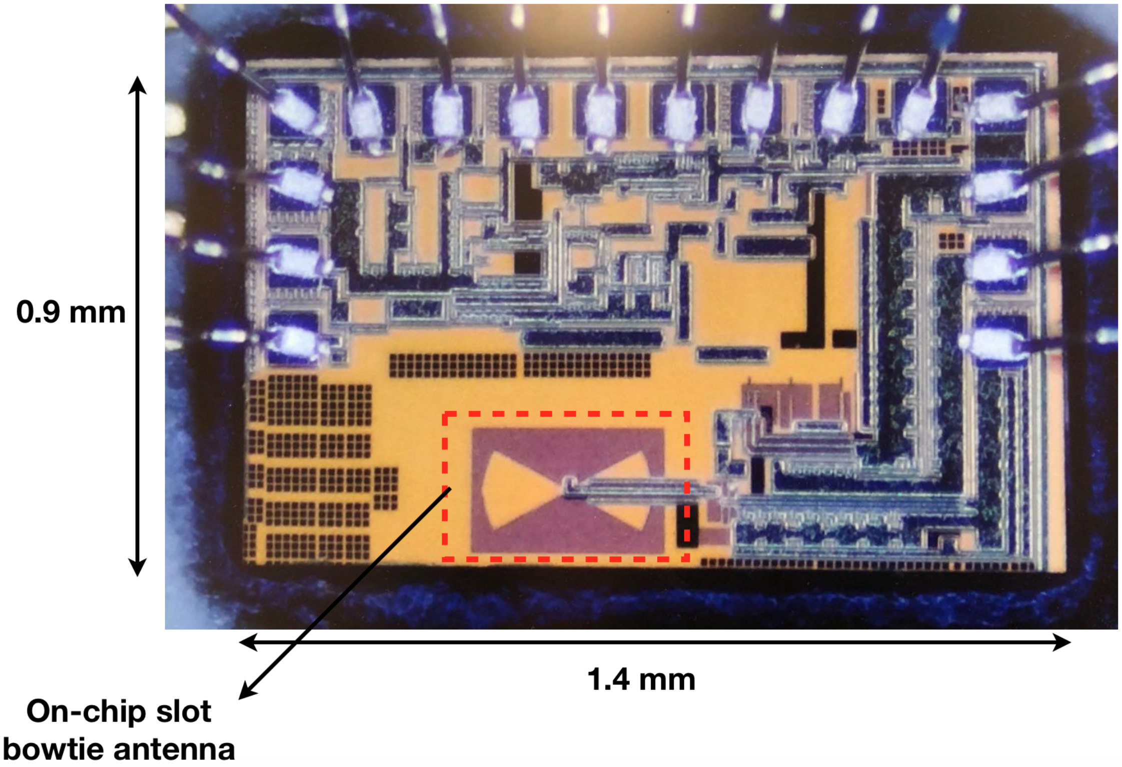

Figure 3.4: Micrograph of coherent THz detector chip.

3.3.1 Frequency-domain Measurement

To characterize the performance of this detector, multiple CW signal sources from 20 GHz to 500 GHz are deployed to measure the power level of downconverted tones at IF. In the second test, another silicon-based chip ([70]) is used to radiate a frequency comb with a different spacing from the receiver to demonstrate the chip-to-chip dual-frequency comb measurement setup. This setup is characterized in the 20-220-GHz frequency range.

At the first step of characterization of this detector, we need to measure the IF BW and noise floor of this receiver. The IF BW is measured by changing the frequency of the RF signal (generated by the Keysight E4428C signal generator and radiated by a horn antenna) and measuring the IF power. Fig. 3.5 shows the receiver IF characterization measurement setup.

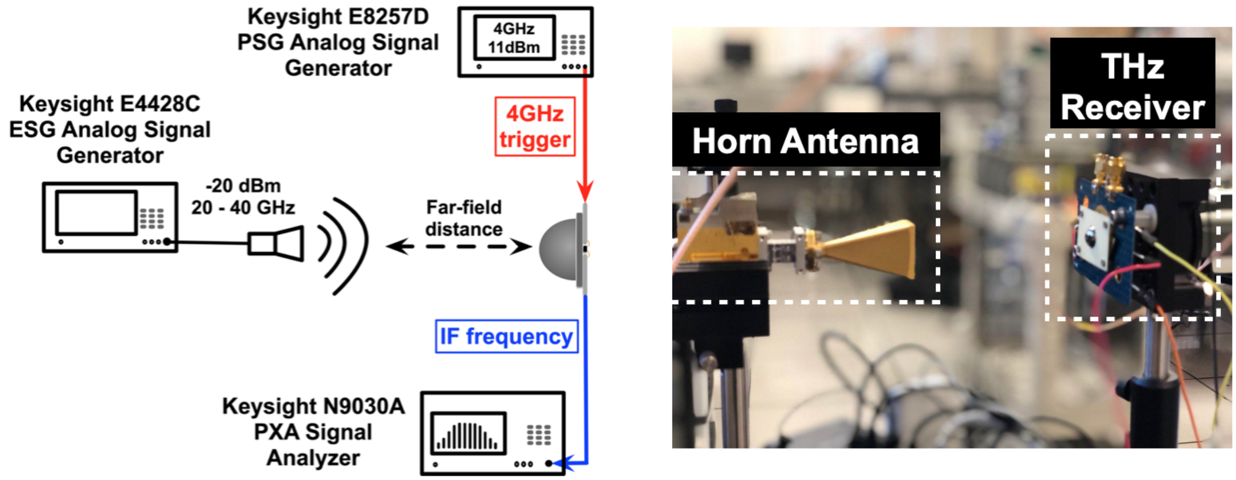

Figure 3.5: THz detector IF characterization measurement setup.

The power of the RF signal is kept constant and equal to -20 dBm in this measurement, whereas the frequency is increased from 20 GHz to 40 GHz. In this measurement, the LO frequency comb spacing is 4 GHz, and the RF signal is mixed with the fifth harmonic (20 GHz) in the LO comb, and the IF power can be measured up to 20 GHz.

The IF power and noise floor with a 1 Hz resolution BW (RBW) are plotted in Fig. 3.6. In this measurement, the IF 3 dB BW is measured around 100 MHz, and the noise floor is less than -140 dBm in the entire BW. Thermal and flicker noises from the mixer, noise of the spectrum analyzer, and the added noise to the LO signal due to passing through several stages, are the factors that determine the IF noise floor. Moreover, the measured IF tone is also shown in Fig. 3.6. The 10-dB-below-peak spectral line-width of 2 Hz with 1 Hz RBW is measured.

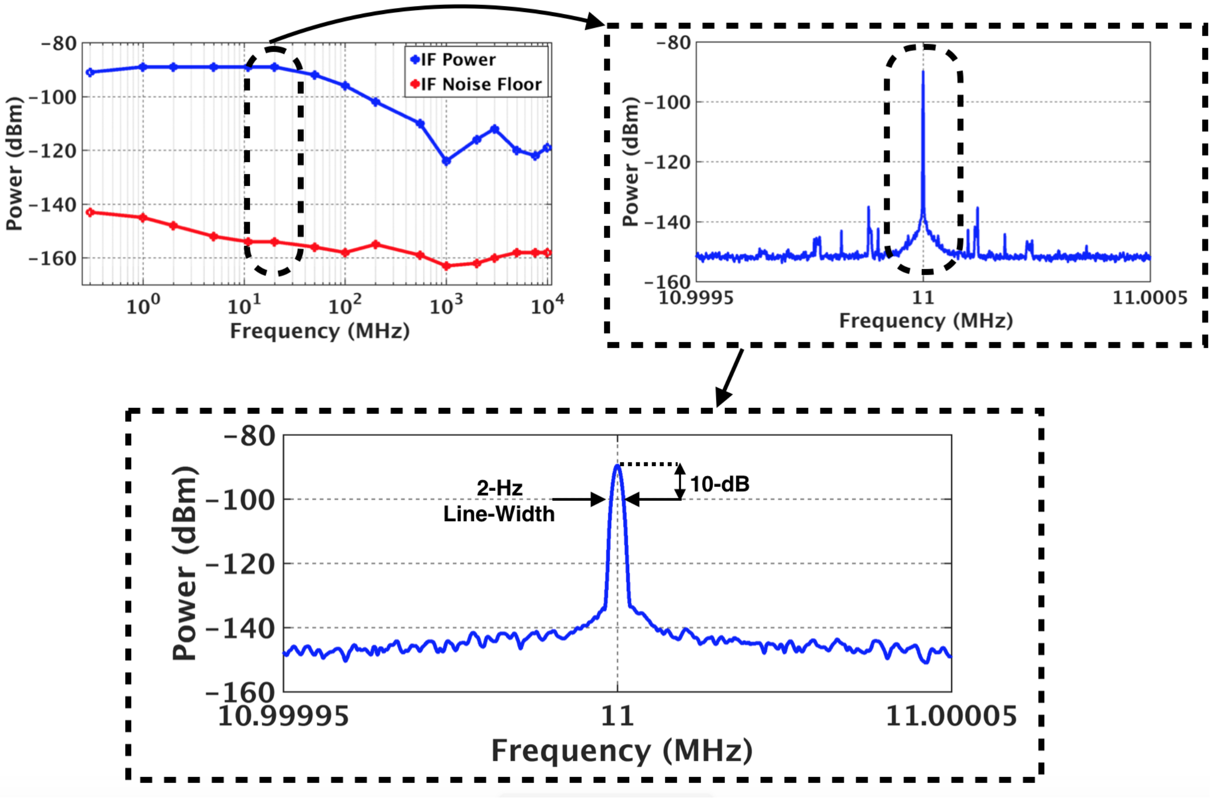

Figure 3.6: THz detector IF characterization measurement result: IF BW, IF noise floor, IF tone, and a spectral line-width of 2 Hz.

In the next step, the sensitivity of the THz detector is measured. For measuring the response of the RX to various frequencies, CW signal sources in different bands and horn antennas are used. These measurement setup configurations for broadband RX chip characterization are shown in Fig. 3.7.

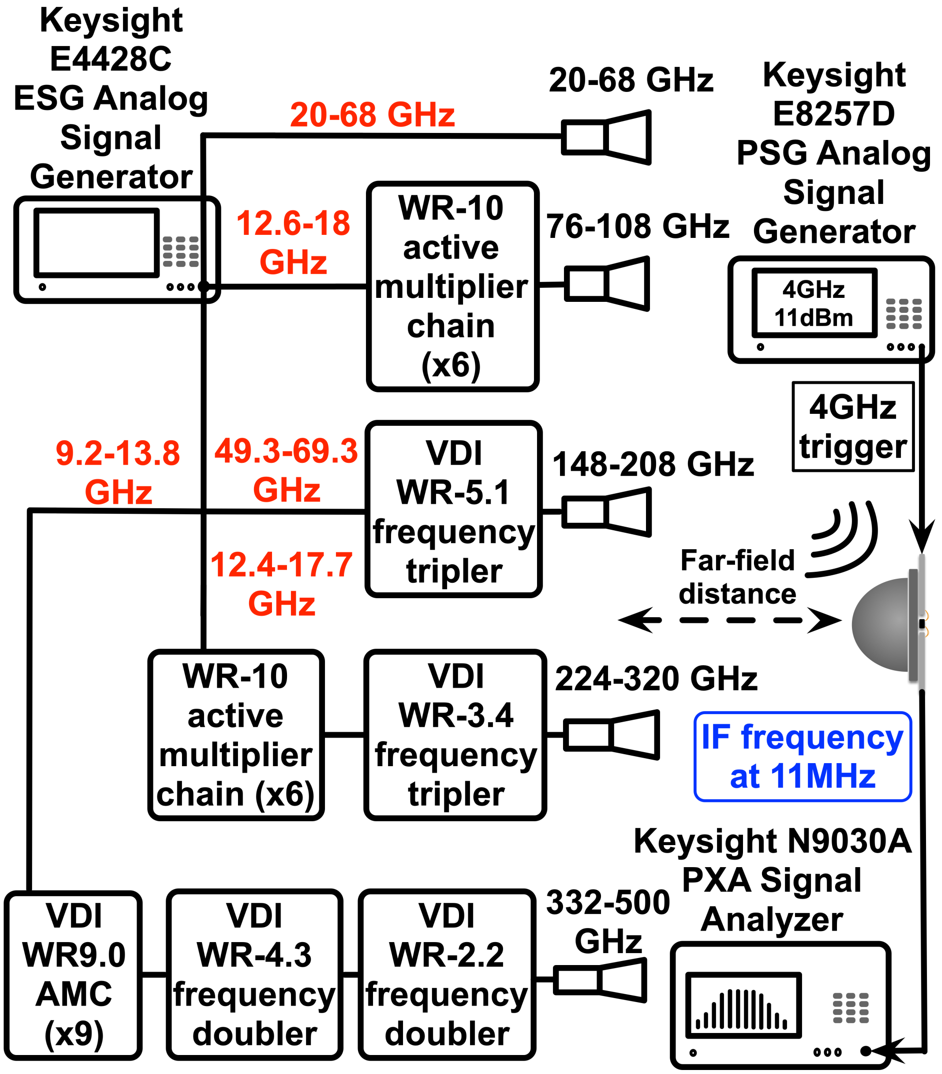

Figure 3.7: Measurement setup configurations for characterizing the THz detector performance over multiple frequency bands.

A Keysight E4428C signal generator is used to directly generate CW sinusoidal signals for the 20–70 GHz range. The generated waves are radiated with various horn antennas to cover this band. For the 20–36 GHz band, an A-Info LB-180400 horn antenna with a +15 dBi gain is utilized. The distance between the horn antenna and the chip is set to 27 cm to ensure a far-field regime. This distance is calculated based on the largest dimension of this horn antenna and on the maximum operation frequency, which is 40 GHz in this band. For 40–52 GHz, a QuinStar QWH U-band horn antenna with a +22.5-dBi gain is used, and the distance is 92 cm. Finally, for the 56–68 GHz band, the distance is 68 cm, and an OML MR15RH with +24-dBi is employed.

The 75–110 GHz band is covered using a Millitech WR-10 active multiplier chain (AMC) that generates signals and an OML M10RH horn antenna with a +24-dBi gain that radiates them. This multiplier multiplies its input signal by a factor of 6. The distance between the RX chip and the horn antenna is 50 cm.

Signals in the next frequency band, 140–210 GHz, are generated using a VDI WR-5.1 passive frequency tripler, which has an input-to-output efficiency between 2% and 5%. A standard horn antenna with a +24 dBi gain radiates the generated signals, and its distance to the RX chip is 30 cm.

The next frequency band, 220–320 GHz, is generated by cascading a Millitech WR-10 AMC and a VDI WR-3.4 passive frequency tripler. This cascaded setup multiples its input signal by a factor of 18, and the far-field region in this band is 30 cm. A standard horn antenna with a +24 dBi gain is used in this frequency band.

Finally, another cascaded setup is employed to cover the 330–500 GHz frequency band, in which a VDI WR9.0 AMC, followed by two VDI frequency doublers, WR-4.3 and WR-2.2, are utilized. The distance between the standard horn antenna with a +24 dBi gain and the RX chip is 5 cm in this frequency band.

RF signals from CW signal sources are down converted to the IF signals by using THz coherent detector chip as a receiver. The response of the chip is recorded by measuring the IF power.

The sensitivity of the RX is calculated by fixing the IF frequency at 11 MHz to eliminate the IF BW effect and obtain consistency in the measured signal. The received power at the RX ($P_{R,ant}$) is estimated using the Friis transmission equation (which includes the on-chip antenna gain). For sensitivity calculation, the IF signal-to-noise ratio can be calculated at 11 MHz for various RF signals. The sensitivity in dBm can be calculated as follows:

$$Sensitivity = P_{R,ant} - (P_{IF} - RX\ output\ noise\ floor) + 10\log(\frac{1KHz}{RBW}), \tag{3.6}$$

For this calculation, the RX output noise floor at 11 MHz is -154 dBm, and the distance between the horn antennas and the chip is determined to ensure that the far-field region has been reached. Fig. 3.8 shows the sensitivity of the RX for the frequency range between 20 and 500 GHz, and the RBW is 1 KHz.

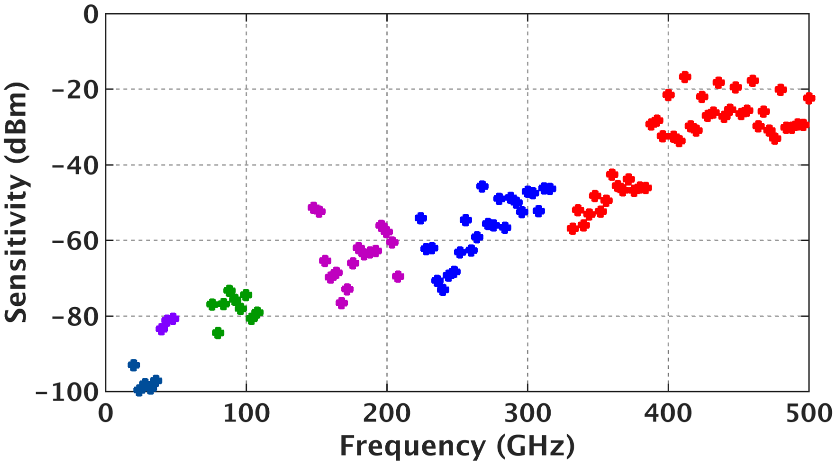

Figure 3.8: THz detector sensitivity plot from 20 GHz up to 500 GHz.

3.3.2 Chip-to-chip Dual-frequency Comb Measurement

Frequency comb detection is one of the applications of this design, given the existence of a broadband frequency comb as an LO signal. In this measurement, this chip is used as a TX and RX and can downconvert a mm-wave and THz frequency comb (which is called RF) to low RF frequencies (called IF). This downconversion is done by setting a slight difference (f_{IF}) between the repetition frequencies of LO and RF frequency combs, which creates a unique difference between every adjacent pair of RF and LO tones. The IF signal is another frequency comb with equally spaced tones equal to (f_{IF}), which is a sampled version of the RF signal, produced by the LO. Each tone in the IF uniquely represents one of the tones in the RF frequency comb, which can be utilized in spectroscopy systems.

A dual-frequency comb test setup is shown in Fig. 3.9. The distance between the TX chip and the RX chip is 2 cm. The comb spacing of the LO and RF signals are set to 4 GHz and 4 GHz + 300 KHz, resulting in an IF frequency comb with a 300 KHz spacing.

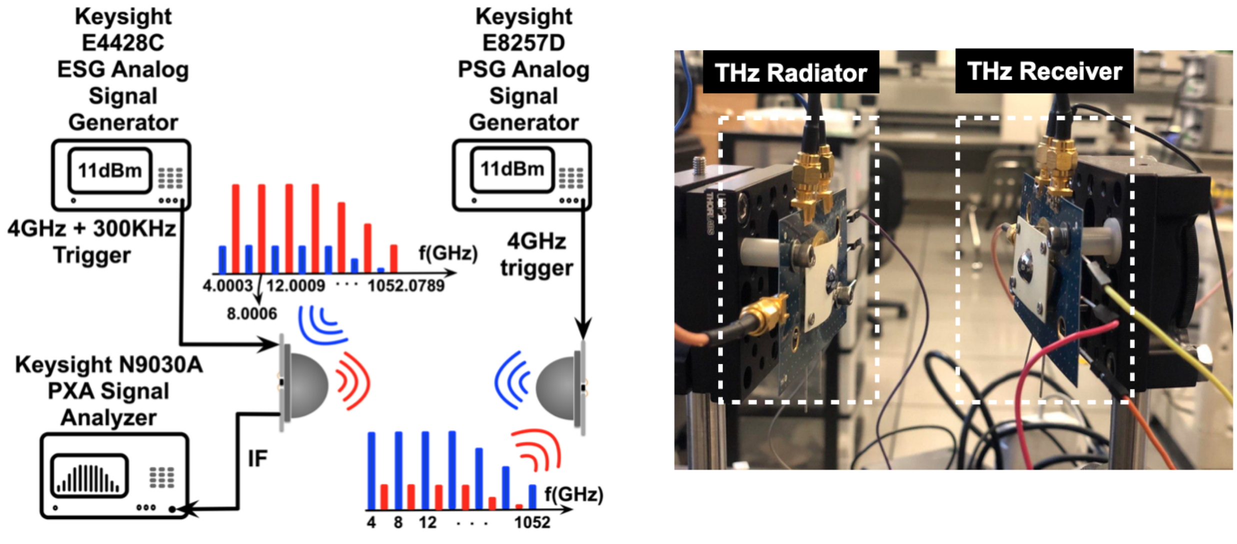

Figure 3.9: Chip-to-chip dual-frequency comb measurement setup.

In this measurement, 50 IF tones are measured, corresponding to 200 GHz BW in the RF frequency comb (Fig. 3.10). An off-chip bias-tee is used for separating the DC and IF frequencies to ensure that Q2 in Fig. 3.3 is always in the active region while the IF frequency can be measured.

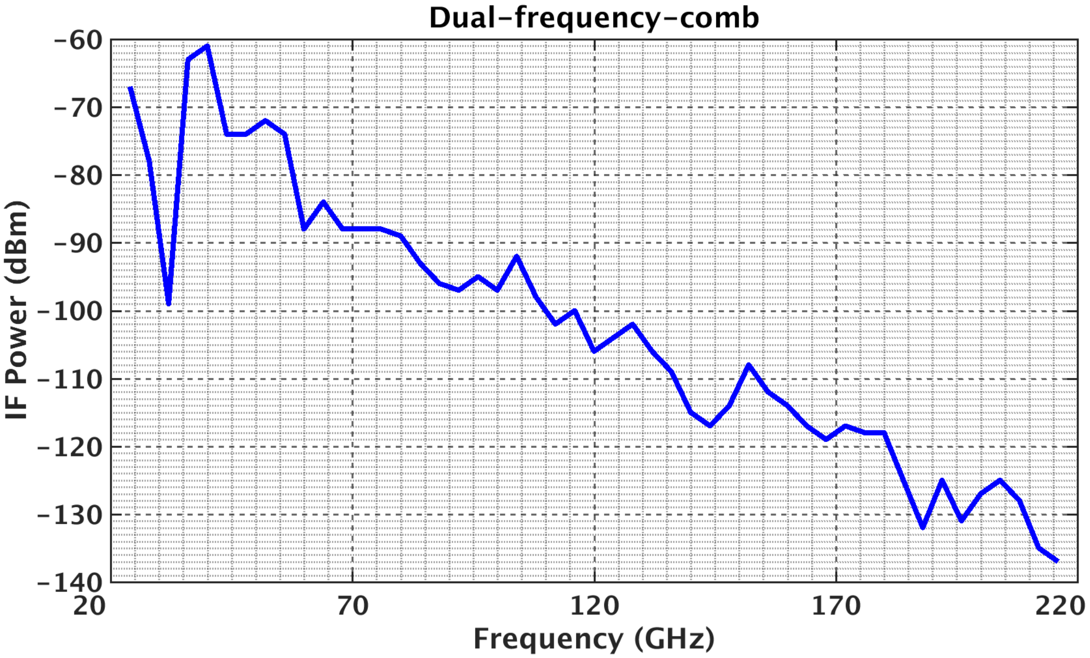

Figure 3.10: Chip-to-chip dual-frequency comb measurement result.

3.4 Chapter Summary

This chapter introduced a fully integrated ultra-broadband oscillator-free laser-free, millimeter-wave and terahertz coherent detector, using a single on-chip antenna. This chip is an energy-efficient solution for developing integrated broadband detectors with enhanced bandwidth in silicon-based technology. This coherent detector can detect arbitrary signals up to 500 GHz with a peak sensitivity of -100 dBm with a 1 KHz resolution bandwidth. The frequency resolution of 2 Hz is demonstrated. Among the recently developed coherent receivers, the proposed detector has the widest bandwidth. The spectral purity resulting from the extremely narrow spectral line-width makes this design a solution for a wide range of high-resolution sensing applications, including narrow absorption line spectroscopy, radar, imaging, and remote sensing. A chip-to-chip dual-frequency comb is also successfully measured and characterized in the 20–220 GHz frequency range by utilizing this chip as a THz transmitter (chapter 2) and receiver. This area-efficient and low-power topology allows scaling up the design for large array implementation. To have a compact integrated THz radiation and detection system, an on-chip slot bow-tie antenna is employed in this design with a maximum gain of up to +20 dBi, including the gain of the silicon lens. This chip is fabricated in 130 nm SiGe BiCMOS process technology, occupies a total die area of 1.26 mm^2 and consumes 206 mW of dc power.

Table 3.1 shows the comparison table with other state-of-the-art terahertz coherent detectors in silicon.

3.5 Acknowledgment

The authors thank the National Science Foundation Career Award program for partially supporting the work.

Table 3.1: Comparison with state-of-the-art coherent terahertz detectors in silicon

	This work	[69]	[98]	[99]	[100]	[101]	[102]
Frequency (GHz)	**20-500**	50-280	40-330	220-330	115-325	315-328	240
Frequency Resolution (Hz) [1]	**2**	2	10 M	380 K	N/A	N/A	>2 M [2]
Minimum Sensitivity (dBm) [3]	**-100**	-73	-64	-129	-115	-124	-102
LO Frequency (GHz)	**4**	3-5	N/A	45-46.67	28.75-81.25	17.7	0.075
RX Tuning Range (GHz)	**480**	230	390	110	210	13	2.4
P_{DC} (mW)	**206**	34	212	1700	36	56	980
Die Area (mm^2)	**1.26**	0.56	4.94	6	0.9	1.3	2.8
Technology	**130-nm SiGe BiCMOS**	65-nm CMOS	130-nm SiGe BiCMOS	45-nm CMOS SOI	65-nm CMOS	65-nm CMOS	65-nm CMOS

[1] LO tuning resolution which is limited to linewidth of the tones.

[2] Estimated from measured spectrum plots

[3] Calculated for SNR = 1 with RBW = 1 kHz.

CHAPTER 4

Terahertz Channel Characterization Using a Silicon-based Picosecond Impulse Source

This chapter presents a THz channel characterization using a picosecond impulse radiator in silicon, published in [75, 76]. In this work, a long-path THz communication channel is characterized in the frequency range of 0.32–1.1 THz using a customized, silicon-based THz impulse radiator chip. The chip generates and radiates picosecond impulses with an on-chip antenna at a repetition rate of 8 GHz, resulting in a broadband 0.1–1.1 THz frequency comb. The chip is fabricated in 130-nm SiGe BiCMOS process. A specular link is created using an impulse radiator, parabolic reflector antennas, a plane mirror, and a downconverter mixer. The THz channel is characterized up to a distance of 110 m. The measurement results demonstrate channel path loss, atmospheric absorption, and low-loss frequency windows suitable for wireless links in THz range. To the best of our knowledge, this is the first time a customized low-power silicon-based radiator has been used as the channel characterization source at THz frequencies. The results correspond well with those obtained by the HITRAN [103].

4.1 Introduction

THz frequencies, which lie between optical and radio frequencies, have attracted researchers due to their wide range of applications. The non-ionizing nature of these frequencies renders them effective in security and medical imaging [104]. In addition, high operating frequencies and wide bandwidth enhance the spatial and lateral resolutions for radar applications [40, 105], and the presence of distinct rotational transitions of numerous molecules in the THz spectrum makes these frequencies a viable solution for gas spectroscopy [39, 38]. Furthermore, THz frequencies promise larger bandwidths for wireless links [106]. Hundreds of gigahertz of free unlicensed spectrum available in the THz regime make them an ideal candidate to realize high-speed wireless communication links. It is evident that the THz band has the potential to realize terabit-per-second communication in the future [107, 108, 109].

Utilizing THz band for long-distance communication and remote sensing have been of interest. In the last decade, remarkable improvements have been made in the specifications of accessible THz technologies in photonics and electronics. The birth of 5G systems and the definition of the 6G standard for communication and sensing are evidence of the increasing interest in the exploitation of THz frequencies for ultra-broadband wireless communication. At the same time, pushing the operating frequencies beyond 300 GHz has been among the popular research topics in academia. For communication applications particularly, if the current trend continues, the data rates of WLANs and cellular links are expected to surpass 1 Tbps and 100 Gbps, respectively, by the end of this decade [9]. According to Shannon-Hartley's ideal communication theorem, such data rates require a large bandwidth, which is feasible to allocate only in frequencies above the mm-wave band. However, researchers have remained pessimistic regarding the feasibility of THz propagation over relatively long distances due to high atmospheric absorption loss. This issue is even more critical for the case of the silicon-based THz radiators [110], in which the amount of radiated power is 10s of dB below that of the optical-based THz systems.

Most studies in the THz domain have been limited to short-distance setups in a lab environment. Studies of long-distance THz propagation have mostly utilized laser-based THz sources. However, laser-based THz systems suffer from high power consumption, high cost, and bulky measurement setups. Although such studies have offered valuable analyses of the THz band, they do not promise a practical solution for the long-distance THz propagation problem. Therefore,, it is essential to investigate the possibility of a compact and low cost solution to implement a long-distance link, not only for communication purposes but also for sensing and radar applications.

To exploit THz frequencies for the aforementioned applications, it is imperative to study the atmospheric channel response of these frequencies and investigate the possibility of THz propagation over relatively long paths [111]. The presence of the water vapor absorption lines results in a significant attenuation of the THz waves in the atmosphere and poses the main challenge to realizing long-distance wireless links. In far-field, the channel loss can be expressed based on the Friis transmission equation:

$$P_{r|dB} = P_{t|dB} + G_{t|dB} + G_{r|dB} + 20\log(\frac{\lambda}{4\pi d}) - 4.34\alpha_f d, \tag{4.1}$$

where P_r is the received power and P_t is the transmitted power. G_r and G_t are the antenna gain for the receiver (RX) and transmitter (TX), respectively; α_f is the frequency-dependent atmospheric attenuation factor; λ is the signal wavelength; and d is the distance between the receiver and the transmitter. As is evident, the amount of path loss is directly proportional to the frequency of the propagating wave. As a result, at the THz band, the amount of path loss is significantly larger compared to lower frequency bands, thereby limiting the propagation distance. The other challenge arises from atmospheric absorption lines. A precise knowledge of the locations and widths of these absorption lines is essential for long-distance applications. Spectral shaping techniques can be employed to effectively use the windows in between the absorption peaks to mitigate this problem. These challenges become even more critical in the case of silicon-based THz radiators, in which the radiated power is significantly lower than optical THz generators.

There are a number of challenges that need to be addressed for designing high-speed links in the THz regime. The primary challenge is to generate and detect THz waves using compact, scalable, and cost-effective implementations. Optical THz generation techniques are mainly based on the emission of a femtosecond laser to a photoconductive antenna [50, 51], resulting in expensive and bulky setups and therefore limiting the practicality of such approaches. Quantum cascade lasers [112] that generate THz radiation through inter-sub-band transitions are expensive and highly sensitive to optical alignment.

THz transmitters and receivers fabricated using silicon-based processes represent a practical solution, because such processes enable low-cost, integrated, and efficient implementation of THz-based systems. However, despite recent advances in the field, THz power generation in silicon is still limited. The switching transients and low f_{max} of the transistors pose the main challenge for on-chip THz power generation. Conventional electronic approaches use harmonic-based continuous wave radiators in silicon technologies to radiate power in the lower THz band [113]. These approaches have narrow bandwidths and are therefore unsuitable for broadband applications. For the purpose of this study, a broadband THz radiator is preferred. THz pulse radiators and receivers can cover 100s of GHz band. [67, 69, 80, 83, 70], thereby incorporating spectral information over a broad band. This feature is useful and critical for specific applications such as hyperspectral imaging, broadband sensing, and high-resolution radars [114].

Prior studies of THz wireless channel characterization have been attempted with varying temperatures, humidity, and elevations to refine the existing theoretical models and predict atmospheric propagation in this regime. These studies have used predominantly optical setups implementing Fourier transform spectroscopy (FTS) [115, 116, 117] or THz time domain spectroscopy (THz-TDS) [118]. For instance, in [115], multipass FTS was used to propagate THz radiation between 0.15 and 1.1 THz over distances up to 469 m. In [118], a THz-TDS system with optoelectronic antennas was used to characterize water-vapor absorption from 0.2 to 2 THz over a distance of 6.2 m. All these techniques suffer from the aforementioned limitations imposed by the use of an optical-laser-based setup.

Due to the limited bandwidth and radiated power of conventional electronic THz sources, and due to high absorption in the THz band, low-cost electronic sources were not considered as a viable option for relatively large distances. However, [75, 76] showed that transmitting and receiving broadband THz pulses over 100s of meter is feasible. This paper describes an all-electronic method that uses a low-power silicon integrated radiator based on PIN diode reverse recovery [67] to examine the channel response in the 0.32–1.1 THz frequency range for distances between 10 and 110 m. The goals of this work are (1) to demonstrate wireless transmission and reception in THz frequencies over long distances using a low-power custom silicon-based radiator, (2) to identify the frequency windows suitable for THz propagation, and (3) to demonstrate channel characteristics (e.g., atmospheric absorption coefficient) over a broad range of frequencies using a compact, all-electronic, tunable silicon source. The experimental setup of this work can also be used to investigate long-distance high-speed wireless communication, remote sensing, and radar applications.

The rest of this chapter is organized as follows. In section 4.2, the long-path experimental setup for channel characterization is elaborated. Section 4.3 presents the measurement results of this experiment. Section 4.4 offers insights into the measurement results and proposes a method of extracting the absorption coefficient from the measured data. Lastly, section 4.5 summarizes the chapter.

4.2 Long-Distance Experimental Setup

It is well-known that THz atmospheric transmission is a function of relative humidity [119]. The channel characterization measurements were performed indoors with an average humidity of 55%. The schematic of the measurement setup for distances between 10 and 110 m is shown in Fig. 4.1.

In order to generate a wideband frequency comb, a THz pulse radiator chip based on reverse recovery of a PIN diode is used [67]. The chip radiates a frequency comb from 10s of GHz to 1 THz using an on-chip slot bow-tie antenna. The spacing between the THz tones is

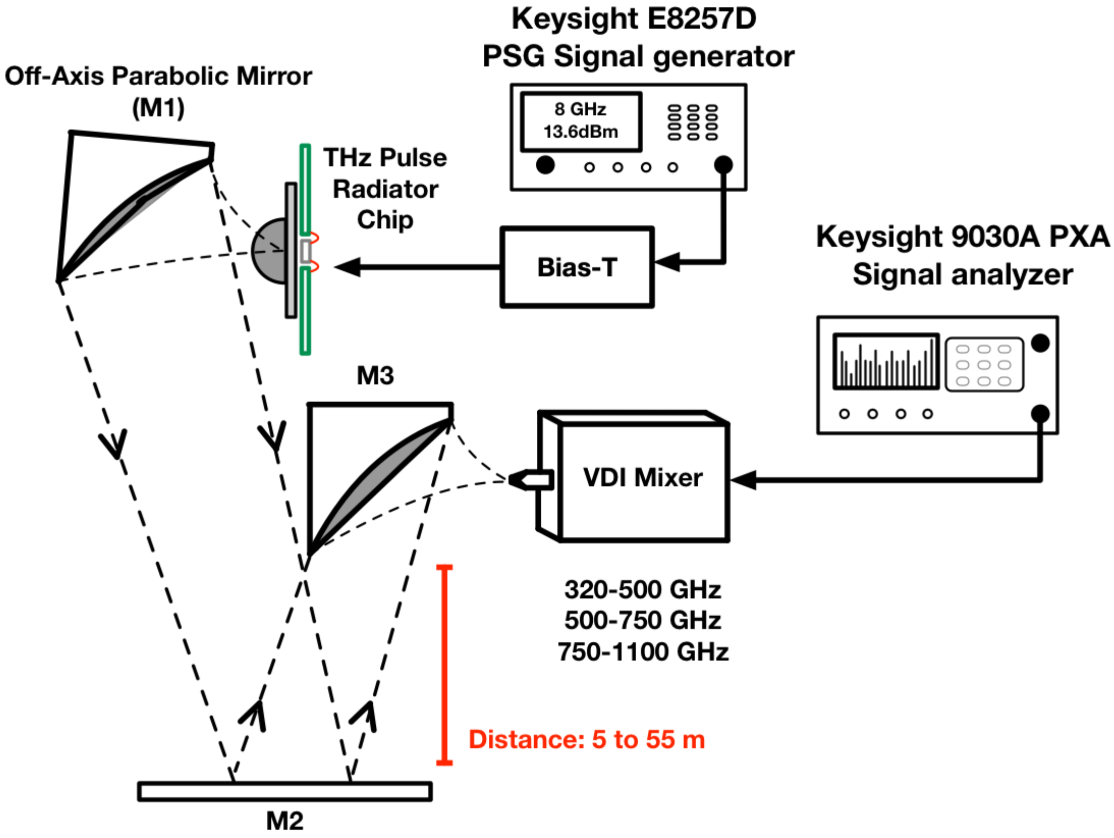

Figure 4.1: Block diagram of the long-distance THz impulse measurement setup.

set by the repetition rate of the external trigger, which is programmable from 100s of MHz up to 12 GHz. This tunability feature enables sweeping of the frequency of the THz tones radiated by the chip, thereby enabling measurements with a high frequency resolution. The spectral purity of the radiated THz tones is of the first order, dependent on the phase noise of the external source. Consequently, the 10-dB linewidth of the radiated tones is less than 2 Hz, which can be attributed to the low phase of the input trigger source. This makes the THz pulse radiator chip useful for high-resolution spectroscopy as well as remote sensing applications. The chip is implemented in 130-nm SiGe BiCMOS technology and consumes a total 45 mW of DC power. In this experimental setup, the chip is fed by an 8-GHz trigger signal from a Keysight E8257D PSG Signal Generator.

Two off-axis parabolic (OAP) mirrors were utilized to increase the directivity of TX and RX antennas for long-distance propagation. The parabolic mirrors are utilized as directive reflector antennas for THz waves enabling long-distance propagation. The directivity of the OAP mirror is determined by the size of the mirror, Therefore, 4-inch OAP mirrors with aluminium coating were used to collimate the beams. Furthermore, the metal thickness of the mirror coating was larger than the skin depth at THz frequencies, promising low-loss reflection.

Following M1, the collimated THz electromagnetic waves pass through various distances between 5 and 55 m to reach a plane mirror (M2). The reflected waves from M2 pass through the return path to reach another 4-inch OAP reflector (M3). A Keysight N9030A PXA Signal Analyzer and VDI SAX mixers are used in conjunction with WR2.2, WR1.5, and WR1.0 horn antennas to cover the 320–500, 500–750, and 750–1100-GHz frequency bands, respectively. Moreover, by using a broadband pulse radiator and by changing the position of M2, the channel characteristics were evaluated for different frequencies as well as different distances. Fig. 4.2 illustrates the measurement setup used in this study.

One of the main challenges is the precise collimation of the invisible THz waves. For this purpose, the THz pulse radiator chip is replaced with a lens that transforms the red laser beam (located at back of the printed circuit board) into a point source. After collimating the visible light by adjusting the mirrors, the quality of collimation is checked at a distance of 55 m from the setup. To facilitate the measurements at different distances without needing to adjust the mirrors, another visible light laser (the green-light laser shown in Fig. 4.2) is used to track the propagation path of the collimated THz waves.

Collimation, although performed in visible light region, can fail in the THz band due to nonideal effects of the antennas at the receiver and transmitter sides. One of the main challenges over the band of radiation is the varying phase center of the antennas. Therefore, it is critical to take such an effect into account during the measurement. In order to have a realistic expectation of the phase center deviation, electromagnetic simulation is performed

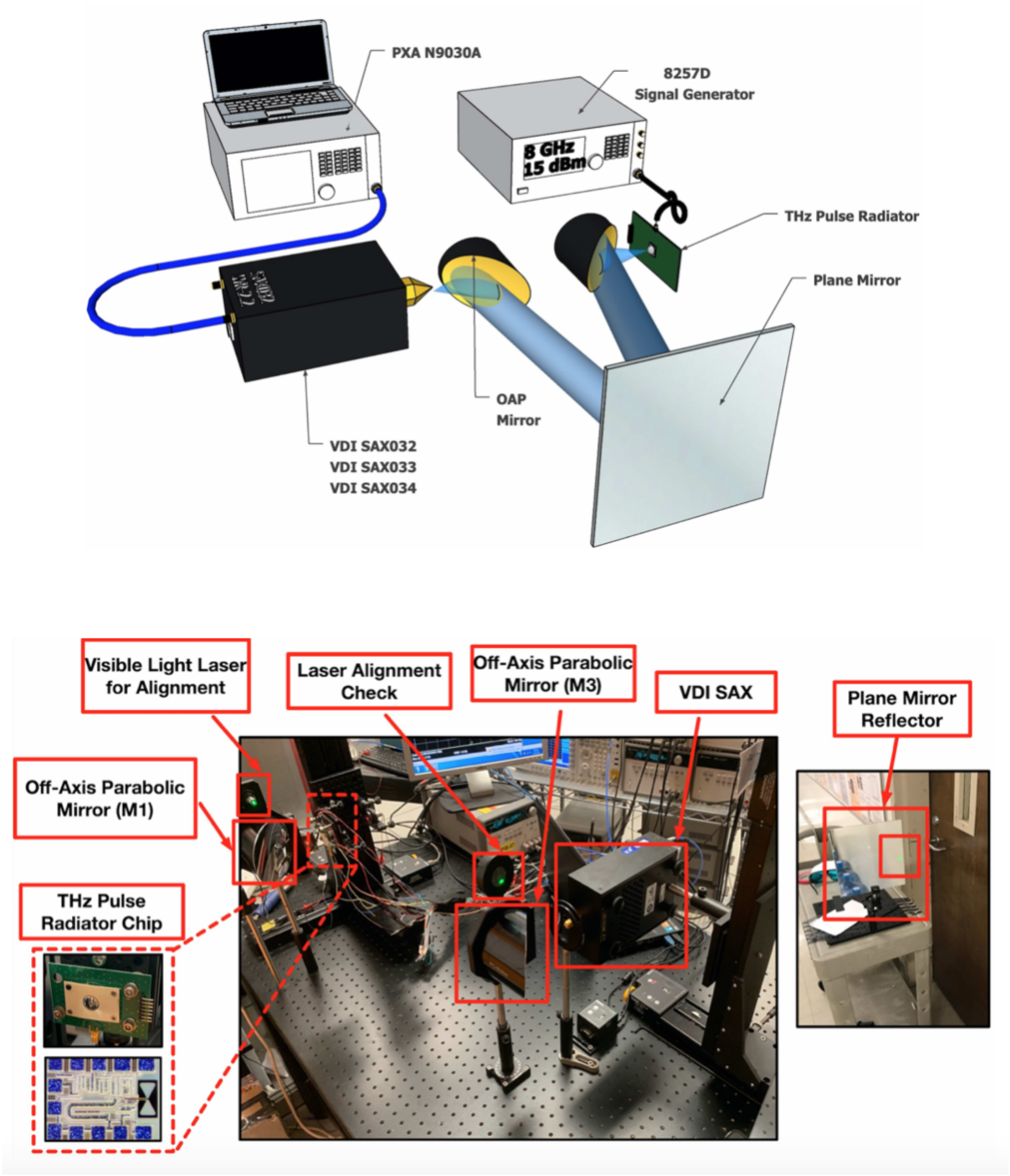

Figure 4.2: A picture of the long-distance THz pulse measurement setup with details of the components and equipment used.

in CST Studio Suite that illustrates the change in the phase center. Fig. 4.3, shows the fluctuations of the phase center for the radiator's antenna.

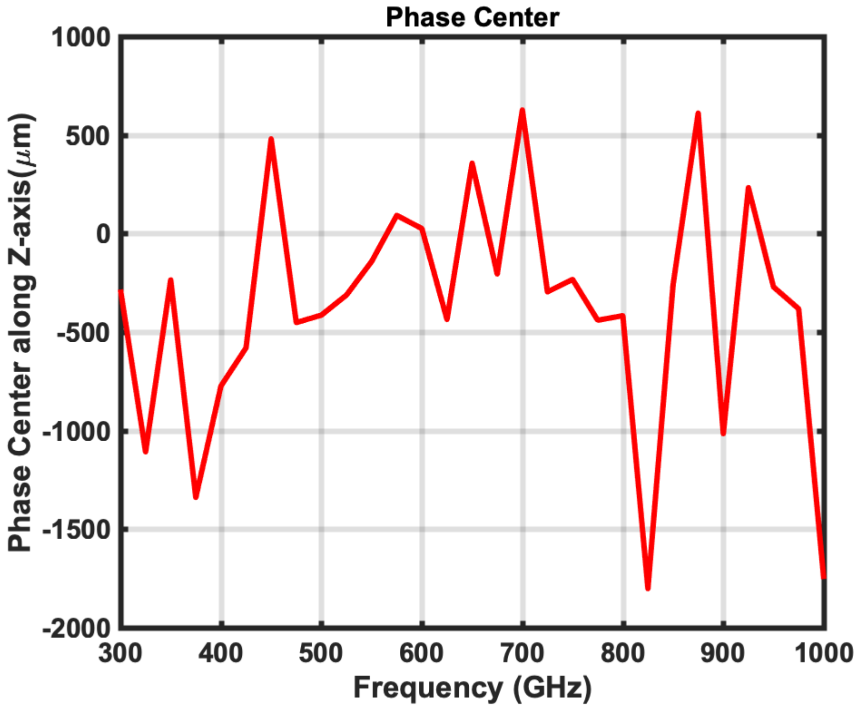

Figure 4.3: Variation of antennas' phase center across THz band for THz impulse transmitter.

As observed, the phase center changes abruptly across the band, which is due the complex structure of the the transmitter's antenna, which consists of a high resistivity silicon lens, doped silicon layer, silicon oxide, and a slot bow-tie (Fig. 4.4).

In order to compensate the phase center fluctuations and maintain collimation, for each frequency point, the position of the chip is adjusted to find the position with the highest received power. The same method is applied at the receiver side. Phase center variations of diagonal horn antennas at the receiver side are calculated based on [120, 121] for each THz frequency band, which is shown in Fig. 4.5.

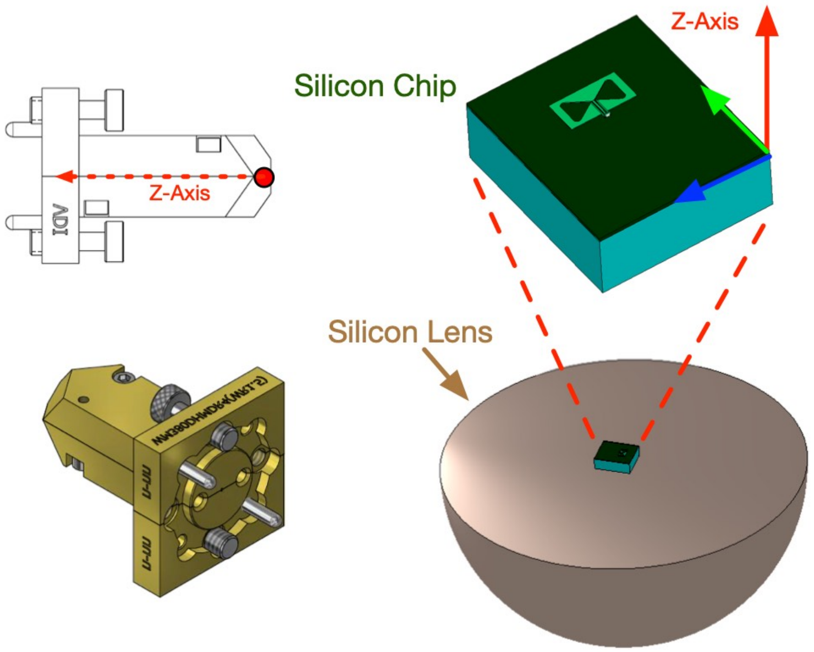

Figure 4.4: Structure of the transmitter and receiver antennas.

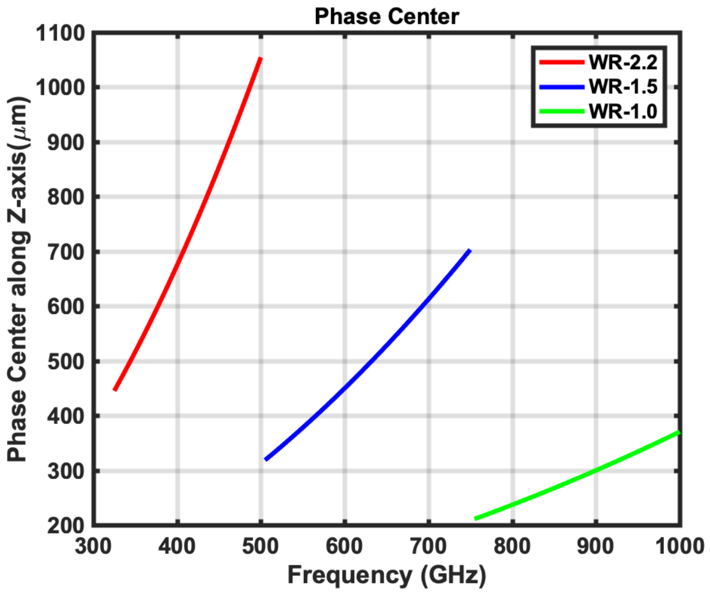

Figure 4.5: Variation of antennas' phase center across THz band for VDI receiver.

Note that this measurement setup can also be utilized for high-speed THz communication applications. To realize this, the radiator needs to have modulation capabilities at the front-end, which is achievable in modern silicon processes considering the advances in THz circuit design over the last few years.

4.3 Measurement Results

Fig. 4.6 shows the power of the received signal over the frequency range of 0.32–1.05 THz and the channel length of 10 to 110 m.

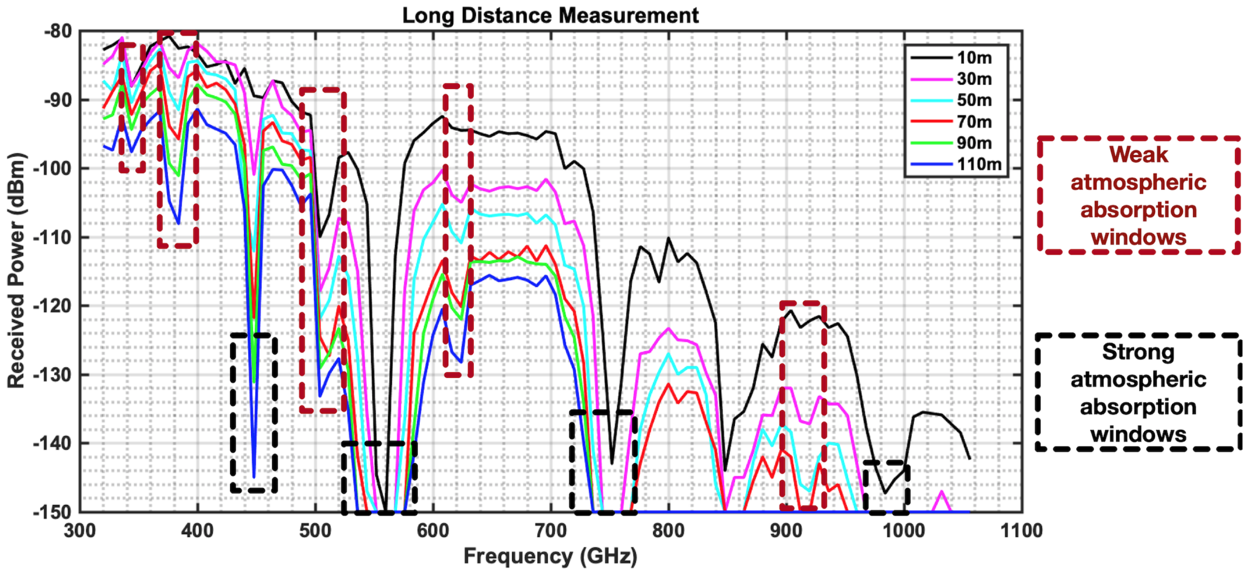

Figure 4.6: Measured received power across the THz band for different propagation distances.

The frequency step of the measurement is 8 GHz, which equals the repetition rate of the external trigger applied to the THz radiator. Note that by varying the repetition rate, the frequency steps can be changed to any arbitrary number, thus enabling us to cover the desired frequency band with a resolution determined by the linewidth of THz tones. The 10-dB linewidth of the THz tones of the THz radiator is less than 2 Hz, which is achieved by locking the repetition rate of the pulses to a low-phase-noise external source. The measured noise floor of the setup is -150 dBm for 1-Hz resolution bandwidth (RBW), which imposes the upper limit on the wireless link range.

As known from equation (4.1), the attenuation of the THz waves can be attributed to two main factors: path loss and absorption. The former directly depends on the propagation distance and the frequency of the propagating wave, which is verified by the results presented in Fig. 4.6. The frequency-dependant absorption stems from the quantized molecular rotational transitions of molecules occurring in the THz regime. Fig. 4.6 illustrates the weak and strong absorption windows due to the presence of water molecules in the atmosphere. These windows are divided into weak and strong windows based on the absorption coefficient. For windows with attenuation above 0.5 dB/m, it is referred to as strong absorption window, whereas attenuation of 0.1–0.5 dB/m is labeled as weak absorption window. The locations of the absorption windows have a strong resemblance with those of the HITRAN database [103]. The results of Fig.4.6 can be used to determine the low-loss frequency windows for long-distance broadband communication, remote sensing, and radar applications.

Fig. 4.7 plots the received power in logarithmic scale versus distance for various frequencies. This figure illustrates the effect of atmospheric absorption on the received power at different frequencies. When fitted to a straight line, different tones have different slopes because of frequency-dependent atmospheric attenuation coefficients. The rate at which the received power declines with distance depends on the absorption as well as path loss caused by imperfect collimation. For instance, at 488-GHz, the slope at which the power drops is less compared to 728-GHz tone, due to different amounts of atmospheric absorption.

The measured weak and strong absorption windows are summarized in Table 4.1. The results are consistent with the HITRAN simulations.

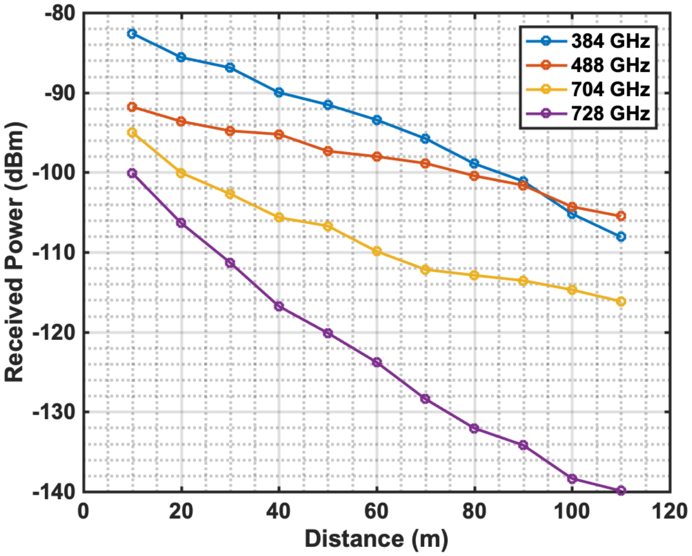

Figure 4.7: Measured received power versus propagation distance.

Table 4.1: THz Absorption Windows

Weak Absorption Windows	Strong Absorption Windows
0.33–0.34 THz	0.44–0.46 THz
0.375–0.39 THz	0.53–0.58 THz
0.48–0.49 THz	0.74–0.77 THz
0.615–0.63 THz	0.96–1 THz
0.91–0.925 THz	–

4.4 Estimation of Absorption Coefficient

In this section, the absorption coefficient is estimated from the received power at a particular frequency. By measuring the received power across different channel lengths, the frequency-dependent atmospheric absorption coefficient α_f is calculated. The received power over different distances can be compared to obtain an estimate of the absorption coefficient at a particular frequency. From equation (1), over two distances d_1 and d_2, the ratio of the received power can be expressed as

$$\alpha_f = 0.2303 \frac{P(d_1)_{r|dB} - P(d_2)_{r|dB} - 20\log(\frac{d_2}{d_1})}{d_2 - d_1}. \tag{4.2}$$

By using (4.2), the atmospheric absorption coefficient can be calculated for a particular frequency in far-field mode. The upper bound of the extracted absorption coefficient is limited by the noise floor of the setup.

The above analysis is valid only in the far-field region, where the THz beams diverge based on Friis theory. In this setup, OAP mirrors are used to collimate the radiated THz beam from the chip. In the case of perfect collimation, the waves are nondivergent; therefore, the attenuation is due simply to absorption rather than path loss factor. However, due to self-diffraction effects, the collimation is never perfect, and the transmitted THz waves acquire a curvature as they propagate along the channel. This effect of divergence is quantified in terms of the Rayleigh range, which is defined as the distance at which the beam width increases by a factor of $\sqrt{2}$. In other words, the effective spot size of the collimated THz beam doubles at this distance. In this study, a 4-inch OAP mirror has been used to collimate the THz waves. The Rayleigh range can be calculated as

$$Z_r = \frac{\pi W_c^2}{\lambda}, \tag{4.3}$$

where W_c is the radius of the OAP reflector antenna, which is 2 inches in the measurement setup (half of the OAP mirror's diameter), and λ is the wavelength. The Rayleigh range for a 4-inch mirror is 8.1 and 27 m at 300 GHz and 1 THz respectively, where the far-field distance is 20.6 and 68.8 m at 300 GHz and 1 THz, respectively. In order to calculate the absorption coefficient at each distance, it is critical to identify the region in which the THz waves are propagating. The on-chip antenna is shown in Fig. 4.8 (a), and the EM simulation is performed using CST Microwave Studio. The far-field pattern is illustrated in Fig. 4.8 (a) at 300, 500, 700, and 1000 GHz. Fig. 4.8 (b) is a symbolic representation of different THz propagation regions.

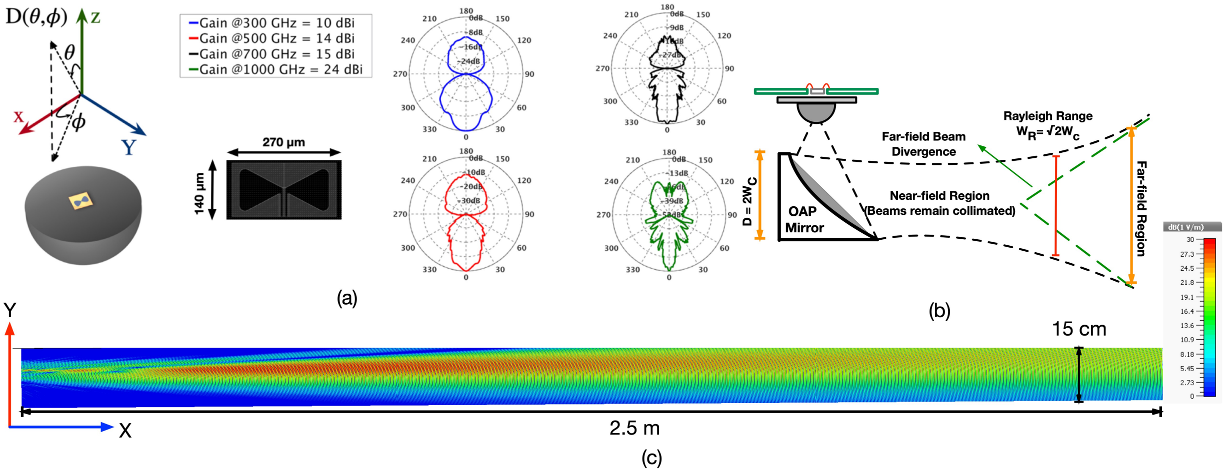

Figure 4.8: (a) Broadband slot bow-tie antenna and its radiation pattern across THz band. (b) Illustration of different propagation regions when an OAP mirror is used. (c) Simulated E-field in Y direction that shows the different propagation regions.

To verify and demonstrate these regions, we use the far-field data of the chip at 300 GHz and the model of a 2-inch OAP mirror for EM simulations. Note that the diameter of the OAP in this simulation is half of the one we used in our measurement to increase the simulation speed. As a result, the Rayleigh range in this simulation is one-quarter of the Rayleigh range in our measurement setup. As shown in Fig. 4.8 (c), results of EM simulation clearly illustrates the divergence of THz waves in 2-m length, which is close to the Rayleigh range of the OAP mirror with 2-inch diameter at 300 GHz.

In the receiving side, by using an OAP with the same dimensions placed at Z_r, half of the transmitted power is lost due to diffraction. Equation (5) also shows that with an increase in the frequency of the radiated signal, the Rayleigh range increases. Therefore, the waves can remain collimated for longer distances at higher frequencies. Depending on the frequency of the radiated signal, the resulting beam width can be expressed in terms of distance from the source as

$$W(d) = W_c\sqrt{1+(\frac{d}{Z_r})^2}, \tag{4.4}$$

where W is the effective beam radius after propagating a distance d from the source. As a result, the ratio of the received power at two distances d_1 and d_2 can be represented as

$$\frac{P_r(d_1)}{P_r(d_2)} = Ke^{\alpha_f(d_2-d_1)}, \tag{4.5}$$

where K is a factor that estimates for the power loss due to divergence of THz beams (or spot size change) and can be expressed as

$$K = \frac{1 + (\frac{d_2}{Z_r})^2}{1 + (\frac{d_1}{Z_r})^2}. \tag{4.6}$$

K is a function of the frequency of the radiated signal and the distances taken into consideration. In the near-filed region, the absorption coefficient can be approximated as

$$\alpha_f = 0.2303 \frac{P(d1)_{r|dB} - P(d2)_{r|dB} - 10\log(K)}{d_2 - d_1}. \tag{4.7}$$

Fig. 4.9 plots the atmospheric absorption coefficient for frequencies in the range of 0.3–0.9 THz using (4.6) and (4.7).

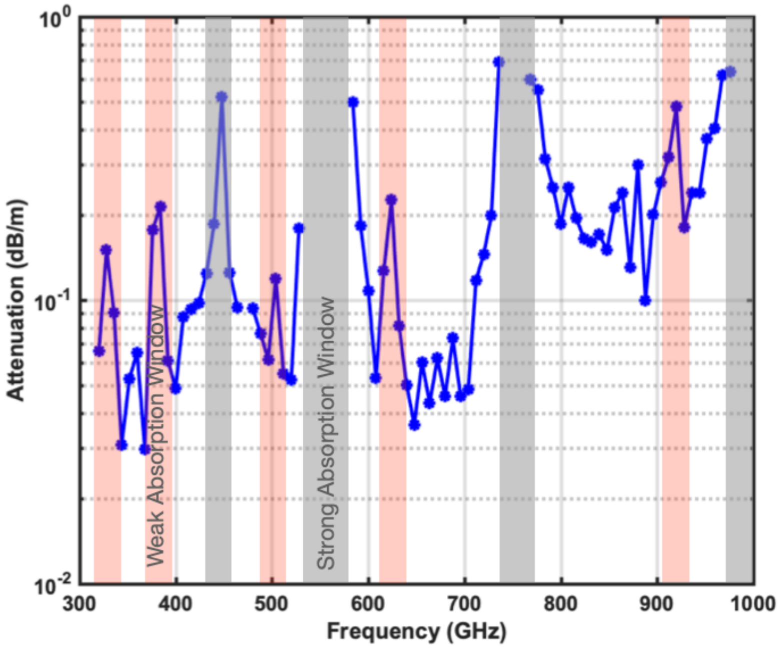

Figure 4.9: Calculated attenuation based on measurement results.

Note that to calculate the absorption coefficient, the points below the Rayleigh range for each frequency was used. Therefore, equation (4.7), was used for calculations in near filed region; however, there are still minor errors in calculation of K since the radiated THz waves are not ideal Gaussian beams.

The lower limit of the atmospheric absorption coefficient is set by the amplitude stability of the source, and the upper limit is set by the noise floor of the setup. The relative strengths and the positions of the absorption coefficient peaks are consistent with the HITRAN simulations [103].

4.5 Chapter Summary

This chapter presents the results of indoor THz wireless channel characterization using a low-power, custom-designed impulse radiator chip. A broadband radiator eliminates the need for multiple radiating sources to cover a broad range of frequencies. A THz non-line-of-sight link is designed that can be used for communication and broadband sensing applications. In addition, the use of a silicon process to design the radiator enables integrating an array of radiators on a single die, which is a practical solution for increasing the propagation range.

Using a customized measurement setup, channel characterization is performed for frequencies in the range of 0.3–1 THz for a distance of 10–to–110 m in steps of 10 m. A comparison of this study with other atmospheric channel characterization attempts is presented in Table II. Due to the use of a customized silicon-based broadband THz pulse radiator, this study benefits from low cost and high integration compared to previously proposed techniques. Frequency windows with strong water-vapor absorption, as well as low-loss windows suitable for wireless propagation in a low-THz regime, are identified from the measurement results. Moreover, the results demonstrate the feasibility of using low-power THz silicon radiators for applications such as high-speed communications, high-resolution remote sensing, and radars. To the best of the authors' knowledge, this is the first time THz propagation up to a distance of 110 m using a low-power silicon-based radiator that covers the 320–1000 GHz frequency range has been demonstrated.

4.6 Acknowledgment

The authors thank the National Science Foundation Career Award program for partially supporting the work.

Table 4.2: Comparison of THz Channel Characterization with Previous Studies

	This work	[122]	[123]	[124]	[125]
Maximum distance (m)	**110**	167	910	100	0.67
Frequency range (THz)	**0.32–1.1**	0.1–1	0.1–1	0.1–0.4	0.1–2
Frequency steps (GHz)	**8**†	0.0898	0.0084	100	2–3
Source output power (dBm)	**19.2 (EIRP)**	-45.3	-45.3	10*	-
THz source	**Custom-designed 130-nm SiGe BiCMOS chip**	Femtosecond laser (THz-TDS)	Femtosecond laser (THz-TDS)	Virginia Diodes Multiplier	Picometrix T-Ray 4000 (THz-TDS)

[*] 10 dBm @ 400 GHz, 8.5 dBm @ 300 GHz, 20 dBm at 200 GHz, and 24 dBm @ 100 GHz.

[†] Tunable from 10s of MHz up to 8 GHz with the resolution of 2 Hz, which is limited by the phase noise.

CHAPTER 5

Conclusion

This dissertation presents a fully integrated laser-free terahertz impulse transceiver in silicon that can radiate and detect arbitrary signals in the millimeter-wave and terahertz bands with a 2 Hz frequency resolution. This design was developed in commercially available silicon technologies and their performances were evaluated through measurements.

Conventional THz radiators and detectors suffer from high power consumption, high cost, and bulky measurement setups due to the requirement of a femtosecond laser source, which limits their accessibility and ability to be mass-produced. Thus, there has been a tendency to implement THz systems in electronics, including both silicon and III–V substrates.

The transistor speed in silicon-based technologies has been improving over the last several decades, making electronic THz systems a low-cost alternative for optical systems. One of the main challenges in realizing efficient integrated THz systems in silicon is the generation and detection of signals beyond the f_{max} of a transistor. This is an important metric because it fundamentally defines the maximum frequency at which the device can provide power amplification. Continuous-wave signal generation and detection or impulse-based systems are the two main approaches used for THz electromagnetic wave generation and detection beyond the f_{max} of the transistor in silicon-based technologies. Recently, oscillator-free architectures have been introduced to radiate and detect signals in the THz regime, which utilizes a nonlinear current-switching mechanism to generate a reference frequency comb. Unlike conventional signal generation and detection techniques in the THz regime, the D2I method does not rely on an oscillator.

Chapter 2 described a fully integrated silicon-based laser-free oscillator-free terahertz impulse radiator. This THz transmitter radiates 2.5 picosecond impulses, corresponding to a frequency comb with 1.052 THz bandwidth. In addition, this chip can transmit 4 Gb/s data with the non-return-to-zero inverted on-off keying modulation scheme. A 2 m specular non-line-of-sight communication link for long-range wireless applications is built using this transmitter, parabolic reflector antennas, and a plane mirror. This chip is fabricated in 130 nm SiGe BiCMOS process technology, occupies a total die area of 1.26 mm^2 and consumes 206 mW of dc power.

Chapter 3 introduced an oscillator-free frequency comb-based coherent detector with an on-chip antenna for sensing and imaging applications in mm-wave and THz frequencies. This design detects arbitrary signals from 20 to 500 GHz with 2-Hz frequency resolution. A peak sensitivity of -100 dBm is measured with 1 KHz resolution bandwidth. The frequency spacing in the on-chip reference frequency comb is tunable and set to 4 GHz. A chip-to-chip dual-frequency comb measurement setup is successfully implemented using this receiver and the impulse transmitter (chapter two). This setup is characterized in the 20-220 GHz frequency range. This chip is fabricated in 130 nm SiGe BiCMOS process technology, occupies a total die area of 1.26 mm^2 and consumes 206 mW of dc power.

Chapter 4 presented a long-path THz communication channel characterization in the frequency range of 0.32–1.1 THz using a customized, silicon-based THz pulse radiator chip. A specular link was created using an impulse radiator, parabolic reflector antennas, a plane mirror, and a downconverter mixer. The THz channel was characterized up to a distance of 110 m. The measurement results demonstrated channel path loss, atmospheric absorption, and low-loss frequency windows suitable for wireless links in the THz range.

In summary, the integrated circuits presented in this dissertation demonstrate that silicon technologies are a promising low-cost alternative for conventional THz radiation and detection techniques. With the improvement in silicon technologies, the performance of silicon-based THz systems is expected to improve in the near future. Therefore, although the THz domain has been barely explored, the growth of THz light in everyday applications is inevitable.

REFERENCES

[1] M. Tonouchi, “Cutting-edge terahertz technology,” Nature Photonics, vol. 1, pp. 97–105, Feb. 2007.

[2] R. Han et al., “Filling the Gap: Silicon Terahertz Integrated Circuits Offer Our Best Bet,” in IEEE Microwave Magazine, vol. 20, no. 4, pp. 80-93, April 2019.

[3] Williams, B., “Terahertz quantum-cascade lasers,” Nature Photon 1, 517–525 (2007).

[4] K. K.O. et al., “Opening Terahertz for Everyday Applications,” in IEEE Communications Magazine, vol. 57, no. 8, pp. 70-76, August 2019.

[5] H. Aggrawal, P. Chen, M. M. Assefzadeh, B. Jamali and A. Babakhani, “Gone in a Picosecond: Techniques for the Generation and Detection of Picosecond Pulses and Their Applications,” in IEEE Microwave Magazine, vol. 17, no. 12, pp. 24-38, Dec. 2016.

[6] K. Sengupta, T. Nagatsuma, and D. M. Mittleman, “Terahertz integrated electronic and hybrid electronic-photonic systems,” Nature Electronics, vol. 1, no. 12, pp. 622–635, 2018.

[7] John Federici and Lothar Moeller, “Review of terahertz and subterahertz wireless communications,” Journal of Applied Physics 107, 111101 (2010).

[8] H. Elayan, O. Amin, R. M. Shubair and M. Alouini, “Terahertz communication: The opportunities of wireless technology beyond 5G,” 2018 International Conference on Advanced Communication Technologies and Networking (CommNet), 2018, pp. 1-5.

[9] H. Elayan, O. Amin, B. Shihada, R. M. Shubair and M. -S. Alouini, “Terahertz Band: The Last Piece of RF Spectrum Puzzle for Communication Systems,” in IEEE Open Journal of the Communications Society, vol. 1, pp. 1-32, 2020.

[10] Rogalski, A. and Sizov, F.. “Terahertz detectors and focal plane arrays” Opto-Electronics Review, vol. 19, no. 3, 2011, pp. 346-404.

[11] D’Arco A, Di Fabrizio M, Dolci V, Petrarca M, Lupi S. “THz Pulsed Imaging in Biomedical Applications,” Condensed Matter. 2020.

[12] Leahy-Hoppa, Megan R.. “Terahertz For Weapon And Explosive Detection.” WIT Transactions on State-of-the-art in Science and Engineering 54 (2012).

[13] N. Born et al., ”Monitoring the water status of plants using THz radiation,” 2014 39th International Conference on Infrared, Millimeter, and Terahertz waves (IRMMW-THz), 2014, pp. 1-2.

[14] B. B. Hu and M. C. Nuss, “Imaging with terahertz waves,” Opt. Lett. 20, 1716-1718 (1995).

[15] Z. D. Taylor, R. S. Singh, M. O. Culjat, J. Y. Suen, W. S. Grundfest, H. Lee, and E. R. Brown, “Reflective terahertz imaging of porcine skin burns,” Opt. Lett. 33, 1258-1260 (2008).

[16] Joo-Hiuk Son, Seung Jae Oh, and Hwayeong Cheon, “Potential clinical applications of terahertz radiation,” Journal of Applied Physics 125, 190901 (2019).

[17] Habibagahi, I., Omidbeigi, M., Hadaya, J. et al. “Vagus nerve stimulation using a miniaturized wirelessly powered stimulator in pigs,” Sci Rep 12, 8184 (2022).

[18] J. Jang, I. Habibagahi, H. Rahmani and A. Babakhani, “Wirelessly Powered, Batteryless Closed-loop Biopotential Recording IC for Implantable Leadless Cardiac Monitoring Applications,” 2021 IEEE Biomedical Circuits and Systems Conference (BioCAS), 2021.

[19] C. S. Joseph, A. N. Yaroslavsky, V. A. Neel, T. M. Goyette and R. H. Giles, “Continuous wave terahertz transmission imaging of nonmelanoma skin cancers”, Lasers Surg. Med., vol. 43, no. 6, pp. 457-462, Aug. 2011.

[20] Fitzgerald AJ, Wallace VP, Jimenez-Linan M, Bobrow L, Pye RJ, Purushotham AD, Arnone DD., “Terahertz pulsed imaging of human breast tumors,” Radiology. 2006 May;239(2):533-40.

[21] Nagendra Paradad Yadav, Guo-Zhen Hu, Zheng-Peng Yao, Ashish Kumar, “Diagnosis of dental problem by using terahertz technology,” Journal of Electronic Science and Technology, Volume 19, Issue 3, 2021.

[22] J. F. Federici, B. Schulkin, F. Huang, D. Gary, R. Barat, F. Oliveira, and D. Zimdars, “THz imaging and sensing for security applications—explosives, weapons and drugs,” Semiconductor Science and Technology, 20(7), S266–S280, doi: 10.1088/0268-1242/20/7/018.

[23] R. Fukasawa, “Terahertz Imaging: Widespread Industrial Application in Nondestructive Inspection and Chemical Analysis,” in IEEE Transactions on Terahertz Science and Technology, vol. 5, no. 6, pp. 1121-1127, Nov. 2015.

[24] Katsuhiro Ajito, Yuko Ueno, Ho-Jin Song, Emi Tamechika Naoya Kukutsu (2011) Terahertz Spectroscopic Imaging of Polymorphic Forms in Pharmaceutical Crystals, Molecular Crystals and Liquid Crystals, 538:1, 33-38.

[25] D. Wang et al., “Integrated 240-GHz Dielectric Sensor With dc Readout Circuit in a 130-nm SiGe BiCMOS Technology,” in IEEE Transactions on Microwave Theory and Techniques, vol. 66, no. 9, pp. 4232-4241, Sept. 2018.

[26] R. Ebrahimi Ghiri, E. Kaya and K. Entesari, “Time-Domain Dielectric Spectroscopy Using a Miniaturized Contact-Based UWB System,” in IEEE Transactions on Microwave Theory and Techniques, vol. 66, no. 12, pp. 5863-5872, Dec. 2018.

[27] Cuisset, A.; Hindle, F.; Mouret, G.; Bocquet, R.; Bruckhuisen, J.; Decker, J.; Pienkina, A.; Bray, C.; Fertein, É.; Boudon, V. “Terahertz Rotational Spectroscopy of Greenhouse Gases Using Long Interaction Path-Lengths,” Appl. Sci. 2021, 11, 1229.

[28] T. Globus et al., “Highly Resolved Sub-Terahertz Vibrational Spectroscopy of Biological Macromolecules and Cells,” in IEEE Sensors Journal, vol. 13, no. 1, pp. 72-79, Jan. 2013.

[29] H. Zhong, A. Redo-Sanchez, and X.-C. Zhang, “Identification and classification of chemicals using terahertz reflective spectroscopic focal-plane imaging system,” Opt. Express 14(20), 9130–9141 (2006).

[30] K. Ajito, “Terahertz Spectroscopy for Pharmaceutical and Biomedical Applications,” in IEEE Transactions on Terahertz Science and Technology, vol. 5, no. 6, pp. 1140-1145, Nov. 2015.

[31] N. Shimizu et al., “Remote gas sensing in full-scale fire with sub-terahertz waves,” 2011 IEEE MTT-S International Microwave Symposium, 2011, pp. 1-4.

[32] B. M. Fischer, H. Helm and P. U. Jepsen, “Chemical Recognition With Broadband THz Spectroscopy,” in Proceedings of the IEEE, vol. 95, no. 8, pp. 1592-1604, Aug. 2007.

[33] R. You, Z. Lu, Q. Hou and T. Jiang, “Study of pollution air monitoring system based on space-borne terahertz radiometer,” 2017 10th UK-Europe-China Workshop on Millimetre Waves and Terahertz Technologies (UCMMT), 2017, pp. 1-4.

[34] A.A. Gowen, C. O'Sullivan, C.P. O'Donnell, "Terahertz time domain spectroscopy and imaging: Emerging techniques for food process monitoring and quality control," Trends in Food Science Technology, Volume 25, Issue 1, 2012, Pages 40-46.

[35] P. H. Bolivar, M. Brucherseifer, M. Nagel, H. Kurz, A. Bosserhoff, and R. Buttner, "Label-free probing of genes by time domain terahertz sensing," Phys. Med. Biol., vol. 47, no. 21, pp. 3815–3821, Nov. 2002.

[36] Akter N, Hasan MM, Pala N. A "Review of THz Technologies for Rapid Sensing and Detection of Viruses including SARS-CoV-2," Biosensors. 2021; 11(10):349.

[37] Mittleman, D., Jacobsen, R., Neelamani, R. et al. "Gas sensing using terahertz time-domain spectroscopy . Appl Phys B 67, 379–390 (1998).

[38] Y. Mehta, S. Razavian, K. Schwarm, R. M. Spearrin, and A. Babakhani, "Terahertz Gas-phase Spectroscopy of CO using a Silicon-based Picosecond Impulse Radiator," in Conference on Lasers and Electro-Optics, OSA Technical Digest (Optica Publishing Group, 2020), paper SM2F.7.

[39] M. M. Assefzadeh et al., "Terahertz trace gas spectroscopy based on a fully-electronic frequency-comb radiating array in silicon," 2016 Conference on Lasers and Electro-Optics (CLEO), 2016, pp. 1-2.

[40] S. Razavian, M. M. Assefzadeh, M. Hosseini and A. Babakhani, "THz Micro-Doppler Measurements Based On A Silicon-Based Picosecond Pulse Radiator," 2019 IEEE MTT-S International Microwave Symposium (IMS), 2019, pp. 309-311.

[41] S. Razavian, S. Thomas, M. Hosseini and A. Babakhani, "Micro-Doppler Detection and Vibration Sensing using Silicon-based THz Radiators," in IEEE Sensors Journal, 2022.

[42] M. Jian, Z. Lu and V. C. Chen, "Drone detection and tracking based on phase-interferometric Doppler radar," 2018 IEEE Radar Conference (RadarConf18), 2018, pp. 1146-1149.

[43] S. Razavian et al., "Plasma Characterization Using a Silicon-Based Terahertz Frequency Comb Radiator," in IEEE Sensors Letters, vol. 4, no. 9, pp. 1-4, Sept. 2020, Art no. 3501304.

[44] S. Matsuura, M. Tani, and K. Sakai, "Generation of coherent terahertz radiation by photomixing in dipole photoconductive antennas," Applied Physics Letters, vol. 70, no. 5, pp. 559–561, 1997. 3.1.

[45] Burford, Nathan M., and Magda O. El-Shenawee. “Review of terahertz photoconductive antenna technology.” Optical Engineering 56, no. 1 (2017): 010901.

[46] Berry, Christopher W., and Mona Jarrahi. “Terahertz generation using plasmonic photoconductive gratings,” New Journal of Physics 14.10 (2012): 105029.

[47] Preu S, Dohler G H, Malzer S, Wang L J and Gossard A C 2011 Tunable, “Continuous-wave terahertz photomixer sources and applications,” J. Appl. Phys.

[48] Tani, Masahiko, Shuji Matsuura, Kiyomi Sakai, and Shin-ichi Nakashima. ”Emission characteristics of photoconductive antennas based on low-temperature-grown GaAs and semi-insulating GaAs,” Applied optics 36, no. 30 (1997): 7853-7859.

[49] Nuss, Martin C., and Joseph Orenstein. ”Terahertz time-domain spectroscopy.” Millimeter and submillimeter wave spectroscopy of solids (1998): 7-50.

[50] P. Chen, M. Hosseini, and A. Babakhani, “An Integrated Germanium-Based THz Impulse Radiator with an Optical Waveguide Coupled Photoconductive Switch in Silicon.” Micromachines. 2019; 10(6):367.

[51] P. Chen, M. Hosseini, and A. Babakhani, “An integrated germanium-based optical waveguide coupled THz photoconductive antenna in silicon,” 2016 Conference on Lasers and Electro-Optics (CLEO), 2016, pp. 1-2.

[52] Nicola Peserico, Hangbo Yang, Xiaoxuan Ma, Shurui Li, Zibu Hu, Mostafa Hosseini, Aydin Babakhani, Puneet Gupta, Chee Wei Wong, Volker J. Sorger, “PIC-based joint transform correlator CNN,” Proc. SPIE PC12019, AI and Optical Data Sciences III, PC120190L (9 March 2022).

[53] Gonzalez, G. “Microwave Transistor Amplifiers: Analysis and Design,” 2nd edn, (Prentice-Hall, Upper Saddle River, 1997).

[54] . Mei et al., “First Demonstration of Amplification at 1 THz Using 25-nm InP High Electron Mobility Transistor Process,” in IEEE Electron Device Letters, vol. 36, no. 4, pp. 327-329, April 2015.

[55] U. R. Pfeiffer, E. Ojefors, A. Lisauskas and H. G. Roskos, “Opportunities for silicon at mmWave and Terahertz frequencies,” 2008 IEEE Bipolar/BiCMOS Circuits and Technology Meeting, 2008, pp. 149-156.

[56] P. Chevalier et al., "Si/SiGe:C and InP/GaAsSb Heterojunction Bipolar Transistors for THz Applications," in Proceedings of the IEEE, vol. 105, no. 6, pp. 1035-1050, June 2017.

[57] B. Heinemann, H. Rcker, R. Barth, F. Brwolf, J. Drews, G. G. Fischer, A. Fox, O. Fursenko, T. Grabolla, F. Herzel, J. Katzer, J. Korn, A. Krger, P. Kulse, T. Lenke, M. Lisker, S. Marschmeyer, A. Scheit, D. Schmidt, J. Schmidt, M. A. Schubert, A. Trusch, C. Wipf, and D. Wolansky, "SiGe HBT with ft/fmax of 505 GHz/720 GHz," in 2016 IEEE International Electron Devices Meeting (IEDM), Dec 2016, pp. 3.1.1–3.1.4.

[58] O. Momeni and E. Afshari, "High Power Terahertz and Millimeter-Wave Oscillator Design: A Systematic Approach," in IEEE Journal of Solid-State Circuits, vol. 46, no. 3, pp. 583-597, March 2011.

[59] R. Han and E. Afshari, "A high-power broadband passive terahertz frequency doubler in cmos," IEEE Transactions on Microwave Theory and Techniques, vol. 61, no. 3, pp. 1150–1160, 2013.

[60] B. Cetinoneri, Y. Atesal, A. Fung, and G. Rebeiz, "W-band amplifiers with 6-dB noise figure and milliwatt-level 170–200-GHz doublers in 45-nm CMOS," IEEE Trans. Microw. Theory Tech., vol. 60, no. 3, pp. 692–701, Mar. 2012.

[61] S. Razavian and A. Babakhani, "A Highly Power Efficient 2×3 PIN-Diode-Based Intercoupled THz Radiating Array at 425GHz with 18.1dBm EIRP in 90nm SiGe BiCMOS," 2022 IEEE International Solid- State Circuits Conference (ISSCC), 2022, pp. 1-3.

[62] Y. Tousi, O. Momeni, and E. Afshari, "A 283-to-296 GHz VCO with 0.76 mW peak output power in 65 nm CMOS," in IEEE Int. Solid-State Circuits Conf. Dig. Tech. Papers, Feb. 2012, pp. 258–259.

[63] A. Arbabian, S. Callender, S. Kang, M. Rangwala, and A. M. Niknejad, "A 94 GHz mm-wave-to-baseband pulsed-radar transceiver with applications in imaging and gesture recognition," IEEE Journal of Solid-State Circuits, vol. 48, no. 4, pp. 1055–1071, April 2013.

[64] X. Wu and K. Sengupta, "Programmable picosecond pulse generator in cmos," in Microwave Symposium (IMS), 2015 IEEE MTT-S International. IEEE, 2015, pp. 1–4.

[65] M. M. Assefzadeh and A. Babakhani, "Broadband Oscillator-Free THz Pulse Generation and Radiation Based on Direct Digital-to-Impulse Architecture," IEEE Journal of Solid-State Circuits, 2017.

[66] P. Chen, M. M. Assefzadeh and A. Babakhani, “A Nonlinear Q-Switching Impedance Technique for Picosecond Pulse Radiation in Silicon,” in IEEE Transactions on Microwave Theory and Techniques, vol. 64, no. 12, pp. 4685-4700, Dec. 2016.

[67] S. Razavian and A. Babakhani, “A THz Pulse Radiator Based on PIN Diode Reverse Recovery,” 2019 IEEE BiCMOS and Compound semiconductor Integrated Circuits and Technology Symposium (BCICTS), Nashville, TN, USA, 2019, pp. 1–4.

[68] Jamali, B., Razavian, S. and Babakhani, A., 2020, March. “Fully electronic silicon-based THz pulse sources and detectors,” In Terahertz Photonics (Vol. 11348, pp. 41-48). SPIE.

[69] B. Jamali and A. Babakhani, “A Fully Integrated 50–280-GHz Frequency Comb Detector for Coherent Broadband Sensing,” in IEEE Transactions on Terahertz Science and Technology, vol. 9, no. 6, pp. 613-=623, Nov. 2019.

[70] M. Hosseini and A. Babakhani, “A 4-Gb/s Laser-Free Picosecond Impulse Transmitter With a Broadband On-Chip Antenna,” 2020 45th International Conference on Infrared, Millimeter, and Terahertz Waves (IRMMW-THz), 2020, pp. 1-2.

[71] A. Babakhani, X. Guan, A. Komijani, A. Natarajan, and A. Hajimiri, “A 77-GHz Phased-Array Transceiver With On-Chip Antennas in Silicon: Receiver and Antennas,” pp. 2795–2806, 2006.

[72] Y.-L. Chen, C.-L. Ruan, and L. Peng, “A novel ultra-wideband bow-tie slot antenna in wireless communication systems,” Progress In Electromagnetics Research Letters, vol. 1, pp. 101–108, 2008.

[73] K. Chung, S. Pyun, and J. Choi, “Design of an ultrawide-band TEM horn antenna with a microstrip-type balun,” IEEE Trans. Antennas Propag., vol. 53, no. 10, pp. 3410–3413, Oct. 2005.

[74] S.-W. Qu, J.-L. Li, Q. Xue, and C. H. Chan, “Wideband cavity-backed bowtie antenna with pattern improvement,” IEEE Transactions on Antennas and Propagation, vol. 56, no. 12, pp. 3850–3854, 2008.

[75] M. Hosseini, M. Assefzadeh, S. Razavian, Y. Mehta and A. Babakhani, “Terahertz Channel Characterization using a Silicon-based Picosecond Pulse Source,” 2020 IEEE Radio and Wireless Symposium (RWS), 2020, pp. 76-79.

[76] S. Razavian, M. Hosseini, Y. Mehta and A. Babakhani, “Terahertz Channel Characterization Using a Broadband Frequency Comb Radiator in 130-Nm SiGe BiCMOS,” in IEEE Transactions on Terahertz Science and Technology, vol. 11, no. 3, pp. 269-276, May 2021.

[77] P. Chen and A. Babakhani, “A 30GHz impulse radiator with on-chip antennas for high-resolution 3D imaging,” in 2015 IEEE Radio and Wireless Symposium (RWS), Jan 2015, pp. 32–34.

[78] M. Assefzadeh and A. Babakhani, “A 9-psec dierential lens-less digital-to-impulse radiator with a programmable delay line in silicon,” in Radio Frequency Integrated Circuits Symposium, 2014 IEEE, June 2014, pp. 307–310.

[79] S. Razavian and A. Babakhani, “Silicon Integrated THz Comb Radiator and Receiver for Broadband Sensing and Imaging Applications,” in IEEE Transactions on Microwave Theory and Techniques, vol. 69, no. 11, pp. 4937-4950, Nov. 2021.

[80] M. Hosseini and A. Babakhani, “A Fully Integrated 20-500-GHz Coherent Detector with 2-Hz Frequency Resolution,” 2020 IEEE BiCMOS and Compound Semiconductor Integrated Circuits and Technology Symposium (BCICTS), 2020, pp. 1-4.

[81] S. V. Thyagarajan, S. Kang, and A. M. Niknejad, “A 240 GHz fully integrated wideband QPSK receiver in 65 nm CMOS,” IEEE Journal of Solid-State Circuits, vol. 50, no. 10, pp. 2268–2280, Oct. 2015.

[82] Z. Hu, C. Wang, and R. Han, “A 32-unit 240-GHz heterodyne receiver array in 65-nm CMOS with array-wide phase locking,” IEEE Journal of Solid-State Circuits, vol. 54, no. 5, pp. 1216–1227, May 2019.

[83] S. Razavian and A. Babakhani, “A Fully Integrated Coherent 50–500-GHz Frequency Comb Receiver for Broadband Sensing and Imaging Applications,” 2020 IEEE Radio Frequency Integrated Circuits Symposium (RFIC), Los Angeles, CA, USA, 2020.

[84] B. Jamali and A. Babakhani, “A Fully Integrated 30-to-160GHz Coherent Detector with a Broadband Frequency Comb in 65nm CMOS,” 2019 14th European Microwave Integrated Circuits Conference (EuMIC), 2019, pp. 104-107.

[85] C. Jiang, A. Mostajeran, R. Han, M. Emadi, H. Sherry, A. Cathelin, and E. Afshari, “A 320GHz subharmonic-mixing coherent imager in 0.13m SiGe BiCMOS,” in 2016 IEEE Intl. Solid-State Circuits Conf. (ISSCC), Jan. 2016, pp. 432–434.

[86] Q. Zhong, W. Choi, C. Miller, R. Henderson, and K. K. O, “ A 210-to-305GHz CMOS receiver for rotational spectroscopy,” in 2016 IEEE Intl. Solid- State Circuits Conf. (ISSCC), Jan. 2016, pp. 426–427.

[87] M. J. W. Rodwell, M. Kamegawa, R. Yu, M. Case, E. Carman, and K. S. Giboney, “GaAs nonlinear transmission lines for picosecond pulse generation and millimeter-wave sampling,” IEEE Transactions on Microwave Theory and Techniques, vol. 39, no. 7, pp. 1194–1204, July 1991.

[88] M. K. Matters-Kammerer, D. van Goor, and L. Tripodi, “20GHz to 480GHz on-chip broadband spectrometer in 65-nm CMOS technology,” in 2016 46th European Microwave Conference (EuMC), Oct. 2016, pp. 349–352.

[89] M. K. Matters-Kammerer, D. van Goor, and L. Tripodi, “Broadband sub-THz spectroscopy modules integrated in 65-nm CMOS technology,” Intl. Journal of Microwave and Wireless Technologies, vol. 9, no. 6, pp. 1211–1218, 2017.

[90] D. W. van der Weide and F. Keilmann, “Coherent periodically pulsed radiation spectrometer,” May 1998, US Patent 5,748,309.

[91] Schliesser, A., Picqué, N. Hänsch, T. “Mid-infrared frequency combs,” Nature Photon 6, 440–449 (2012).

[92] A. Schliesser, M. Brehm, F. Keilmann, and D. W. van der Weide, “Frequency-comb infrared spectrometer for rapid, remote chemical sensing,” Optics Express, vol. 13, no. 22, pp. 9029–9038, Oct. 2005.

[93] I. Coddington, W. C. Swann, and N. R. Newbury, “Coherent dual-comb spectroscopy at high signal-to-noise ratio,” Physical Review A, vol. 82, p. 043817, Oct. 2010.

[94] P. Chen, M. M. Assefzadeh, and A. Babakhani, “Time-domain characterization of silicon-based integrated picosecond impulse radiators,” IEEE Transactions on Terahertz Science and Technology, vol. 7, no. 5, pp. 599–608, Sep. 2017.

[95] I. Coddington et al., “Dual-comb spectroscopy,” Optica 3, 2016.

[96] N. Sinha, M. Rachid, S. Pavan, and S. Pamarti, “Design and analysis of an 8 mW, 1 GHz span, passive spectrum scanner with ¿+31 dBm out-of-band IIP3 using periodically time-varying circuit components,” IEEE Journal of Solid- State Circuits, vol. 52, no. 8, pp. 2009–2025, Aug. 2017.

[97] D. M. Pozar, “Microwave and RF Design of Wireless Systems,” United Kingdom, Wiley, 2001.

[98] X. Wu and K. Sengupta, “A 40-to-330GHz synthesizer-free THz spectroscope-on-chip exploiting electromagnetic scattering,” in 2016 IEEE Intl. Solid-State Circuits Conf. (ISSCC), Jan. 2016, pp. 428–429.

[99] C. Wang and R. Han, “Dual-terahertz-comb spectrometer on cmos for rapid, wide- range gas detection with absolute specificity,” IEEE Journal of Solid-State Circuits, vol. 52, no. 12, pp. 3361–3372, 2017.

[100] T. Chi, M. Huang, S. Li, and H. Wang, “A packaged 90-to-300ghz transmitter and 115-to-325ghz coherent receiver in cmos for full-band continuous-wave mm-wave hyper-spectral imaging,” in 2017 IEEE International Solid-State Circuits Conference (ISSCC), 2017, pp. 304–305.

[101] Y. Zhu, H. Wang, K. Kang, and O. Momeni, “A low power sub-harmonic self-oscillating mixer with 16.8db conversion loss at 310ghz in 65nm cmos,” in 2019 IEEE Custom Integrated Circuits Conference (CICC), 2019, pp. 1–4.

[102] Z. Hu, C. Wang, and R. Han, “A 32-unit 240-GHz heterodyne receiver array in 65-nm CMOS with array-wide phase locking,” IEEE Journal of Solid-State Circuits, vol. 54, no. 5, pp. 1216–1227, May 2019.

[103] I. Gordon, L. Rothman, C. Hill, R. Kochanov, Y. Tan, P. Bernath, M. Birk, V. Boudon, A. Campargue, K. Chance, B. Drouin, J.-M. Flaud, R. Gamache, J. Hodges, D. Jacquemart, V. Perevalov, A. Perrin, K. Shine, M.-A. Smith, and E. Zak, “The hitran2016 molecular spectroscopic database,” Journal of Quantitative Spectroscopy and Radiative Transfer, 07 2017.

[104] P. H. Siegel, “Terahertz technology,” in IEEE Transactions on Microwave Theory and Techniques, vol. 50, no. 3, pp. 910-928, March 2002,

[105] Fitch, Michael J., and Robert Osiander. “Terahertz waves for communications and sensing.” Johns Hopkins APL technical digest 25.4 (2004): 348-355.

[106] K. Takano et al., “A 105Gb/s 300GHz CMOS transmitter,” 2017 IEEE International Solid-State Circuits Conference (ISSCC), 2017, pp. 308-309.

[107] K. Huang and Z. Wang, “Terahertz Terabit Wireless Communication,” in IEEE Microwave Magazine, vol. 12, no. 4, pp. 108-116, June 2011.

[108] Akyildiz, Ian F., Josep Miquel Jornet, and Chong Han. “Terahertz band: Next frontier for wireless communications.” Physical communication 12 (2014): 16-32.

[109] T. S. Rappaport et al., “Wireless Communications and Applications Above 100 GHz: Opportunities and Challenges for 6G and Beyond,” in IEEE Access, vol. 7, pp. 78729-78757, 2019.

[110] H. Saeidi, S. Venkatesh, C. R. Chappidi, T. Sharma, C. Zhu and K. Sengupta, “A 4×4 Distributed Multi-Layer Oscillator Network for Harmonic Injection and THz Beamforming with 14dBm EIRP at 416GHz in a Lensless 65nm CMOS IC,” 2020 IEEE International Solid- State Circuits Conference - (ISSCC), 2020, pp. 256-258.

[111] Ippolito, Louis J. “Attenuation by atmospheric gases,” Radiowave Propagation in Satellite Communications. Springer, Dordrecht, 1986. 25-37.

[112] Kumar, Sushil. “Recent progress in terahertz quantum cascade lasers.” IEEE Journal of Selected Topics in Quantum Electronics 17.1 (2010):38-47.

[113] E. Seok et al., “A 410GHz CMOS Push-Push Oscillator with an On-Chip Patch Antenna,” 2008 IEEE International Solid-State Circuits Conference - Digest of Technical Papers, 2008, pp. 472-629.

[114] S. Razavian and A. Babakhani, “Multi-Spectral THz Micro-Doppler Radar Based on a Silicon-Based Picosecond Pulse Radiator,” 2020 IEEE/MTT-S International Microwave Symposium (IMS), 2020, pp. 787-790.

[115] Joseph S. Melinger, Yihong Yang, Mahboubeh Mandehgar, and D. Grischkowsky, “THz detection of small molecule vapors in the atmospheric transmission windows,” Opt. Express 20, 6788-6807 (2012).

[116] Wang, R., Yao, J.Q., Xu, D.G., Wang, J.L. and Wang, P., 2011, February. “The physical theory and propagation model of THz atmospheric propagation,” In Journal of Physics: Conference Series (Vol. 276, No. 1, p. 012223). IOP Publishing.

[117] Baron, Philippe, Jana Mendrok, Yasuko KASAI, Satoshi OCHIAI, Takamasa SETA, Kazutoshi SAGI, Kodai SUZUKI, Hideo SAGAWA, and Urban Joachim. “AMATERASU: model for atmospheric terahertz radiation analysis and simulation,” Journal

of the National Institute of Information and Communications Technology Vol 55, no. 1 (2008).

[118] Yang, Yihong, Mahboubeh Mandehgar, and Daniel R. Grischkowsky. ”Understanding THz pulse propagation in the atmosphere.” IEEE Transactions on Terahertz Science and Technology 2, no. 4 (2012): 406-415.

[119] Danylov, A., 2006. “THz laboratory measurements of atmospheric absorption between 6% and 52% relative humidity,” Submillimeter-Wave Technology Laboratory University of Massachusetts Lowell, 175.

[120] E. Muehldorf, “The phase center of horn antennas,” in IEEE Transactions on Antennas and Propagation, vol. 18, no. 6, pp. 753-760, November 1970.

[121] Johansson, Joakim F., and Nicholas D. Whyborn. “The diagonal horn as a submillimeter wave antenna.” IEEE Transactions on Microwave Theory and Techniques 40, no. 5 (1992): 795-800.

[122] Y. Yang, M. Mandehgar and D. R. Grischkowsky, “Broadband THz Pulse Transmission Through the Atmosphere,” in IEEE Transactions on Terahertz Science and Technology, vol. 1, no. 1, pp. 264-273, Sept. 2011.

[123] Kim, Gyeong-Ryul, Tae-In Jeon, and D. Grischkowsky. “910-m propagation of THz ps pulses through the atmosphere,” Optics Express 25, no. 21 (2017): 25422-25434.

[124] Ma, Jianjun, Rabi Shrestha, Lothar Moeller, and Daniel M. Mittleman. “Invited article: Channel performance for indoor and outdoor terahertz wireless links,” APL Photonics 3, no. 5 (2018): 051601.

[125] F. Moshirfatemi, “Communicating at terahertz frequencies,” Ph.D. dissertation, 2017.